Expanding the field of view

from classical to extra-classical receptive fields, neurons to populations, and voxels to sensors

Akhil Edadan

`

`

Expanding the field of view

from classical to extra-classical receptive fields, neurons to populations, and voxels to sensors

Het gezichtsveld uitbreiden

van klassieke tot extra-klassieke receptieve velden, neuronen tot populaties en voxels tot sensoren

(met een samenvatting in het Nederlands)

Proefschrift

ter verkrijging van de graad van doctor aan de
Universiteit Utrecht
op gezag van de
rector magnificus, prof.dr. H.R.B.M. Kummeling,
ingevolge het besluit van het college voor promoties
in het openbaar te verdedigen op

vrijdag 18 september 2020 des middags te 12.45 uur

door

Akhil Edadan

geboren op 29 maart 1993
te Payyanur, India

`

Promotor:

Prof. dr. S.O. Dumoulin

Copromotoren:

Dr. W. Zuiderbaan
Dr. M. de Jong

Dit proefschrift werd (mede) mogelijk gemaakt met financiële steun van de European Union's Horizon 2020 research and innovation programme under the Marie Sklodowska-Curie grant agreement No 641805 to S.O. Dumoulin

`

Contents

General Introduction 6

Extending pRF models from fMRI to MEG: A stimulus-referred forward model to predict MEG measurements 18

One in a million: How much do variations in single-neuron receptive fields contribute to population receptive fields? 50

Early extra-striate cortex supports receptive field interactions to process natural images 66

The functional architecture of the visual cortex in psychotic patients with visual hallucinations 84

General Discussion 104

References 110

Nederlandse samenvatting 130

Curriculum Vitae 136

`

`

Chapter 1

General Introduction

`

Vision and receptive fields

Humans are visual beings. Vision is an important sense that is essential for us to interact with and navigate the world around us. Thus, any disorder of the visual system will have a profound impact on our daily life. Importance of vision is also observed in our brain. About 25 % of the human cerebral cortex is devoted to processing visual information (Van Essen, 2003). Consequently, the visual system is one of the most widely studied part of the human brain. A complete understanding of the visual system has numerous advantages such as efficient diagnosis and treatment of various visual disorders, building advanced computer vision and deep learning technologies and creating art that has not been *seen* before (for example, *Movement in squares, 1961* by Bridget Riley, *Room for one color, 1997* by Olafur Eliason).

Visual processing involves a series of steps starting from the photoreceptors in the retina converting the light into electrical signals. These electrical signals are then transferred to the brain. Via lateral geniculate nucleus in the thalamus they reach visual cortex where they are processed by billions of neurons. Any source of visual information has various spatial properties such as position, size, luminance, contrast, color, shape, orientation, and temporal properties such as rate and direction of movement. Understanding visual processing thus requires a knowledge of how these individual features are processed by the neurons in the visual cortex.

Any image is represented by a group of neurons in the visual cortex with every neuron processing the information from a small region within the image, known as the receptive field (RF) of that neuron. The term receptive field was originally used to define an area on the dog's skin from a which a spinal scratch reflex could be elicited (Sherrington, 1906). It was later adapted in vision by Hartline (1940) when he extended the term to the region in the retina from which a response could be elicited in the optic nerve fiber of the frog. He found that the strongest response was observed from the center of the RF which faded with the distance from the center. Kuffler (1953) then determined that the RF of a retinal ganglion cell is a concentric structure with a central excitatory region where a light source produced excitatory response and a large inhibitory region where a light source produced inhibitory response (Kuffler, 1953). However, this notation was found to be confusing. Later it was found that many RF has a center surround organization with a central ON region and an OFF region surrounding it which can act in both excitatory and inhibitory ways depending on the stimulus. For example, An ON region

`

produces a positive response to bright light and negative response to dark light and the OFF region does the opposite. Hubel and Wiesel through a series of works determined RFs for neurons in the visual cortex of cats and monkeys that are selective for shapes, orientation along with the position of the stimuli (Hubel & Wiesel, 1962, 1968, 1974). Neurons whose RFs were closer to each other in the visual field were also found to lie closer in the visual cortex forming visual field maps on the cortex.

However, every neuron is not acting in isolation to process the information in the images, instead they interact with one another through intercellular connections. This was discovered through the findings that sometimes image structures falling outside the RF of these neurons can also influence their responses (for review see (Allman, Miezin, & McGuinness, 1985)). This led to the discovery of region in the visual field where the presence of a stimuli can modulate the responses to the stimuli in the RF but by itself cannot produce a response from the neuron. This region was then called as the **extra-classical RF** for a neuron, since they are activated by stimuli falling outside the **"classical" RF**. The first evidence of such extra-classical interactions was shown by Mcllwain in cats, where a moving stimulus in the far periphery enhanced the response to the stimulus presented inside the RF of the neuron (McIlwain, 1964). Studies have attributed the classical RFs to the feed forward projections from LGN and extra-classical RFs to feedback responses from higher visual areas in visual hierarchy (Angelucci, Levitt, & Lund, 2002; Hupé et al., 1998). Presence of such extra-classical interactions have thus challenged the idea of a hierarchical feedforward way of visual processing and provided evidence for the presence of ascending, descending and lateral flow of information by which neurons modulate the responses of each other.

Initial studies probing the extra-classical RFs used stimuli with simple properties. Later however, researchers started using contextual stimuli that helped to explain the involvement of extra-classical interactions in several steps of visual processing (Allman et al., 1985; Fitzpatrick, 2000; Gilbert & Wiesel, 1990; Knierim & Van Essen, 1992). For example, Field and colleagues in a psychophysical experiment on contour integration found that a set of Gabor patches arranged in a collinear fashion is important to detect the contours and any deviation from collinearity affected the detectability (Field, Hayes, & Hess, 1993). They proposed the idea of long-range interactions between neurons within an association field. Evidence that information from the extra-classical RFs is used by the neurons for figure ground segregation was also shown in a series of experiments by various researchers (Gilbert & Wiesel, 1990; Knierim & Van Essen,

`

1992; Kovacs & Julesz, 1993; V. A. Lamme, 1995). In one such compelling study, Lamme and colleagues found that a neuron whose RF was completely enclosed within a test patch received information about the orientation of the background and used it for identifying the orientation of the test patch (V. A. Lamme, 1995). Various studies have shown that modulation of the response by the extra-classical interactions can either be facilitation, suppression or a combination of the two (Cavanaugh, Bair, & Movshon, 2002; Ichida, Schwabe, Bressloff, & Angelucci, 2007; Kapadia, Ito, Gilbert, & Westheimer, 1995; Levitt & Lund, 1997, 2002) (Figure 1). These extra-classical interactions thus help in the transition from a local processing to a more global representation through figure ground segregation, perception of uniform surfaces and grouping which are the crucial first steps in object recognition and scene segmentation.

`

A

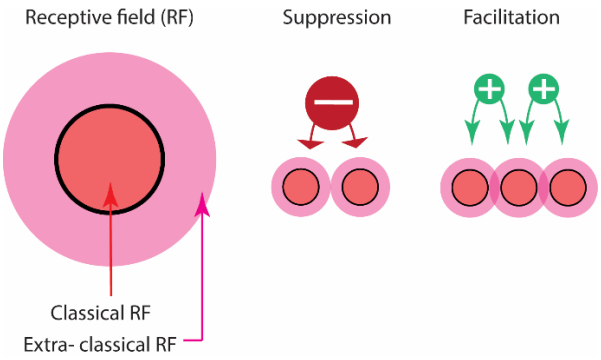

B

Figure 1: Receptive fields (RF) and contextual interactions. (A) An illustration of a typical neuronal RF showing classical RF (bright orange) and extra-classical RF (light orange). Extra-classical interactions can influence the neuronal activity in different ways depending on the nature of contextual interaction. Inhibitory interactions are depicted by the white "-" sign inside red circle and facilitatory interactions are depicted by the white "+" sign inside green circle. RFs from both of the interactions can lead to the activation of extra-classical RF, suggesting input from outside the classical RF (Jones, Wang, & Sillito, 2002). (B) Illustration of how neurons represent an image through their RFs and their interactions. Extra-classical RFs of neurons are not activated in the absence of a contextual interaction (bright orange circles without light orange surrounding it) and neurons process their own preferred image property. For example, a neuron that has a large receptive field size processes the low spatial frequency content in an image and vice versa. However, in the presence of a contextual stimuli, neurons communicate with each other which can activate their extra-classical RFs. Such an interaction can be facilitatory (shown by '+' sign in green circle) for example when RFs are collinear or suppressive (shown by '-' sign in a red circle) when processing iso-oriented lines (Kastner, Nothdurft, & Pigarev, 1999). Also, RFs of the neurons processing the locally oriented lines lying along the contour structure cause the grouping of local features into a more global structure as shown by the dark blue outline on the RFs processing the rails on the bridge.

`

Functional Magnetic Resonance Imaging (fMRI) and population receptive fields (pRFs)

Most of the single neuron RF studies are from non-human primates and cannot be directly translated to humans due to several differences between the species. For example, human visual cortex contains a greater number of neurons compared to other species which are thought to be performing uniquely human skills such as language processing. Since the single neuron activity is measured using invasive electrophysiology techniques which is not feasible to be performed in humans, a non-invasive technique for measuring human brain activity is important for a full understanding of human visual system.

fMRI

fMRI is a technique widely used to measure brain activity to study human visual system. fMRI provides a non-invasive measurement of brain activity at a high spatial resolution. Single recording units in any fMRI measurement are called fMRI voxels with a typical dimension of 2x2x2 mm^3. Given the typical neural densities (50,000 neurons per cubic mm of cortex), every fMRI voxel measures the activity of about 400,000 neurons. (Leuba & Garey, 1989; Rockel, Hiorns, & Powell, 1980). Thus, fMRI measures the activity of a population of neurons and not a single neuron. Briefly, neural activity in the brain needs oxygen which are supplied by the blood. A neural activity thus will cause a local change in the relative amounts of oxygenated and deoxygenated blood in the region of the activity. These have different magnetic properties and can cause inhomogeneities in the magnetic field in the region of activity. fMRI measurements are based on the size of these inhomogeneities. fMRI thus provides an indirect measure of the neural activity through the local changes in the blood flow. The fMRI measurements are hence called Blood Oxygenation Level Dependent (BOLD) signals. fMRI can also be used to study the brain activity in other animals which helps in the comparison of findings between different species.

pRFs

Since fMRI measures the activity of a population of neurons, fMRI measurements can be used to record the brain activity in response to a stimulus presented at the aggregate RF of a population of neurons. RFs estimated from every fMRI voxel are thus called the population

`

receptive fields (pRFs) (Figure 2). PRFs measured from every fMRI voxel reflects the RF properties of individual neurons inside the voxel and also their interactions with each other.

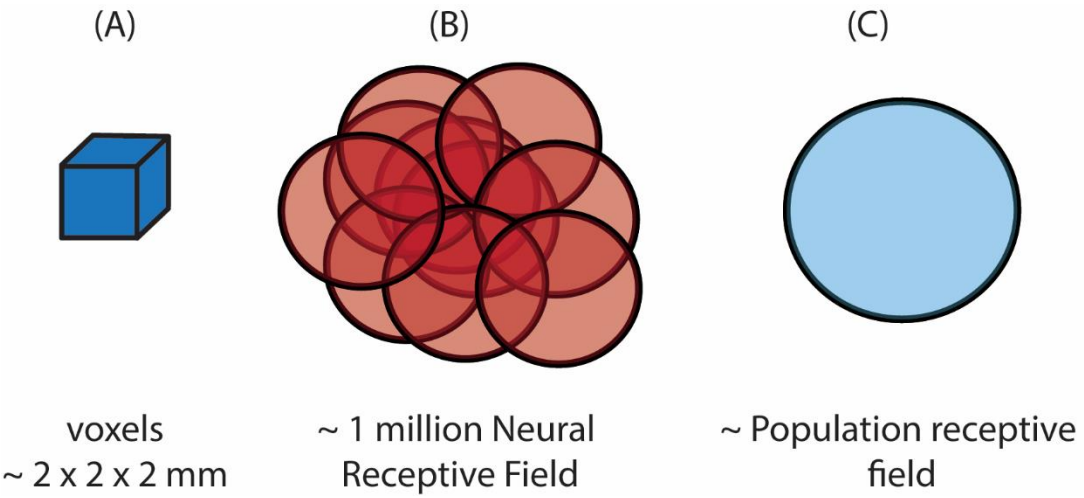

Figure 2. Population receptive fields from a single fMRI voxel (adapted from (Brewer & Barton, 2012))**.** (A) A typical fMRI voxel has a resolution of about 2 cubic mm and can contain about 1 million neurons, and (B) each with an associated RF which are approximately in the same region in the visual field. Classical RFs of the individual neurons are depicted by the bright orange circles. (C) A pRF (blue circle) for the cortical location is estimated as the mean RFs of all the neurons within the fMRI voxel.

Computational neuroimaging and pRF models

PRF properties are estimated using fMRI with help of advanced data analysis approach called computational neuroimaging (Wandell, 1999). In computational neuroimaging approach, predictions are made about the fMRI responses to a range of stimuli and tasks by building models of how the brain performs the computation. Since these models are built referring to the response to a stimulus, these are generally called stimulus referred neural models. One such commonly used model is called the population receptive field (pRF) model (Dumoulin & Wandell, 2008; K. N. Kay, Winawer, Mezer, & Wandell, 2013; Zuiderbaan, Harvey, & Dumoulin, 2012). Using fMRI measurements and pRF models, we can quantify the properties of pRFs. A typical pRF mapping experiment involves a high contrast bar aperture sweeping the visual field in different directions viewed by the participants in the fMRI scanner when the fMRI responses

`

are measured. A pRF model analysis then starts with defining a neural pRF model that summarizes a region in the visual field that the stimulus process. The most basic pRF model is a 2-dimensional circular symmetric gaussian defined by a position (x, y) and size (σ) (Dumoulin & Wandell, 2008). FMRI response is then predicted by multiplying the pRF model with the stimulus sequence that varies over space and time and convolving the resulting time course with the hemodynamic response function. The parameters that define pRF model are varied and optimal pRF parameters are determined by minimizing the residual sum of squares of the difference between the predicted response and measured fMRI response (Figure 3).

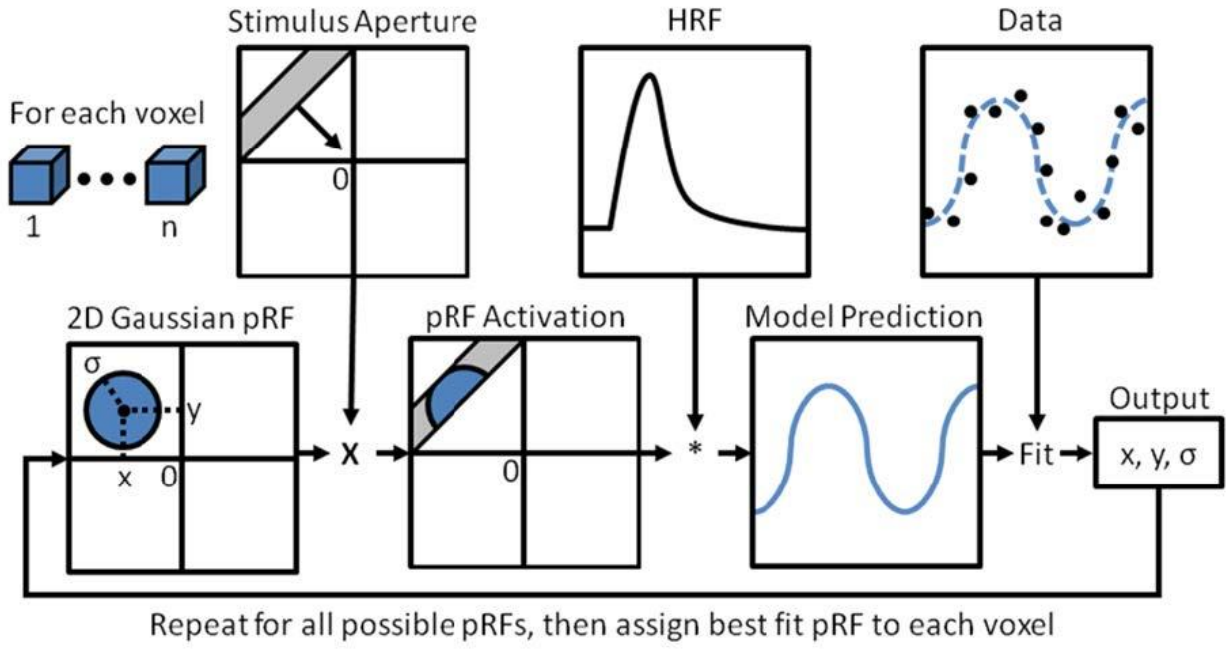

Figure 3. pRF modeling procedure. Flow chart describing the pRF model fitting procedure. For each fMRI voxel, a pRF model is defined as a 2D Gaussian with a position (x, y) and size (σ). PRF model is then multiplied with the stimulus aperture giving the pRF activation. PRF activation is then convolved with the hemodynamic response function (HRF) to estimate the model prediction. Model prediction is compared with the measured fMRI data from the voxel. This procedure is then repeated for pRF models with different position and size parameters. The pRF model which explains the maximum variance in the data is assigned as the pRF for the particular voxel (Figure 4 from Brewer & Barton, 2012; which was adapted from Dumoulin & Wandell, 2008)

`

Are pRF models representative of underlying neural activity?

Since fMRI measures neural activity indirectly as the local changes in the blood oxygenation, the measurement could be reflecting a mix of neural activity and the neurovascular coupling (Heeger & Ress, 2002; Logothetis & Wandell, 2004). However, every fMRI study is based on the implicit assumption of linearity between the measured BOLD responses and underlying neural activity (Boynton, Engel, Glover, & Heeger, 1996). There are other non-invasive techniques also used in neuroscience to measure the human brain activity, such as magnetoencephalography (MEG), electroencephalography (EEG), and electrocorticography (eCOG) which gives a more direct measurement of the underlying neural activity. Each of these have its own advantages and disadvantages like fMRI. Hence, it is important to combine the information from these different modalities to get a complete picture of brain activity. In this effort, recently pRF models have also been extended to another measure of brain activity in humans, namely invasive intracranial electrode recordings (Harvey, Vansteensel, et al., 2013; Winawer et al., 2013). In **Chapter 2** of this thesis we extent pRF models to a non-invasive recording technique. We do this by using the pRF models built from fMRI to predict MEG responses to a similar visual stimulation. Thereby, we aim to validate that the two measurements are recording a common underlying neural activity.

Magneto encephalography

MEG is a common technique used in neuroscience to measure brain activity based on the fundamental principle that electrical activity is associated with magnetic fields. In every neuron, neural activity (for example, resulting from a stimulus activity in the RF of the neuron) causes the movement of ions between intra and extracellular space. Such an ionic movement creates a local field potential (LFP) between the dendrites and soma. This potential difference results in a primary intracellular current along the soma-dendritic axis of the neuron and an extracellular volume current in the opposite direction (da Silva, 2013). When these currents flow across a large number of neurons with a similar dendritic orientation, a magnetic field strong enough to be measured will be created on the scalp surface (Hämäläinen, Hari, Ilmoniemi, Knuutila, & Lounasmaa, 1993). This magnetic field can then be measured on the scalp surface with the help of MEG sensors (~ 200) (Figure 4). MEG signals can be used to study neural activity at high temporal resolution (in milliseconds). Also, compared to fMRI signals, MEG provides direct measurement of the neural activity. Since each MEG sensor measures the activity of neurons

`

over a large area of the cortex (in centimeters), pRF models are not commonly used in MEG studies. In **chapter 2** of this thesis, we present a forward modeling approach that can be used to predict MEG responses using the pRF models built using fMRI, thereby opening new opportunities for exploring changes in pRF properties over time.

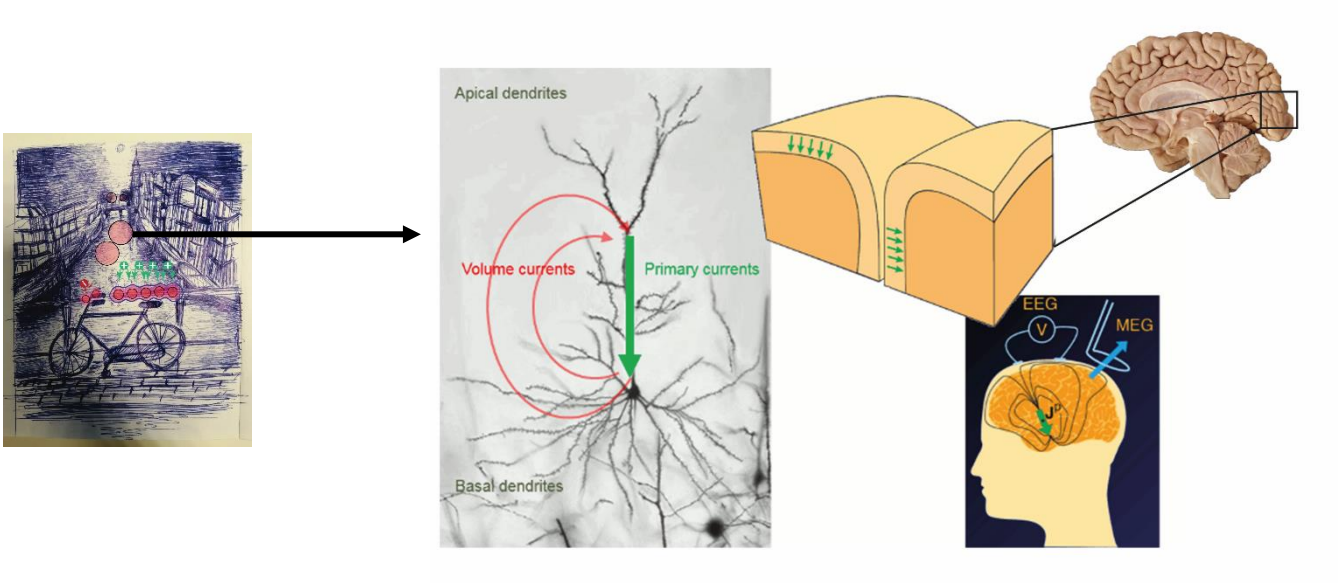

Figure 4. Neural mechanism underlying MEG signals. A schematic representation showing the origin of MEG signals. Similar to fMRI, MEG also measures the neural activity of a population of neurons. Single neurons in the population will process the information from its RF resulting in an electrical activity. Synchronous electrical activity from a large number of such neurons are required to create a magnetic field that are strong enough to be measured by the MEG sensors (figure adapted from https://neuroimage.usc.edu/brainstorm/Tutorials/HeadModel).

Applying pRF models for understanding visual processing

PRF models have been a cornerstone in visual neuroscience for studying spatial properties of visual system in both healthy and diseased population (Dumoulin & Knapen, 2018). PRF models provide detailed information about the pRF properties such as position, RF center size, (Dumoulin & Wandell, 2008), RF suppressive surround size properties (Zuiderbaan et al., 2012), spatial summation (K. N. Kay et al., 2013), connectivity (Haak et al., 2013). PRF sizes estimated from the pRF models can also be compared to the electrophysiology studies (Dumoulin & Wandell, 2008; K. N. Kay, Naselaris, Prenger, & Gallant, 2008). PRF modeling approach can also be used to define the visual field maps with the polar angle and eccentricity maps derived from the pRF position estimates (Figure 5). Visual field maps are used as regions of interest

`

(ROI) in ROI analysis, wherein all the measurements within a ROI are assumed to have homogeneous processing and can be averaged in individual's brain. Finally, pRF models are also used to characterize the changes in the functional architecture in various ophthalmological and neurological disorders (E. J. Anderson et al., 2017; Dumoulin & Knapen, 2018; Hoffmann et al., 2012; Schwarzkopf, Anderson, de Haas, White, & Rees, 2014).

Thus, with the help of carefully designed experimental stimuli and tasks, we can use pRF models to study different properties of visual processing in both healthy and diseased population. In **Chapter 3**, we investigate the extent to which the pRF properties reflect the RFs of the individual neurons using stimuli with different spatial frequencies that can excite sub population of neurons selective to a specific spatial frequency. In **Chapter 4,** we investigate the effect of the extra classical RF interactions on the pRF properties. Finally, in the **chapter 5**, we use pRF models to investigate the abnormal visual processing in patients with schizophrenia that leads to visual hallucinations.

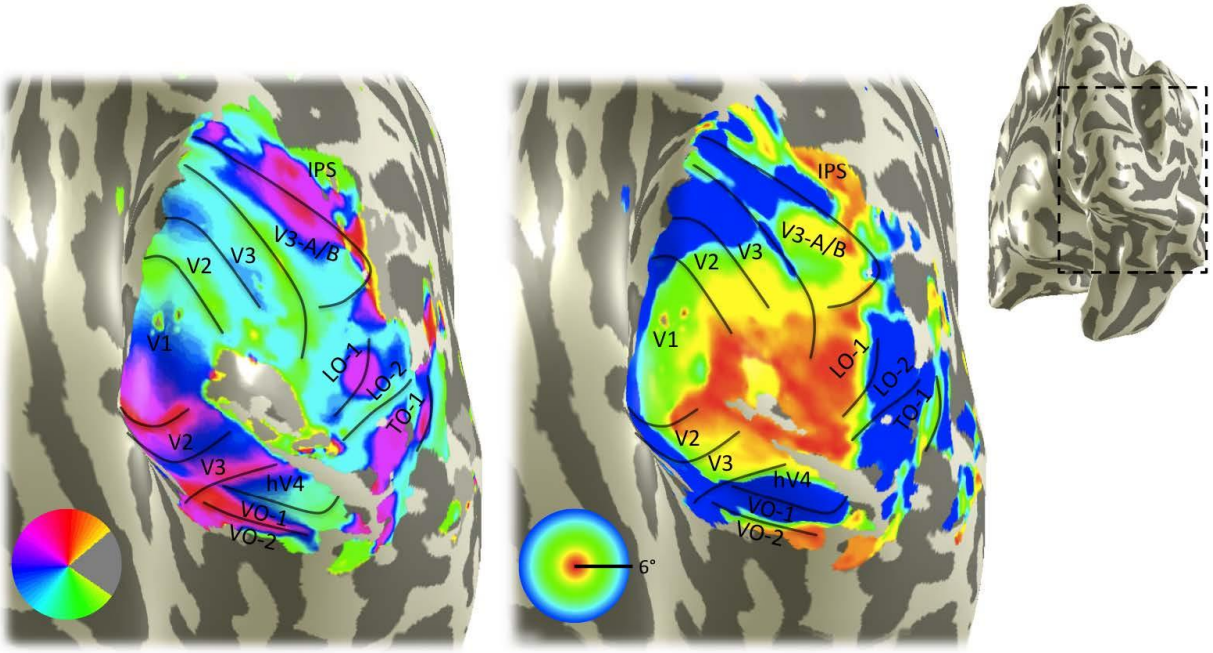

Figure 5. Visual field maps defined using population receptive field mapping technique in humans. Inset shows the smoothed surface rendering of the right hemisphere and the dotted box indicating the region that is magnified. Magnified region of the cortex shows the visual field maps (V1, V2, V3, V3-A/B, IPS, hV4, VO-1, VO-2, LO-1, LO-2, TO-1) delineated using the polar angle (left) and eccentricity (right) maps extracted from the pRF model parameters (Figure 1 from (Wandell, Winawer, & Kay, 2015)).

`

Schizophrenia

Schizophrenia is a severe neuropsychiatric disorder which affects the way in which the patient thinks, feels and behaves. Symptoms of schizophrenia are often classified into positive, negative and cognitive. Positive symptoms include psychotic behaviors such as hallucinations and delusions. Negative symptoms are those which are associated with a disturbance in the normal emotions and behaviors and can include reduced ability to perform facial expression and reduced feelings of pleasure in everyday life. Cognitive symptoms are generally negative such as poor information processing, decision making, and attention.

Hallucinations in the patients with schizophrenia can seriously affect their quality of life. Visual hallucinations in patients with schizophrenia is often linked with an impaired visual processing they exhibit. There are some theories that specifically link the disturbed contextual interactions and gain control mechanisms which are resulting from the properties of underlying extra-classical interactions (Dakin, Carlin, & Hemsley, 2005; Silverstein & Keane, 2011). In the **chapter 5**, we investigate the neural mechanism underlying the visual hallucinations in patients with schizophrenia using pRF models.

Summary and thesis outline

Receptive fields (RF) are thus a fundamental organizational principle of the visual cortex and an important aspect of visual processing. Thus, studying the RF properties are important for understanding visual processing. In humans, pRF models are being used to study the spatial properties of the RFs of a population of neurons. In this thesis, we investigate the properties of extra-classical RFs in both healthy individuals and a patient population using pRF models. In **chapter 2**, we examine the relationship between the fMRI BOLD response and MEG magnetic field measurement to validate that pRF models reflect the underlying neural computations. We then proceed to investigate the extent to which the properties of single neurons are maintained at the population level in **chapter 3**. We dive deeper into the interactions between the neurons in **chapter 4** by studying the extra-classical RFs of neurons in healthy subjects. Finally, we apply the pRF model analysis in a patient population known to shown abnormal visual perception due to an inability to use context in a stimulus in **chapter 5**.

`

Chapter 2

Extending pRF models from fMRI to MEG: A stimulus-referred forward model to predict MEG measurements

Akhil Edadan, Eline R Kupers, Noah C Benson, Wietske Zuiderbaan, Maartje C. de Jong, Serge O Dumoulin, and Jonathan Winawer (under review)

Author contributions

SOD and JW designed the study. ERK created the stimuli and collected data. ERK and AE analyzed data. ERK and AE drafted the manuscript. NCB, WZ, MCDJ, SOD, and JW provided general supervision and guidance throughout

`

Abstract

Population receptive field (pRF) models predict neurophysiological responses at high spatial resolution (millimeters) on visual cortex to visual stimuli varying in spatial position using functional MRI (fMRI), in both healthy and clinical human populations. Due to lower spatial resolution, pRF models are not widely used in magnetoencephalography (MEG). Here, we introduce a forward-modeling approach to extend pRF models determined from fMRI to predict MEG sensor responses. Subjects viewed contrast-reversing bar stimuli sweeping across the visual field in separate fMRI and MEG sessions. We used the pRF model to first make the prediction on the cortex, before predicting MEG time series for every sensor using the MEG forward model. We compared the predicted MEG responses to the observed MEG data (visually evoked steady-state responses at the contrast-reversal rate of the stimulus) and found that using the original pRF parameters estimated by fMRI could explain up to 60 percent of the variance in steady-state MEG sensor responses. When perturbing the pRF parameters by either scaling pRF sizes or rotating the pRF centers around the fovea, the ability of our model to explain variance in the MEG responses decreases by ~15%. This suggests that the MEG is sensitive to pRF properties derived at the fMRI spatial scale. We conclude that our method provides a quantitative approach to link fMRI and MEG measurements to study the spatiotemporal dynamics of human visual field maps.

`

Introduction

A fundamental goal in human neuroscience is to link cognition to brain function. One approach to reach this goal is to build encoding models. By defining the operations that relate an input to its output (e.g. a visual stimulus to the BOLD response of a particular cortical location), one can study the mechanisms underlying the measured neural responses. Starting from the visual stimulus as input, these stimulus-referred encoding models have been successful in predicting neural responses in visual cortex, for example fMRI responses (e.g. pRF model by (Dumoulin & Wandell, 2008); CSS model by (K. N. Kay et al., 2013)), single unit responses (Mante, Bonin, & Carandini, 2008), and LFP responses from EcoG (Electrocorticography) electrodes (Harvey, Vansteensel, et al., 2013; Hermes, Petridou, Kay, & Winawer, 2019). Such encoding models can help to clarify the relation between different measurements of brain activity along with providing an ability to study the visual system at a high spatiotemporal resolution.

However, these encoding models are relatively uncommon in predicting non-invasive electromagnetic field measurements like magnetoencephalography (MEG) or electroencephalography (EEG). Both MEG and EEG imaging techniques are widely-used and provide excellent time-resolved measurements of brain activity across the whole brain. Nevertheless, these techniques lack encoding models because the pooling area of a single sensor covers large parts of the cortex (in the order of several centimeters); the covered area is much larger than the scale at which fMRI can measure stimulus-selectivity in visual cortex. At the spatial resolution of fMRI, the visual field preference of a given neural population in visual cortex, i.e. its population receptive field (pRF), can be estimated on the cortex at a millimeter scale. To estimate pRFs at the same spatial resolution as fMRI for every MEG sensor, one would require a computational model that transforms the signal from a few hundred sensors to thousands of sources on the cortex. Solving such an inverse problem is ill-defined and can have infinite number of solutions.

Here, we propose a novel stimulus-referred forward modeling approach predicting MEG sensors responses from stimulus to cortex and from cortex to sensors. We use the pRF model developed by Dumoulin and Wandell (2008), which has been a well-established approach to study the spatial properties of the human visual system in both healthy and diseased (Dumoulin & Knapen, 2018; Wandell & Winawer, 2015). By first estimating the pRFs using fMRI, the model predicts how the neural response of a particular visual stimulus is represented on the cortical surface. We then use the MEG forward model to project these predicted responses to MEG sensors, instead of creating an inverse solution. These predicted MEG sensor responses can

`

then be compared to observed MEG responses from subjects viewing the same visual stimulus. Our results show that we can predict the MEG responses to a visual stimulus using the pRF models estimated from fMRI.

Methods

Subjects

Ten subjects (5 female), ages 20-45 years (M = 29.7 years, SD = 7.3 years) participated in the study with normal or correct-to-normal vision. All scanning sessions were acquired at New York University. Subjects provided written informed consent. The experimental protocol was in compliance with the safety guidelines for MRI and MEG research and was approved by the University Committee on Activities involving Human Subjects at New York University, USA.

Stimuli

Stimuli were generated using MATLAB (MathWorks, MA, USA) and PsychToolbox (Brainard, 1997; Pelli, 1997) on a Macintosh computer. In both MRI and MEG sessions, subjects were presented with contrast-reversing checkerboard stimuli (10 Hz), windowed within a bar aperture that swept across the visual field in discrete steps. The area outside the stimulus was set to a constant mean luminance. Both MRI and MEG stimuli matched in size (field of view (h x w): 20°x 20°), contrast-reversal rate (10 Hz), bar width (2.5°, i.e. $1/4^{th}$ of the full-field stimulus radius, 10°), but differed in presentation length and sequence (see Experimental design).

Stimulus display

MRI

MRI data for subjects S1 and S2 were acquired with a different scanner (Allegra versus Prisma) and visual display compared to subjects S3-S10.

Allegra: For subjects S1 and S2, stimuli were presented with an LCD projector (Eiki LC_XG250, CA, US) with a screen resolution of 1024 x 768 pixels and refresh rate of 60 Hz. Stimuli were displayed onto a translucent back-projection screen in the bore of the magnet. Subjects viewed the screen through an angled mirror mounted onto the coil of the scanner at a distance of ~58 cm and a field of view of ~32° x ~24° (w x h). To prevent stimuli to be obscured by the MRI compatible eye tracker mounted on a rig inside the bore (~1° of the lower visual field), we

`

decided to confine the stimulus diameter to a circular aperture with a field-of-view of 20°x20° (w x h). The display was calibrated and gamma-corrected using a linearized lookup table.

Prisma: For subjects S3-S10, stimuli were presented with a DPL LED PROPixx projector (VPixx, QC, Canada) with a screen resolution of 1920 x 1080 pixels and refresh rate of 60 Hz. Images were displayed onto a translucent back-projection screen in the bore of the magnet. Subjects viewed the screen through an angled mirror mounted onto the coil of the scanner at a distance of ~83.5 cm and a field of view of ~35° x ~24.4° (w x h). The visible part of the display extends to a circular aperture radius of 12.2° of eccentricity. However, to match our stimuli with previous subjects' scan sessions, we confined the stimuli to a diameter of 20°. The display was calibrated and gamma-corrected using a linearized lookup table.

MEG

Images were presented using an InFocus LP850 projector (Texas Instruments, Warren, NJ) with a resolution of 1024 x 768 pixels and refresh rate of 60 Hz. Images were projected via a mirror onto a front-projection translucent screen at a distance of approximately 42 cm from the subject's eyes (field of view: 22° × 22°). The display was calibrated with the use of a LS-100 luminance meter (Konica Minolta, Singapore) and gamma-corrected using a linearized lookup table.

Experimental design

Subjects participated in one 1.5-hr MRI and one 2-hr MEG session. Sessions were scheduled on different days.

MRI

An MRI session contained 6 runs, where each run was 6.1 minutes. For a given run, the bar apertures swept across the visual field in discrete steps (1.5s per bar position, 31.5s per bar sweep, see Figure 1A) in 8 different bar configurations (4 different orientations: 0°, 45°, 90°, 135°, with two step directions for each orientation). Two step directions are required for fMRI to avoid biased pRF parameter estimates due to the lag of hemodynamic response function. After the first, third, fifth and seventh bar sweep, there was a 22.5s mean luminance or 'blank' period. In addition, each run started and ended with a 12s blank period. A fixation dot was presented in the center of the screen throughout the run, switching between red and green colors (32

`

switches per run, average of 7.2s). Subjects were instructed to fixate on the dot throughout the run and report a switch in color with a button press.

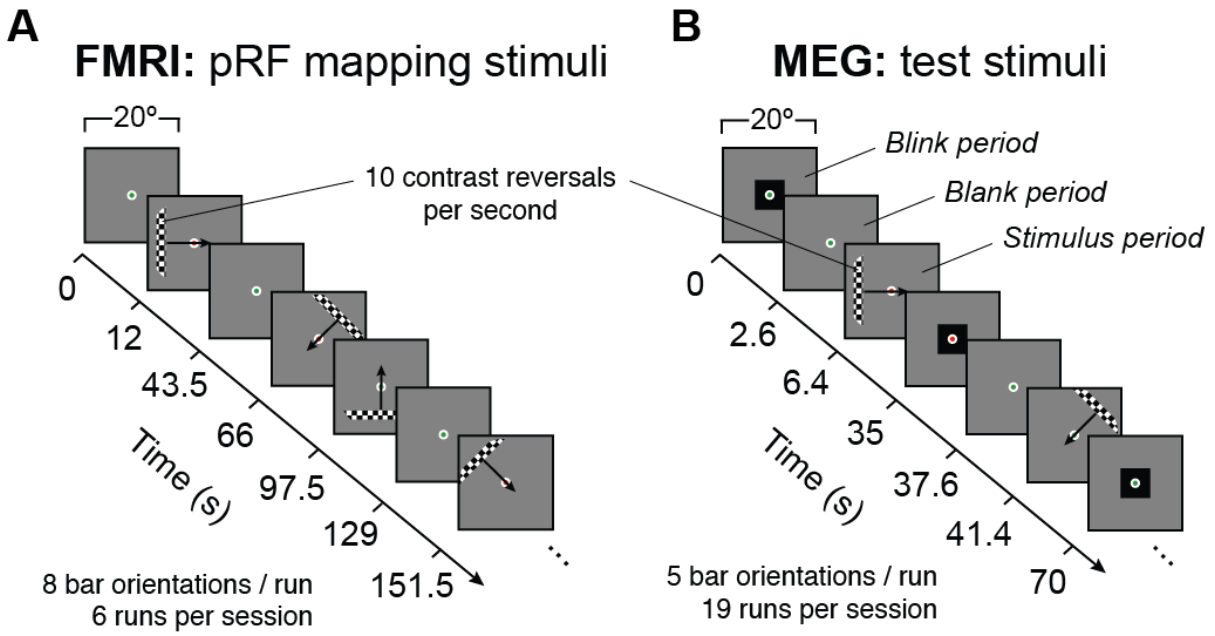

Figure 1. Retinotopic mapping stimuli for fMRI and MEG experiments. (A) FMRI stimuli were used to map pRFs on the cortical surface. Contrast-reversing (100 % contrast) checkerboard bars swept in non-overlapping discrete steps across the visual field (diameter = 20 deg, 1 step per TR, TR=1.5 s), interleaved with blank periods (mean luminance). One run consisted of 8 bar sweeps along cardinal and off-cardinal axes in both directions. Subjects were instructed to fixate in the center of the screen and press a button every time the fixation dot changed color. Fixation dot is enlarged for visibility purposes. (B) MEG stimuli were used in MEG experiment and in stimulus-referred forward model to create predictions. Stimuli were very similar to fMRI (identical contrast, size, and contrast-reversal rate), except for its sequence and duration. One run contained 5 bar sweeps (3 cardinal, 2 off-cardinal) with shorter step durations (TR=1.3 s). Stimulus periods were interleaved with blank and blink periods. During blink periods, subjects were encouraged to make eye blinks to limit blinks during blank and stimulus periods. Blink periods were excluded in both data analysis and model predictions.

MEG

All subjects participated in MEG sessions containing 19 runs, where each run was 3 minutes with short breaks between runs. For a given run, the bar apertures swept across the visual field in discrete steps (1.3s per bar position, 28.6 s per bar sweep) in 5 different bar configurations for a given run (4 different orientations: 0°, 45°, 90°, 135° with two step directions for 0° and one

`

step direction for 45°, 90° and 135°) (see Figure 1B). MEG runs contained mostly a single step direction, because the measured magnetic flux does not contain a time-lag compared to the hemodynamic response function measured with fMRI. This means that we do not need two step directions of the bar to balance out the bias in a particular direction when estimating the pRF parameters.

Before every bar sweep and after the last bar sweep, there was a 2.6s mean luminance or 'blank' period followed by a 3.8s 'blink' period indicated by a mean luminance display with a small black square in the center of screen. A fixation dot was presented in the center of the screen throughout the run, switching between red and green colors (32 switches per run, average of 5.6s).

All subjects were instructed to fixate on the dot throughout the run and report a switch in color with a button press. In addition, subjects were encouraged to blink during the blink period and minimize their blinking during the rest of the run.

Data acquisition

MRI

All subjects' structural and functional data were acquired at the Center for Brain Imaging at New York University. We used a Siemens Allegra 3T head-only scanner for subjects S1 and S2, and a Siemens Prisma 3T full-body scanner for subjects S3-S10 after the irreparable self-quench episode of the Allegra scanner.

Siemens Allegra 3T

Functional data were collected with a Nova Medical phased array, 8-channel receive surface coil (NMSC072). BOLD fMRI data were acquired using a T2*-sensitive echo planar imaging (EPI) pulse sequence (1500 ms TR, 30 ms TE, and 72° flip angle; 2.5 mm^3 isotropic voxels, with 24 slices). The slice prescription was placed approximately perpendicular to the calcarine sulcus and covered most of the occipital lobe, and the posterior part of both the temporal and parietal lobes. An additional field map was collected in the middle of the MRI session to correct functional data for B0 field inhomogeneity during offline image reconstruction using the in-house Center for Brain Imaging algorithm.

Structural data were collected in the same (S2) or separate MRI session (S1) with a Nova Medical head transmit/receive coil (NM011). Data consisted of T1 weighted whole brain anatomical images using a 3D rapid gradient echo sequence (MPRAGE, 1 mm^3 isotropic voxels). Additionally, a T1 weighted "inplane" image was collected with the same coil and slice prescription as the functional scans to aid alignment of the functional images to the high-

`

resolution T1 weighted anatomical images. This scan had a resolution of 1.25 × 1.25 mm and a slice thickness of 2.5 mm.

Siemens Prisma 3T

Both structural and functional data were collected with a 64-channel phased array receive coil. BOLD fMRI data were acquired using a T2*-sensitive echo planar imaging pulse sequence (1-s TR; 30 ms echo time; 75° flip angle; 2 mm^3 isotropic voxels, multiband acceleration 6). Two additional scans were collected with reversed phase-encoded blips, resulting in spatial distortions in opposite directions. These scans were used to estimate the spatial distortions in the EPI runs and used to correct the EPI runs during preprocessing.

Structural data were collected in the same session consisting of T1-weighted whole brain anatomical images (1 mm^3 isotropic voxels) using a 3D rapid gradient echo sequence (MPRAGE). No additional inplane image was needed for alignment for session with the Prisma scanner, because the spatial resolution of the EPIs was higher and whole-brain compared to the Allegra scanner.

MEG

MEG data were acquired continuously with a whole head Yokogawa MEG system (Kanazawa Institute of Technology, Japan) containing 157 axial gradiometer sensors to measure brain activity and 3 orthogonally-oriented reference magnetometers located in the dewar but away from the brain area, used to measure environmental noise. The magnetic fields were sampled at 1000 Hz and were actively filtered during acquisition between 1 Hz (high pass) and 500 Hz (low pass).

Before recording, each subject's head shape was digitized with a handheld FastSCAN laser scanner (Polhemus, VT, USA). Digital markers were placed on the forehead, nasion, left and right tragus and peri-auricular points. To calibrate the digital head shape with the MEG sensors space, five electrodes were placed on the identical location of five digital markers (3 forehead and left/right peri-auricular points). Before and after the main MEG experiment, separate recordings were made of the marker locations within the MEG dewar.

Data Analysis

MRI Preprocessing

Allegra & Prisma structural data: Structural T1-weighted scans were auto-segmented with FreeSurfer's recon-all algorithm ((Dale, Fischl, & Sereno, 1999; Fischl & Dale, 2000; Fischl, Liu, & Dale, 2001; Fischl, Sereno, & Dale, 1999); available at http://surfer.nmr.mgh.harvard.edu/). If needed, errors in white/gray matter voxel segmentation were manually corrected. Visually

`

responsive regions of interest (ROIs) were defined on the inflated cortical surface of individual subjects using the probabilistic atlas of visual areas by (Wang, Mruczek, Arcaro, & Kastner, 2014) resulting in boundaries for areas V1-V4, V3A/B, VO1/2, LO1/2, TO1/2, PHC1/2, IPS0-5, SPL1, and FEF.

Allegra functional data: Using the VistaSoft toolbox (https://github.com/vistalab/vistasoft), functional scans were re-oriented to a standardized NifTi orientation (RIA to LAS), slice-time corrected by resampling the time series in each slice within the 1.5s-volume to the center slice, and motion corrected by aligning all volumes of all scans to the first volume of the first scan. The first 8 volumes of each functional scan were removed to avoid unstable magnetization of the scanner. Functional scans were aligned to the T1-weighted anatomical scan using the additional "inplane" scan.

Prisma functional data: Functional scans were converted from dicom into BIDS format (Gorgolewski et al., 2016) using NYU Center for Brain Imaging in-house version of NIPY's heudiconv (http://as.nyu.edu/cbi/resources/Software.html). The following preprocessing workflow was implemented with the nipype toolbox (Gorgolewski et al., 2016). Using the FSL toolbox (S. M. Smith et al., 2004), all volumes from all EPIs were then realigned to the single-band reference image of the first EPI scan. This single band reference image was then registered to the additional spatial distortion scan with the same phase encoding direction. The two additional spatial distortion scans with opposite phase-encoding direction were then used to estimate the susceptibility-induced warp field using a method similar to (Andersson, Skare, & Ashburner, 2003). Motion correction, registration to the spatial distortion scan and unwarping were then applied in a single step to each volume of each EPI. The unwarped EPIs were aligned to the high-resolution whole-brain T1 using FreeSurfer.

Allegra & Prisma functional data: Time series from EPIs were resampled to 1 mm^3 isotropic voxels within the gray matter voxels using trilinear interpolation. Time series within the gray matter voxels were converted into percent signal change by dividing the signal by its mean. Baseline drifts were removed from each run with high-pass temporal filtering using 3 discrete cosine terms (0 cycles or "DC"; 0.5 cycle and 1 cycle). At last, all 6 runs were averaged given that subjects saw the same stimuli within a dataset.

MEG Preprocessing

The FieldTrip toolbox (Oostenveld, Fries, Maris, & Schoffelen, 2011) was used to read the raw data files. For all subsequent MEG analyses, custom code was written in MATLAB. With use of the triggers from the stimulus presentation computer, MEG data were first divided into 1300 ms

`

epochs (i.e. one MEG TR) for every MEG sensor. For all subjects, epoching resulted in an initial 2660 epochs per sensor: 22 TRs per bar sweep, with 2 TRs for blank and 3 TRs for blink periods before each sweep, and after the last bar sweep of every run, 5 bar sweep directions, for 19 runs. To avoid the transient response associated with a change in the stimulus (either a change in bar position or from a blank period to a stimulus period), we then shortened each epoch to 1100 ms, skipping the first 150 ms and last 50 ms of each 1300-ms epoch. Epoched data were high-pass filtered with a 1 Hz Butterworth filter (with a high-pass amplitude of 3 dB and a passband frequency of 0.1 Hz and amplitude of 60 dB). We used a simple algorithm to detect outliers. First, we computed the variance for every 1100-ms epochs, for each MEG sensor. We labeled an epoch as 'bad' if its variance was 20 times smaller or 20 times larger than the median variance across all epochs and sensors. If more than 20% of the epochs were labeled bad for a given sensor, then we removed the entire sensor from analysis. If more than 20% of sensors contained the same 'bad' epoch, we removed the entire epoch from analysis. Time series within 'bad' epochs that were not removed yet, were replaced by the time series spatially interpolated across nearby sensor (weighting sensors inversely with the distance). We removed on average ~ 21% of dataset, including all epochs of the 5 long-term broken sensors in our MEG system.

We used the Noisepool-PCA algorithm to increase the signal-to-noise ratio (SNR) of our MEG time-series (Kupers et al., 2018). In short, for each subject the algorithm defines a noise pool: a subset of sensors that contained little to no 10 Hz (or stimulus-locked) response. Time series within each epoch and sensor of the noisepool were then filtered to remove all 10 Hz (and harmonics) components. Using principal components analysis (PCA), we defined global noise regressors from the filtered noise pool time series. For each subject, the first 10 PCs were used to create 10 new denoised datasets: the first denoised dataset had the PC 1 projected out of the data in each sensor, epoch by epoch. The second denoised dataset had PC1 and PC2 projected out, etc. For each denoised dataset, we calculated the median R^2 across bootstrapped epochs. The optimal number of PCs to project out was the smallest number of PCs that resulted in a denoised data with a median R^2 within 5% of the maximum possible median R^2 of 10 datasets. This resulted in removing 6 PCs on average across subjects, ranging between 2-8 PCs. At last, we reshaped the denoised MEG Data into a 4D array: *t* time points x *k* epochs x *n* sensors x *m* runs.

`

MEG data quality check

We calculated two parameters to check the quality of the measured MEG data, coherence and split half reliability. First, we computed the coherence for every MEG sensor. This metric provided a signal-to-noise ratio of the steady-state response within stimulus periods and was defined by dividing the average 10 Hz amplitude by the average amplitudes of 10 Hz and neighboring frequencies (i.e. 9 to 11 Hz). The second metric is the split half reliability of the 10 Hz steady state amplitudes. In this case, we split the 19 repeated runs into halves and average across runs within both halves. We then calculate how much variance the average run of the first half can explain the second half, and vice versa. We then average the two variance explained values per MEG sensor, resulting in a split half reliability sensor map.

MRI-MEG head model and alignment

The head model, also referred to as the 'lead field' or 'gain matrix', describes the contribution of cortical locations (or 'sources') to the activity at each individual MEG sensor. To generate this head model, we align the individual's anatomy and the MEG helmet in a common coordinate space using the Brainstorm toolbox (Tadel, Baillet, Mosher, Pantazis, & Leahy, 2011).

Specifically, we defined the nasion and left/right peri-auricular points in the T1-weighted image of each individual subject. We used Brainstorm's automated alignment algorithm to align the fiducials marked in the T1-weighted image, the recorded locations of electrodes attached to the subject's face while lying in the MEG scanner, and points in the 3D head shape. Small manual translational adjustments were applied to the rotation matrix if necessary. After alignment, we computed the individual subject's head model using Brainstorm's implementation of the overlapping spheres algorithm (Huang, Mosher, & Leahy, 1999) using an individual subject's FreeSurfer's pial surface (~290,000 vertices per hemisphere). The initial head model is unconstrained, using 3 vectors to define the dipole orientation of a single vertex, allowing its local current density in any arbitrary direction. We constrained our head model to one perpendicular dipole per vertex, resulting in a final matrix of all Freesurfer vertices by 157 sensors.

A stimulus referred forward model for MEG responses

We build our stimulus referred forward model using the preprocessed fMRI data and MEG data and their corresponding stimuli. First, we estimate the pRF model parameters for every fMRI voxel. We then use these pRF models to make predictions to the MEG stimuli. These predictions are then translated into the MEG sensor space using the head model. Predicted

`

MEG data is compared with the measured stimulus-locked steady state MEG response to estimate the variance explained (Figure 2). We explain each of these steps in detail below.

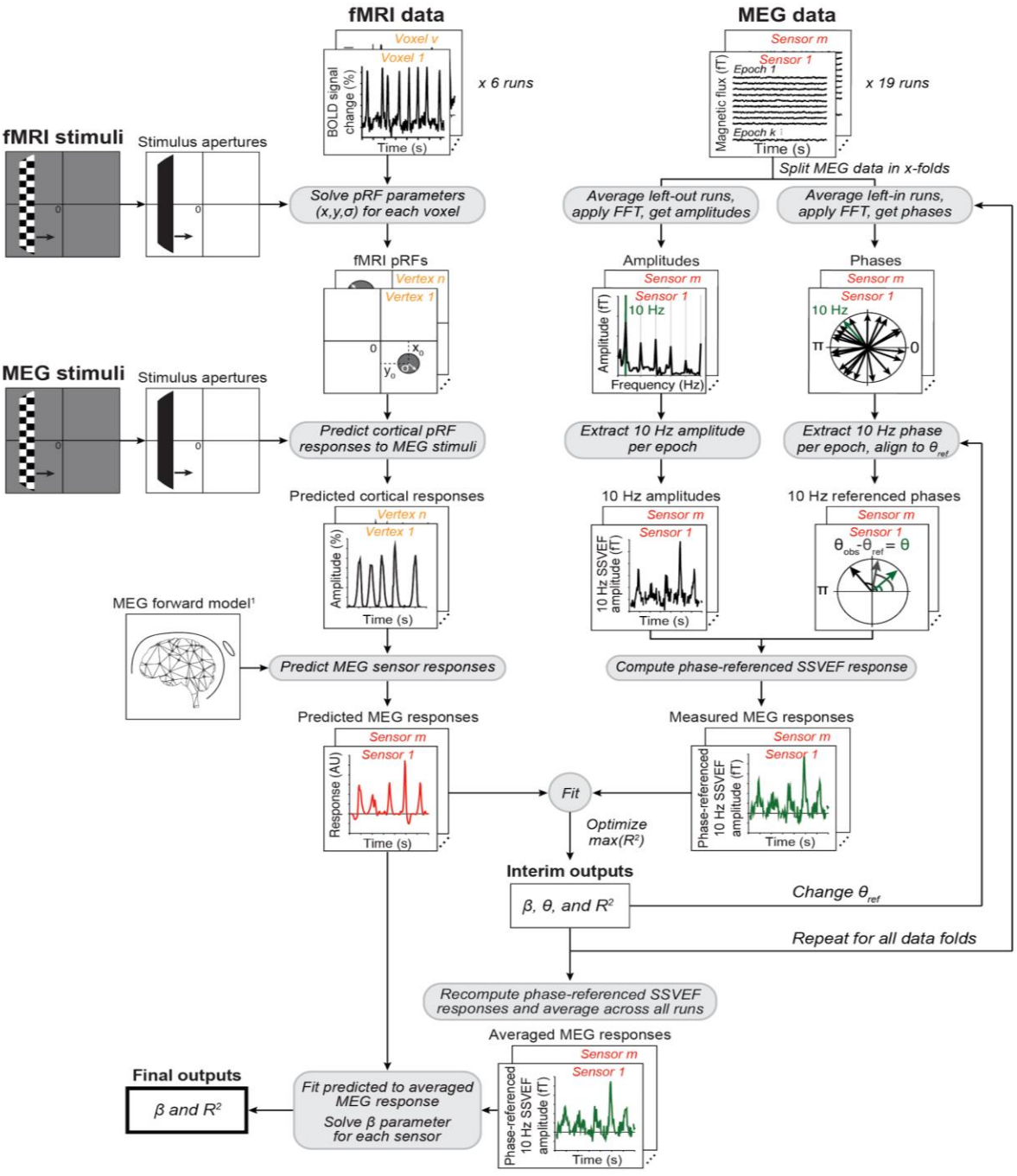

Figure 2. Overview of stimulus-referred forward model. The model takes as inputs both preprocessed fMRI and MEG data and their corresponding stimuli. The fMRI stimuli are binarized into apertures and used to solve pRFs within each cortical location and projected to the cortical surface. These pRFs estimated by fMRI are then multiplied

`

with MEG stimulus apertures to predict time series on the cortical surface. The predicted cortical responses are then multiplied with the gain matrix from the MEG forward model. This forward model is computed by the overlapping spheres algorithm (Huang et al., 1999) and describes the contribution of individual MEG sources to the magnetic fields measured at the MEG sensors. Multiplying both matrices results in predicted MEG responses and are compared against measured MEG responses. The measured MEG responses are computed with leave one out cross-validation. Both left-in and left-out data are averaged across runs and transformed to the Fourier domain. Left-out runs are phase referenced with the reference phase estimated from the left-in runs. For the left-in runs, per MEG sensor, 10 Hz phases will be aligned to one of the possible reference phases, before computing the 10 Hz phase-referenced SSVEF response. To pick the optimal reference phase, we fit the predicted MEG response to the measured MEG response for every possible reference phase and choose the reference phase that results in the largest model fit R^2. This phase-referencing procedure is repeated for the left-out data. At last, phase-referenced MEG responses from all data folds are averaged and fit again by the predicted MEG response, resulting in a final set of betas and R^2 for every sensor.

Solve pRFs with fMRI

Using the Vistasoft toolbox (https://github.com/vistalab/vistasoft), we solved linear circular symmetric 2D Gaussian pRF models on the functional MRI data, as previously described in Dumoulin and Wandell (2008). PRF models were solved by a two-stage coarse-to-fine optimization procedure on the gray matter voxels, using the binarized MRI stimulus apertures and Vistasoft built-in 'difference between two gammas' hemodynamic response function. The first stage of the optimization procedure started with a coarse grid-fit. Parameters from the coarse grid-fit were used as the seed for the fine grid-fit. This fitting procedure resulted in an estimated preferred size (σ, 1 SD of 2D Gaussian), center location (x, y), scaling factor (beta) and variance explained for every voxel. The pRF parameters computed at gray matter voxels are interpolated to surface vertices and a MEG response time series is predicted for every surface vertex.

Smooth pRF parameters across gray matter voxels

Since the pRF parameters are interpolated from the gray matter voxels to the surface vertices using a nearest neighbor interpolation algorithm, there is a chance that a voxel with an unrealistic parameter value could be chosen. To avoid this, we smooth pRF parameters across the cortical surface by calculating a weighted average over a normalized truncated gaussian kernel (Andrade et al., 2001). The gaussian kernel (approximately, a FWHM of 3 mm at 1 cubic mm of voxel resolution) is created at every gray matter voxel, only covering the neighboring

`

voxels. However, neighboring voxels in which estimated pRF model fit did not explain any variance of the data (i.e. a variance explained of 0%) were excluded. We smoothed the position (x, y) and size (sigma) parameters except for beta which we recompute on the cortical surface. Rationale for this as follows.

Beta values estimated using our pRF model implementation covaries inversely with pRF size. A pRF model with a small size will have unrealistically large value. This is because the integral of a pRF kernel is not normalized to be 1, rather depends on the size of the pRF. So, a small pRF will have a small integral, and hence small value during the multiplication of pRFs with the stimulus. When fitting the model to the BOLD signal, some of these small pRFs will have large beta values to accommodate the difference between the predicted and measured BOLD responses. To avoid the large beta values from influencing the smoothing procedure we recompute the beta values on the cortical surface using the following steps. First, we reconstruct the predicted fMRI response for every voxel by multiplying stimulus with the pRF and scaling with the corresponding beta. We then smooth the maximum of predicted response on the cortical surface by multiplying it with a normalized truncated gaussian kernel. Last, we recompute betas by dividing this smoothed maximum response by the maximum of predicted response from smoothed pRF parameters.

Predict MEG responses from pRF parameters estimated with fMRI

To predict the steady-state responses in MEG sensors, we first created a predicted response from estimated pRF parameters on the cortical vertices. Vertices were constrained by those whose pRF parameters explained more than 10% of the variance in the MRI data, and fell within visual ROIs from Wang et al.'s probabilistic atlas (2015). For each vertex, a 2D Gaussian receptive field was constructed using its preferred center and size. The height of this receptive field was scaled by the vertex' beta value. A dot product of these receptive fields and the binarized MEG stimulus resulted in the predicted surface response.

The matrix containing the predicted pRF responses on the cortical surface *S,* were then multiplied with the MEG head model *G*, resulting in predicted MEG sensor responses $\hat{Y}$ (**Equation 1**).

Equation 1: $\hat{\mathrm{Y}} = G \cdot S$

`

Where $\hat{Y}$ *(k* epochs x *m* sensors) are the predicted pRF responses for MEG sensors, *G* (*n* vertices x *m* sensors) is the head model, and *S* (*k* epochs x *n* vertices) stands for the predicted pRF response on the cortical surface.

We compared this predicted MEG sensor responses to the measured MEG responses. Measured MEG response was extracted as phase-referenced steady-state response in steps described below.

Compute phase-referenced steady-state MEG response

Epoched MEG data were transformed into the Fourier domain by applying the FFT to the time series data. We extracted both amplitude and phase information from the spectral MEG data at 10 Hz (i.e. the contrast-reversal rate of the stimulus) to compute a *phase-referenced steady-state response*. This response was calculated as the amplitude at 10 Hz scaled by the difference in angle between the measured phase and a reference phase. This calculation is described in more detail below.

Why compute a phase-referenced steady-state response? Oftentimes, steady-state visually evoked fields are computed by taking the absolute amplitude or power at the contrast-reversal rate of the stimulus while ignoring the phase information. However, this phase information can differ across sensors. For example, because the time for visual information to reach a particular cortical location is different, or because MEG sensors sum over cortical locations that vary in dipole orientations. Taking this phase information into account allows for a richer representation of the measured steady-state response.

To compare differences in phase information, one needs a reference phase. For every run and sensor, we choose a reference phase from 100 potential phases (ranging from 0-2π with equal intervals of π/50) using the following leave-one-run-out approach:

First, we separated MEG data into 2 run groups. We computed the average phase at 10 Hz per epoch across the first split half, separately for every sensor, resulting in a vector with one phase per epoch. Second, we subtracted a potential reference phase from the average phases and calculated the angle of the phase difference per epoch. This difference angle was used to scale steady-state amplitudes of the left-out-run, resulting in the phase-referenced steady-state response *Y* for sensor *m* and epoch *k* as described by **Equation 2:**

Equation 2: $Y_m(k) = A_m(k) \times cos\,(\Theta_m(k) - \Theta_{m,ref})$

`

Where $A_m(k)$ is the amplitude of the left-out run at 10 Hz for every epoch *k* and sensor *m*
$\Theta_m(k)$ is the average phase across all left-out runs at 10 Hz for a given sensor *m*.
$\Theta_{m,ref}$ is the reference phase for the given sensor *m* from the left-in runs

Third, we used our predicted MEG response derived from the pRF parameters on the cortical surface. Using a linear regression, we calculated how much variance in the current phase-referenced steady-state responses of the left-out run could be explained by the predicted MEG sensor responses. Fourth, after computing phase-referenced steady-state response and variance explained for each of the 100 reference phases, we picked the reference phase that resulted in the maximum explained variance for a given sensor in the left-out-run. This procedure was repeated for every sensor.

Once the reference phases were selected, we recomputed the phase-referenced steady-state responses for the entire MEG dataset as described earlier: i.e. subtracting the reference phase from the phase for every epoch, calculating the angle of the phase difference, and multiplying the cosine of difference angle with the amplitude at 10 Hz for every epoch. This resulted in an array with *k* epochs x *l* runs x *m* sensors. MEG data were summarized by taking the average across 19 runs, resulting in a 2-D array (*k* epochs x *m* sensors).

Sensitivity of pRF forward model in predicting MEG sensor responses: systematic variation of pRF parameters

To check how sensitive our model predictions are to changes in the original pRF model estimated by fMRI, we systematically varied the pRF parameters estimated from MRI in two ways: rotate the original pRF centers around the fovea or scale the original pRF sizes.

Rotate pRF centers.

We estimated the sensitivity to pRF center position by systematically rotating the originally estimated pRF centers. We do so by first calculating the polar angle for a given vertex using the x and y pRF parameters, and then adding an angle rotation from -180 to 180 degrees in equal steps of 45 degrees. For every rotation step, we then re-estimate the predicted MEG responses using the forward model. We also re-compute phase referenced amplitude using the reference phase estimated from the new pRF predicted responses. Finally, we calculate the variance explained for every MEG sensor for every rotation step.

We summarize the variance explained for every rotation step by taking the average across a group of sensors selected as the top 10 sensors with highest variance explained in each of the rotation steps. If there are overlapping sensors, we use them only once for

`

averaging. This resulted in a matrix with 9 variance explained values, one for each rotation of pRF center position and the original pRF position (0 degrees rotation).

Scale pRF sizes.

Similarly, we estimate the sensitivity of our model to pRF size by systematically scaling the originally estimated pRF size. We scaled original pRF sizes from 0.2 times smaller to 10 times larger, in 19 log-spaced steps, where a scale factor of 1 is the original pRF size estimated with fMRI. Again, similar to the rotation manipulation, we reperformed our analysis after applying a particular scale factor. For summarizing the effect of scaling, we averaged across a group of sensors selected as the top 10 sensors with highest variance explained in each of the scaling steps. This resulted in a matrix with 19 variance explained values, one for each scale factor applied to the original pRF sizes.

Results

In separate MRI and MEG sessions, subjects viewed high contrast retinotopic bar stimuli traversing across the visual field, where the checkerboards inside the aperture reversed contrast 10 times per second. Data from the MRI session were used to reconstruct population receptive fields (pRFs) on the cortical surface for each individual subject, using the modeling approach described by Dumoulin and Wandell (2008). These pRFs on the cortical surface were the building blocks for our forward modeling approach and were used to predict the observed MEG response. Before describing this model and the quality of the predicted responses, we will first describe the observed components within the MEG data.

Retinotopic stimuli produce reliable steady state responses in posterior MEG sensors

MEG data from individual subjects were divided into 1.1-s non-overlapping time bins (epochs), for every sensor and repeated run. These epochs contained either a contrast-reversing bar at a particular location in the visual field (‘stimulus periods’), a zero-luminance screen (‘blank periods’), or a screen with a black square in the central visual field indicating that subjects could rest their eyes or make excessive eye blinks (‘blink periods’). The latter were removed from all following analyses. Both stimulus and blank periods were averaged across epochs, before transforming the MEG time series to the Fourier domain.

We found a large steady state response at 10 Hz (the contrast-reversal rate of the stimuli) and multiples of 10 Hz (i.e. harmonics) during stimulus compared to blank periods (Figure 3A). These 10 Hz steady state visually evoked fields (SSVEFs) were largest in posterior

`

MEG sensors. To estimate how robust these 10-Hz steady state responses are across runs, we computed two data metrics: the coherence and reliability of the steady state response.

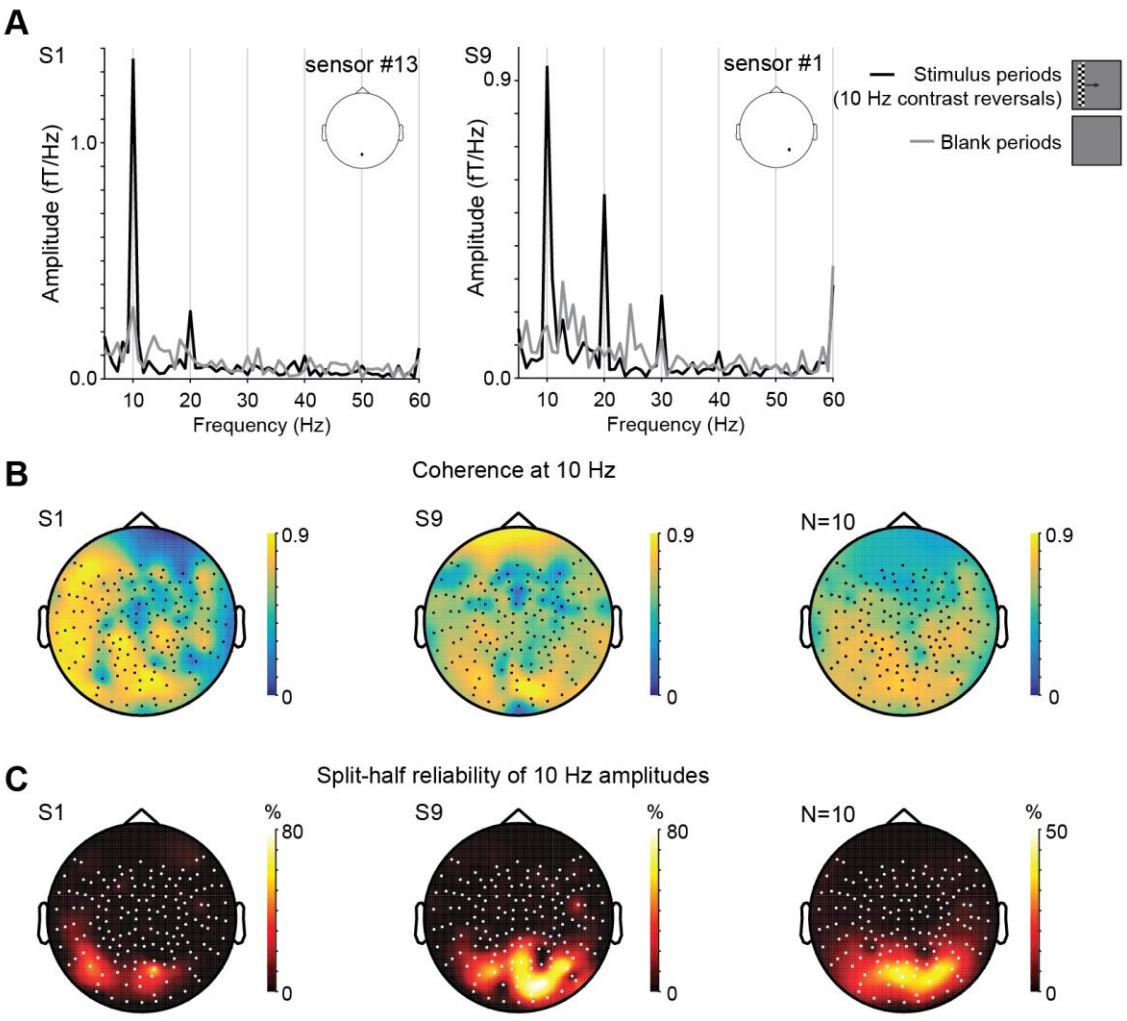

Figure 3. Steady-state visually evoked amplitudes from MEG experiment. (A) Example spectra from two MEG sensors (#1 and #13, location indicated by dot on schematic head) and two subjects (S1 and S9). Stimulus periods show a large peak at the contrast reversal rate known as the 10 Hz steady-state visually evoked field (SSVEF) (black line) and harmonics compared to blank periods (grey line). Note that these amplitudes contain only positive values and are not yet scaled by its referenced-phase. (B) MEG sensor topography of 10 Hz SSVEF coherence (10 Hz amplitude divided by mean of 9-11 Hz amplitude) for subjects S1 and S9 and the sensor-wise average across all subjects (N=10). (C) Split-half reliability of the 10 Hz SSVEF amplitudes for subjects S1 and S9 and the sensor-wise average across all subjects (N=10).

First, we computed the coherence for every MEG sensor. This metric provided a signal-to-noise ratio of the steady-state response within stimulus periods and was defined by dividing

`

the average 10 Hz amplitude by the average amplitudes of 10 Hz and neighboring frequencies (i.e. 9 to 11 Hz). We found that the coherence of the steady state response is largest in posterior sensors (Figure 3B). The large coherence in posterior sensors was in line with the expectation that posterior sensors are located over visual cortex, which were maximally driven by 10 Hz steady state responses.

The specific sensor topography of the steady state coherence varied across subjects. For example, subject S1 showed additional 10 Hz steady state responses with high coherence in lateral and anterior MEG sensors, whereas subject S9 did not. When averaging the coherence metric across subjects, the coherence is largely reduced in anterior sensors and remains high in posterior sensors. This indicates that the 10 Hz steady state amplitudes are most robust in posterior MEG sensors.

The second metric is the split half reliability of the 10 Hz steady state amplitudes. In this case, we split the 19 repeated runs into halves and average across runs within both halves. We then calculate how much variance in the average runs of first half is explained by the second half, and vice versa. We then average the two variance explained values per MEG sensor, resulting in a split half reliability sensor map.

We found that the split half reliability is largest in posterior sensors (up to R^2 = 80 %) in individual subjects and across subjects (see Figure 3C). Interestingly, the sensors with the highest reliability do not always overlap those sensors with the largest coherence within individual subjects. One reason for this discrepancy could be that the coherence metric averages all stimulus epochs, whereas the reliability metric preserves the order of the epochs within a run.

Thus far, we focused only on the 10 Hz steady state Fourier amplitudes and ignored the corresponding 10 Hz phases. Taking the phase information into account will give us additional information about the variability of the 10 Hz steady state response across MEG sensors because the stimulus was moving in different orientations across the visual field. For example, we expect a bar that sweeps from the left to the right side of the visual field, to first drive responses in the right visual cortex before doing so in the left visual cortex. In addition, there might be differences in timing of the 10 Hz amplitudes in MEG sensors because visual information will take longer to reach later visual areas compared to early visual areas. Therefore, to use all available information in the MEG data, we combined both 10 Hz amplitudes and phases into 10 Hz phase-referenced steady state responses. We did so by scaling the 10 Hz amplitudes by the cosine of the difference of the observed phase and a reference phase.

`

A stimulus-referred forward model to predict MEG responses

To predict the MEG responses to retinotopic stimuli, we developed a forward model. In short, our stimulus-referred forward model predicted the MEG responses at every sensor by multiplying the pRF model estimated from fMRI for every cortical location with the MEG stimulus at every time point and then multiplying the resulting responses at every cortical location with the head model based on the anatomy of each individual subject (Figure 2). For the measured MEG responses, we combined amplitude and phase information to obtain the phase referenced amplitude for every sensor. To compute the phase referenced MEG data we determined optimal reference phase for every MEG sensor. For this we phase referenced the MEG amplitudes using a range of reference angles and chose the one that gave the highest variance explained by the model. We used a leave one out cross-validation procedure by splitting the MEG runs into two groups and phase referencing one half with the reference phase estimated with the second half. Finally, to determine the goodness of fit, we compared the predicted time series with the observed 10 Hz phase-referenced steady-state responses averaged across all runs for every MEG sensor.

Forward model can predict visually driven MEG responses in posterior sensors

The MEG time series predicted by our forward model captures the peak responses in the phase-referenced steady-state MEG data with a variance explained of up to ~ 60% within a single sensor located over the back of the head (Figure 4). Amplitude peaks correspond to the responses when bar apertures sweep the visual field in 5 different orientations. One reason for a reduced variance explained for some sensors compared to others is because our forward model underpredicted the data in some of the time points. For example, in subject S9 our model failed to capture the full amplitude of the peak response in the second bar sweep (Figure 4A, second row). There could be different reasons for this which will be discussed in detail in the Discussion.

`

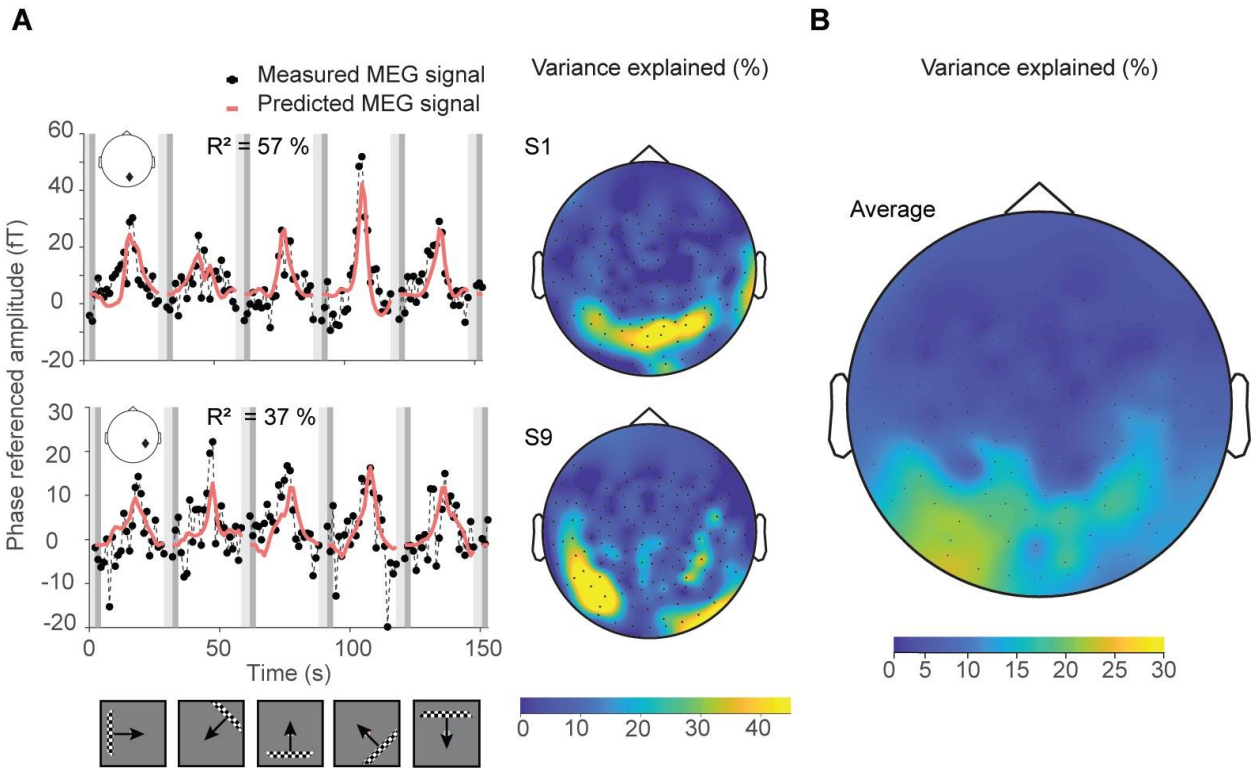

Figure 4. Variance explained of 10 Hz phase-referenced steady-state MEG responses by the stimulus-referred forward model using pRF estimates from fMRI. (A) Left panels show two examples of average 10 Hz phase-referenced MEG responses across runs (black dashed line) and predicted MEG response by the stimulus-referred forward model (red line). The predicted MEG response by the model could explain 57% and 37% of the variance in the measured MEG responses from two posterior sensors in two different subjects (top: S1, bottom: S9). Every dot in the observed MEG time series is the response to a bar position. Light and dark gray boxes indicate blink and blank periods respectively. Blink periods were excluded from the analysis. The sensor location is indicated by the black diamond in the schematic head at the inset on the top left. Right panels show topographic maps of variance explained by model fit across MEG sensors for two subjects shown in the left panel. (B) Topographic MEG sensor map of group average of variance explained by model fit (N=10). Group data were sensor-wise averaged and could explain up to 30% of the variance in the observed MEG signal across posterior sensors.

The sensors with highest variance explained by the forward model were located over the back of the head in both individual subjects and the group average (Figure 4). This agrees with our observation that the coherence and reliability values are largest for the posterior sensors (Figure 3). We find a decrease in the variance explained by the individual sensors for the group average. This is because there is a large inter-subject variation in the variance explained which

`

causes a blurring in the group average (Figure 4B, and see Supplementary Figure S1 for all individual subjects).

Forward model predictions are sensitive to changes in pRF parameters

To determine the extent to which our forward model depends on the accurate estimate of the pRFs (from fMRI data) to predict the variations in the MEG data, we systematically changed the original pRF model parameters estimated from fMRI. We quantified this by a systematic rotation of the pRF positions on the visual field around the fixation point and scaling of the pRF size. In both cases, the ability of the forward model to predict the MEG responses were sensitive to changes in the underlying pRFs on the cortex. We observed a decrease in variance explained in both position and size variations when moving away from the original values as described below.

Changing pRF positions affect the ability to predict MEG responses

In individual subjects, our forward model explained maximum variance when using the pRF positions estimated using fMRI. Variance explained by the model decreased by a maximum of ~15 % when rotated from -180 degrees to 180 degrees around the fixation point in subject S1 (Figure 5A). The specific effect of pRF position variation was not observed in all individual subjects (Supplementary Figure S2). However, on average we observed a maximum variance explained at 0-degree rotation and a maximum drop of ~5% when pRF positions were rotated around the center (Figure 5B).

`

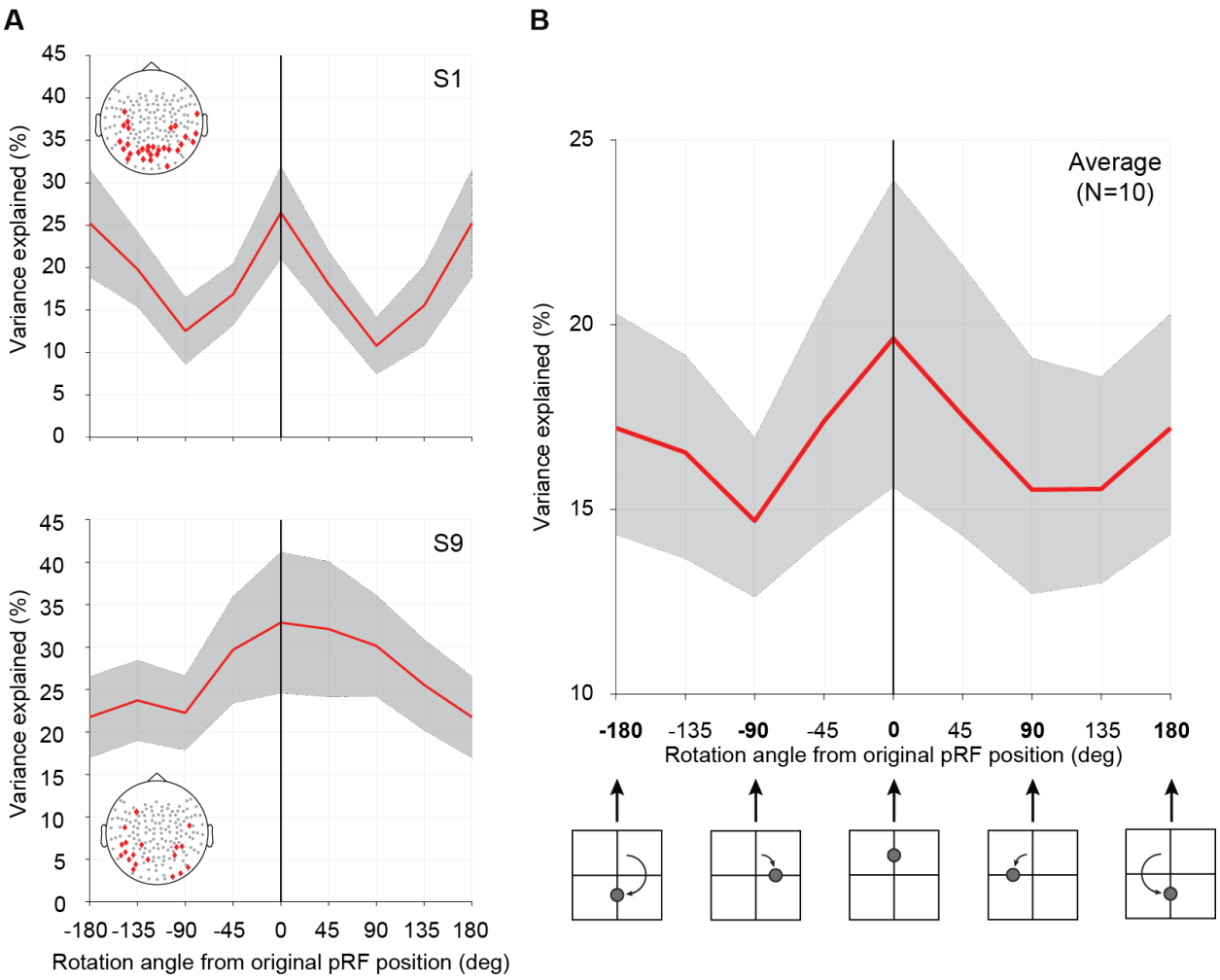

Figure 5. Systematic variation of pRF position decreases ability to explain data by model predictions. (A) Variance explained by the stimulus-referred forward model as a function of pRF center position for two subjects (top: S1, bottom: S9). The position parameter of the pRF estimated with fMRI was systematically rotated around the fovea, from -180 degrees to 180 degrees, and re-fitted to the MEG data. Per subject, sensors with the highest variance explained across all 9 position variations were selected (red dots in schematic head) and averaged (red line). Error bars show 95%-confidence intervals of the average across the selected sensors. Highest variance explained is observed for the original pRF position (0 degrees rotation indicated by the black vertical line). Topographic sensor maps show variance explained for 5 different rotations at the bottom of the graphs (-180, 270, 0, 45, 90, and 180 degrees). (B) Group average of variance explained by model fit (red line) and a 95%-confidence interval obtained by bootstrapping the data from the 10 subjects (gray). A schematic of different pRF positions are shown below. On average, variance explained by the model fit decreases approximately 5% when using pRF positions rotated away from the original pRF position.

`

MEG data is predicted accurately by pRFs smaller than those estimated using fMRI

When changing the pRF sizes, we observed that our forward model explained highest variance when using pRF sizes that was close to but smaller than that estimated using fMRI (Figure 6). This indicates that the ability of the forward model to predict the MEG responses is more sensitive to changes in pRF position than size. Variance explained by the model decreased by a maximum of ~ 16% when scaling the original pRF size in subject S1 (Figure 6A). Similar to position variation, the specific effect of pRF size variation was not observed in all individual subjects (Supplementary Figure S3). On average we observed a maximum drop of ~5% variance explained when the original pRF sizes are scaled (Figure 6B).

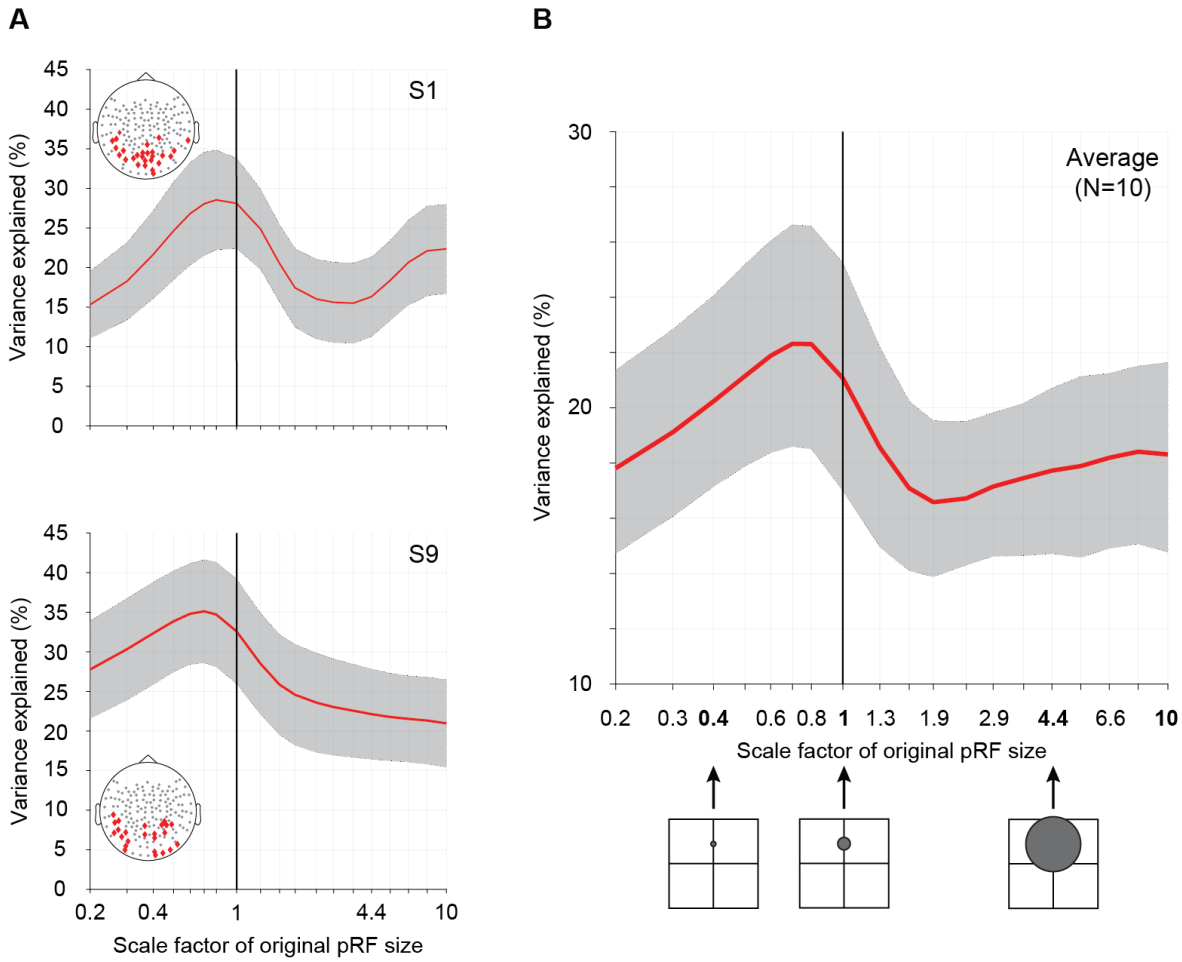

Figure 6. Systematic variation of pRF size decreases ability to explain data by model predictions. (A) Variance explained by the forward model as a function of scaled pRF sizes, i.e. larger or smaller than original pRF size estimated with fMRI, for two subjects (top: S1, bottom: S9). PRF sizes are systematically scaled from 0.2x to 10x the

`

original size. Similar to variations in pRF position, variance explained is averaged for a group of MEG posterior sensors (red dots in the schematic head). Error bars show 95%-confidence intervals of the average across the selected sensors. Both subjects show peak variance explained by the model fit at a pRF size slightly smaller than the original size (scaling factor of 1 indicated by the black vertical line). (B) Group average of variance explained by model fit (red line) and a 95%-confidence interval obtained by bootstrapping the data from the 10 subjects (gray). A schematic of different pRF sizes are shown below. On average, variance explained by the model fit decreases approximately 5% when the pRF sizes become larger or smaller than the original pRF size, similar to the decrement seen when varying the originally estimated pRF position parameter.

Discussion

Overview of results

In this study, we developed a stimulus-referred forward model that can predict MEG responses to a visual stimulation using the pRF model estimated from fMRI. Our model is sensitive to changes in the original pRF model parameters. Our results help to clarify the relation between two different measurements of brain activity along with providing new possibilities for studying the spatiotemporal dynamics of the human visual system at high resolution.

Over-estimation of pRF size by fMRI

One of the important observations from our results is that for the pRF size variation, every subject has highest variance explained when the pRF size is smaller (0.8 times) than the original pRF size estimated from fMRI. For the pRF position variations on the other hand, highest variance explained is observed for the original pRF position estimates from fMRI. Since MEG measures neural activity more directly than fMRI, we believe that pRF size derived from the MEG response is a more accurate reflection of neuronal pRF size than pRF size derived from the BOLD response. Furthermore, PRF estimates from fMRI depend on a number of factors that create a bias towards a larger pRF size but a constant pRF position (Dumoulin & Wandell, 2008).

Some of the neural factors that cause an increase in pRF size estimates include the position scatter and attention. Non-neural factors may also contribute. For example, there is a trade-off between the modelled pRF size and the properties of the hemodynamic response function (HRF) used in the model (Dumoulin & Wandell, 2008; Lerma-Usabiaga, Benson, Winawer, & Wandell, 2020). In addition, pRF sizes were found to increase with eye movements in a previous study (Klein, Harvey, & Dumoulin, 2014; Levin, Dumoulin, Winawer, Dougherty, & Wandell, 2010), although in the present study eye and head movements were controlled during

`

the fMRI as well as the MEG experiment. Since MEG only contains the neural response and not the hemodynamic coupling component present in fMRI, we believe that our method can be a useful tool for updating our existing knowledge about the spatial properties of pRFs estimated from fMRI on top of studying its temporal properties.

A way around inverse models for source localization in MEG

We believe that our model provides an accurate way of estimating sources on the cortex of the MEG responses to visual stimulation. Previous MEG studies that aimed at reconstructing retinotopic maps on the cortical surface from MEG sensor measurements employed MEG source analysis approaches (Brookes et al., 2010; Nasiotis, Clavagnier, Baillet, & Pack, 2017). Briefly, source analysis is a common approach in MEG studies to determine the neural generators of MEG measurements on the cortical surface and can be divided into two important steps. First step is building a forward model of the magnetic fields at a known sensor location that are generated by a current source with known location and orientation. Second step is using the forward model and solving an inverse problem which is: Can we identify the location and orientation of the current source, given the measured magnetic fields outside the skull? The solution to this inverse problem is ill-defined i.e., a measured field from a single source could be resulting from infinite number of current sources (Hadamard, 1952). Multiple approaches have been proposed to solve the problem that each apply different constraints and each give different results (Baillet, Mosher, & Leahy, 2001; Wipf & Nagarajan, 2009). Also, in such source analysis, localization accuracy of MEG sources is computed as the distance between the true activation location and the estimated location. One commonly selected true location is the cortical location that gives highest response in an fMRI experiment (Moradi et al., 2003; Poghosyan & Ioannides, 2007; Sharon, Hämäläinen, Tootell, Halgren, & Belliveau, 2007). Our model tackles these two problems. First, our model defines the sources on the cortex using a stimulus referred pRF model and only use a forward model to predict the magnetic field measurements for every MEG sensor. This provides a way around the ill-defined solution to the inverse problem for predicting the MEG responses to stimuli. Second, since our sources are defined using fMRI directly, it can be argued that we are using the true MEG source locations.

Potential model improvements

Our model, like any other model is not perfect. Below we consider two instances where our model falls short and some potential improvements for it. First, we observed that our model underestimated the peaks in the measured data in the subjects with high variance explained.

`

This could be related to not selecting the correct MEG measurement that underly the neural activity in response to the stimulus. For example, in our study, we used the steady-state stimulus-locked response. However, a previous study found that the broadband signals in ECOG are more related to the BOLD responses (Winawer et al., 2013). Comparing the differences in model performance to broadband and stimulus locked responses could help clarify if a similar relation exists for MEG as well. We also applied a temporal down sampling to the MEG data, which may have been too severe. The underprediction could also be related to the forward model itself. For example, we use the beta values of the pRF fit from fMRI to make predictions on the cortical surface using a smoothing procedure There could be better ways of dealing with the beta value than the one we used here since this free param in pRF fit capture fluctuations in both neural and BOLD response, which could be different for LFP response. Also, in this study we used the basic 2D gaussian pRF model. Our model can be extended by using more extensive pRF models such as the difference of gaussian (DoG) model (Zuiderbaan et al., 2012) or the compressive spatial summation (CSS) model (K. N. Kay et al., 2013), which could possibly capture more complex dynamics.

Second, we observed that our model showed low variance explained in some subjects compared to others. Also, there was considerable differences between the subjects for size and position variations. We believe that this could be the result of both a methodological issue and a true difference between subjects. Methodological issues include improper alignment of the MEG sensor positions with the subject's anatomy and the type and resolution of the head model used. There are multiple head models used in the MEG studies which range from the simple overlapping sphere model we used to complex BEM (Boundary element method) models (Vorwerk et al., 2014). For some subjects, a more accurate modeling of the head could result in the better predictions. Also, we used the head model which maps from all the vertices from a subject's Freesurfer cortical surface to MEG sensors. However, in typical implementations of such head models in Brainstorm, they are down sampled due to computational issues. Subject-related factors such as subject movement, attention, head size, and presence or absence of the hair could also affect the quality of the MEG measurements.

Future extensions and applications

Possibly, the method proposed by Benson and Winawer (2018) can be used to determine pRF model parameters directly from the subject's anatomy using a Bayesian mapping approach, avoiding the participants to go for a fMRI scan session for pRF mapping (Benson & Winawer, 2018). Also, the MEG stimuli were designed such that they were similar to the retinotopic stimuli

`

used for fMRI studies. However, faster stimuli can be used that are not in a temporally predictable sequence, since the MEG responses have a much higher temporal resolution than the fMRI BOLD response.

There are several applications where our model can be used. One important application is to use the model to characterize the changes in pRF properties over time. For example, a previous study, Klein and colleagues have shown a shift in pRF position with attention (Klein et al., 2014). Our forward model can be used to study this change over time by using faster stimuli. Also, our forward model is not limited to the pRF models, but can be possibly be extended to other models that can make predictions on the cortical surface (Harvey, Klein, Petridou, & Dumoulin, 2013; Stigliani, Jeska, & Grill-Spector, 2017; Zhou, Benson, Kay, & Winawer, 2018). Since the brain contains multiple topographic maps, this approach could be used for making predictions of these other maps as well (Harvey, Klein, et al., 2013; Mattay & Weinberger, 1999; Saenz & Langers, 2014).

Conclusion

Neuroscientists use a number of techniques to measure neural activity, each providing different information about brain activity. MEG measures the magnetic field induced by electric currents present in neural activity, whereas fMRI measures the metabolic demands associated with neural activity. In this paper, we have shown that it is possible to use stimulus referred models defined from fMRI responses to predict the MEG responses to retinotopic mapping stimuli. Our results thus support a common underlying mechanism of neural processing measured with the two modalities along with providing new possibilities to study visual processing at a high spatiotemporal resolution.

`

Supplementary figures

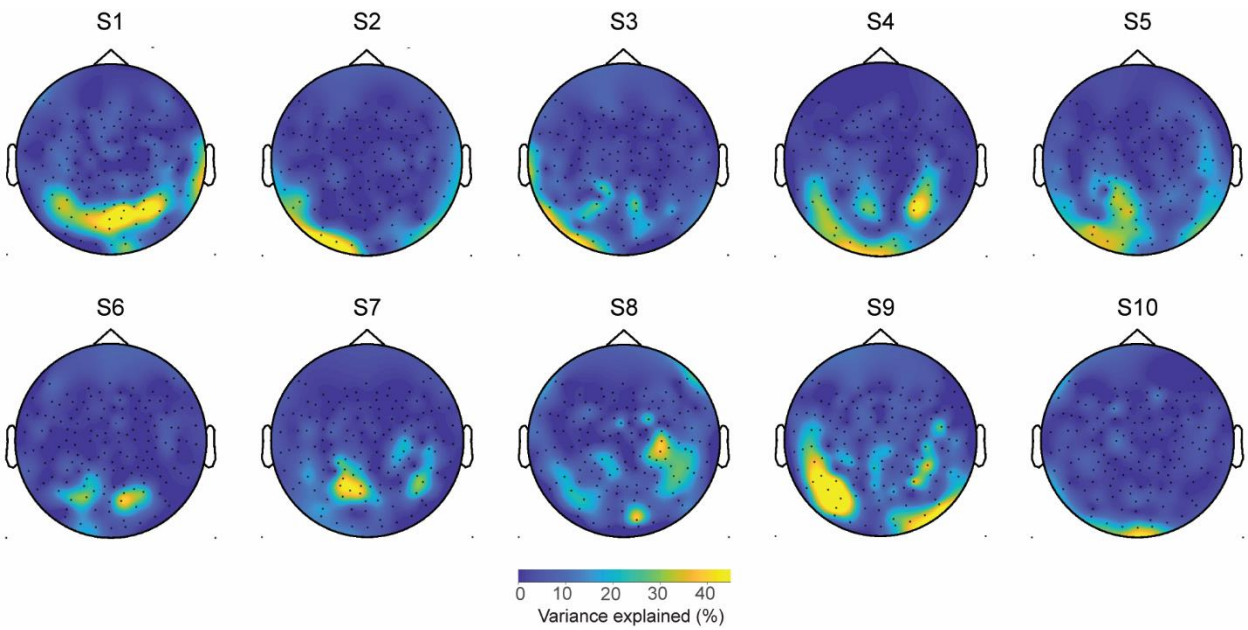

Figure S1. Variance explained by the stimulus referred forward model for all 10 individual subjects. Topographic MEG sensor maps of variance explained by the model predicting the measured 10 Hz phase-referenced steady-state MEG responses. Predicted MEG response by the model explains up to ~60% of the variance in the measured MEG responses in posterior sensors.

`

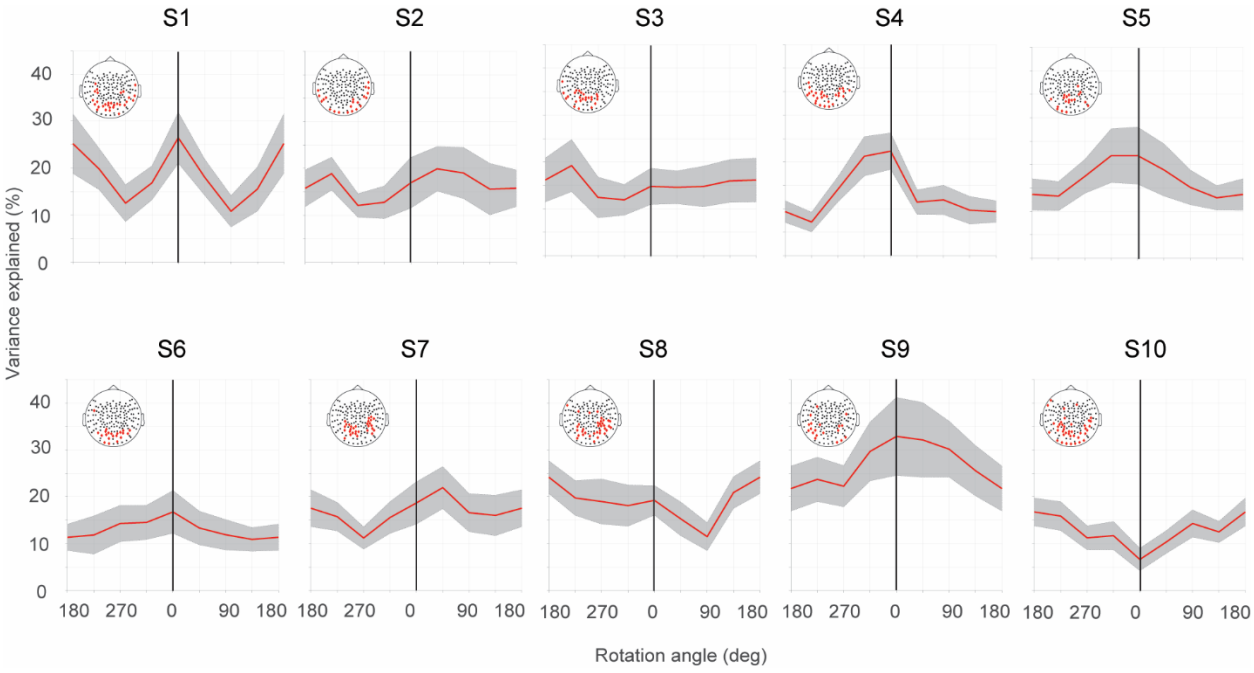

Figure S2. Variance explained by the stimulus-referred forward model as a function of pRF center angle rotation for all 10 individual subjects. The pRFs estimated with fMRI were systematically rotated around the fovea, by -180 degrees to 180 degrees from their original position in steps of 45 degrees. Predicted MEG responses were then recomputed for each of the rotation conditions. Per subject, variance explained values from a group of posterior sensors selected as the top 10 sensors with highest variance explained in each of the 9 rotation conditions were selected (red dots in schematic head) and averaged (red line). Error bars show 95%-confidence interval of the average across the selected sensors. While there are large individual variations, 6 out of 10 subjects have most variance explained in the MEG data when the original pRF positions were used in the stimulus-referred forward model.

`

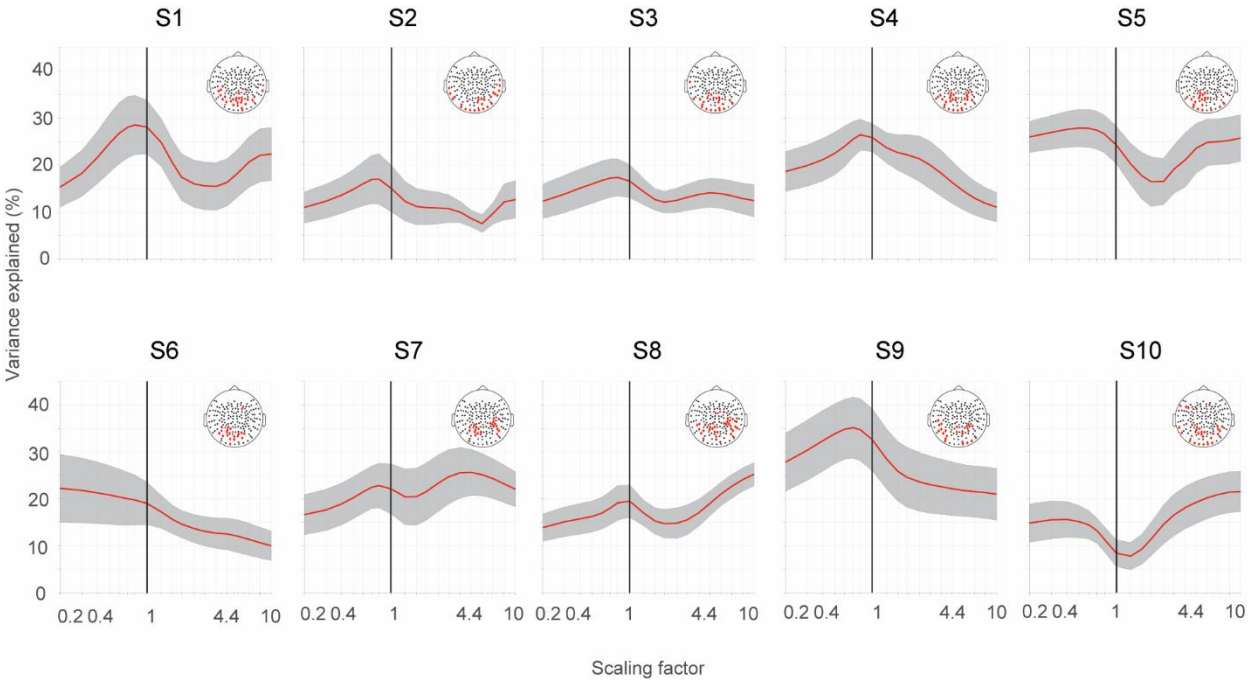

Figure S3. Variance explained by the stimulus-referred forward model as a function of pRF size scale factor for all 10 individual subjects. PRF sizes were systematically scaled from 5x smaller to 10x larger the original size. Similar to variations in pRF position, variance explained is averaged for a group of sensors including the top 10 sensors with the highest variance explained from each of the 19 size scaling conditions (red dots in the schematic head). Error bars show 95%-confidence interval of the average across the selected sensors. Although there are large variations between individual subjects, 6 out of 10 subjects showing a clear peak in variance explained for pRF sizes that are slightly smaller than the original pRF size (a scaling factor of 1). All subjects show a decrease in variance explained when the pRF size is scaled larger than the original pRF size. In some, but not all subject this decrease is followed by an increase in variance explained for very large-scale factors.

`

`

Chapter 3

One in a million: How much do variations in single-neuron receptive fields contribute to population receptive fields?

Akhil Edadan, Demy Vermeij, Serge O Dumoulin (under preparation)

Author contributions

AE and SOD designed the study. AE created the stimuli. AE and DV collected data. AE and DV analyzed data. AE drafted the manuscript. SOD provided critical revisions. SOD provided general supervision and guidance throughout.

`

Abstract

Neurons in the visual cortex respond to stimuli in a specific region in the visual field known as their receptive field (RF). Neurons also have a preferred range of values in other stimulus properties such as spatial frequency. Electrophysiological investigations have shown that spatial frequency preference of single neurons is inversely related to RF size. Here we ask whether this inverse relation is also visible at the neural population level. Using population receptive field (pRF) models and fMRI we studied RF properties of populations of neurons in humans. In this study, we explored the differences in the pRF size across eccentricity (0.5 - 4.5 degrees) in visual field maps V1, V2 and V3 in response to stimuli containing different spatial frequencies (3, 6 and 12 cycles per degree). Contrary to known properties of neuronal RFs, pRF size did not vary with spatial frequency in any of the investigated visual field maps. Interestingly, we did find a decrease in variance explained by the model for higher spatial frequency (12 c/^{o}) at higher eccentricities showing a differential preference for spatial frequencies across eccentricities at a population level. We speculate that differences in neuronal RF size are counteracted by interactions at the population level. Our results indicate that regularities in the properties of individual neurons may play a small role in the behavior of these neurons at the population level.

`

Introduction

Every neuron in visual cortex prefers a region in the visual space where the presence of a stimulus elicits a response from the neuron, known as neuronal receptive field (RF). In addition to locations in the visual field, such a neuron is also selective for other visual features such as shape, orientation, and spatial frequency (Hubel & Wiesel, 1961, 1962, 1968, 1974). In animals, invasive single unit recordings and optical imaging techniques are used to study the properties of features preferred by single neurons or a small group of neurons. In humans, non-invasive techniques like fMRI along with computational models are predominantly used to determine the RF properties of a population of neurons. These models are referred to as population receptive field (pRF) models (Dumoulin & Wandell, 2008; K. N. Kay et al., 2013; Zuiderbaan et al., 2012). The most basic pRF model characterizes the population RFs with a preferred position (x, y) and size (σ), which reflects the RF properties of the individual neurons that constitute the populations. Given the typical neural densities (50,000 neurons per cubic mm of cortex) and conventional fMRI resolutions (2x2x2 mm), about 400,000 neurons can contribute to the pRF (Leuba & Garey, 1989; Rockel et al., 1980). Standard pRF mapping uses a full contrast checkerboard stimulus to elicit neuronal responses from a wide range of neurons in the population to get a good signal to noise ratio. However, some recent studies have also used stimuli that can elicit responses from a more focused population of neurons to study their properties in detail (Alvarez, De Haas, Clark, Rees, & Schwarzkopf, 2015; Dumoulin et al., 2014; Dumoulin & Knapen, 2018; Harvey & Dumoulin, 2016; Yildirim, Carvalho, & Cornelissen, 2018). In this study, we are investigating the properties of a specific population of neurons which are selective to spatial frequency content in a stimulus to determine if the neuronal RF properties are reflected in the population receptive field properties.

Spatial frequency selectivity is one of the fundamental features of vision that is studied thoroughly. In animals, electrophysiology and optical studies have identified neurons selective for different spatial frequencies (Campbell & Robson, 1968; Enroth-Cugell & Robson, 1966; Maffei & Fiorentini, 1973). Further studies in monkey V1 have shown that the preferred average spatial frequency of neurons decreases as a function of eccentricity (De Valois, Albrecht, & Thorell, 1982; Tootell, Silverman, Hamilton, Switkes, & De Valois, 1988; Xu, Anderson, & Casagrande, 2007). fMRI studies have also investigated the spatial frequency selectivity of population of neurons in humans and identified a similar decrease in spatial frequency preference across eccentricity (Henriksson, Nurminen, Hyvärinen, & Vanni, 2008; Sasaki et al., 2001). Some studies have also investigated the link between spatial frequency preferences of

`

neurons and their spatial RF size. In macaque V1, neurons selective to higher spatial frequencies were found to have smaller RF size and neurons selective to lower frequencies to have larger RF (De Valois et al., 1982; Schiller, Finlay, & Volman, 1976). This also agrees with the findings that low spatial frequency information is conveyed through magnocellular pathway known to contain cells with large RF size, whereas high spatial frequency is conveyed through parvocellular pathway known to have cells with small RF size (Hicks, Lee, & Vidyasagar, 1983; Kaplan & Shapley, 1982; Van Essen & DeYoe, 1995). However, no study has specifically reported a systematic change in pRF size with spatial frequency or eccentricity.

Here, we investigate the spatial frequency selectivity of population of neurons by systematically exciting them with stimuli containing different spatial frequencies and measuring the change in their pRF properties. To this aim, we used stimuli that contained three different spatial frequencies, 3 c/^{o} (cycles per degree), 6 c/^{o}, and 12 c/^{o} to probe the changes in the pRF size (σ) across spatial frequencies and eccentricities. If single-neuron RFs are reflected in the neural population RFs, we anticipate to find that different frequency content in the stimuli will excite the population of neurons sensitive to the corresponding frequency and in turn will cause the estimated pRF size to decrease with increasing spatial frequency. However, other factors contribute to the pRF as well, such as extra-classical RF interactions, and both random and systematic variations in RF positions. If the neuronal RF is only a small contributor to the entire neural population RF, we may not find a relationship between spatial frequency and pRF sizes.

Methods

Subjects

Ten (10) subjects (7 males, age range 26 – 46 (M = 30.7 years, SD = 6.25 years)) participated in the study. One subject was excluded because of poor data quality due to technical issues associated with the scanner. Results shown here are from the remaining 9 subjects. All studies were performed with the informed written consent from the subjects. Study was approved by the Human Ethics Committee of University Medical Center Utrecht in accordance with the World Medical Association's Declaration of Helsinki.

`

Stimuli

Stimuli consisted of a stimulus carrier containing band-passed filtered noise (as shown in figure 1, containing 3,6 and 12 c/^{o}, chosen based on the frequency values used in the CSV-1000e contrast sensitivity tests in clinics) revealed through a bar aperture with the edges smoothed using a raised cosine (frequency = 1.7 c/^{o}), that swept across the visual field in discrete steps in 8 different bar configurations for a given scan (4 different orientations (0, 45, 90, 135 degrees) with two step directions for each orientation). The width of the bar aperture subtended 1/4th of the stimulus radius (1.5 and 5 degrees of visual angle, respectively). Each bar position lasted for a duration of 30s and the mean luminance block for 15 s. There was an extra 15 s of mean luminance block at the end of every scan, making the last blank last for 30s. Thus, total duration of one scan run was 315 seconds. We ran 3 scans with spatial frequency 3 c/^{o}, 6 c/^{o} and 4 scans with spatial frequency 12 c/^{o} per subject during one scan session. We adjusted the root mean square (RMS) contrast, calculated as the standard deviation of the pixel intensities, for all the individual spatial frequency stimuli be the same (RMS contrast = 10 %).

The spatial frequency content of the stimuli was meant to activate the neurons selective for the corresponding spatial frequency and in turn affect the estimated pRF size parameters. The chosen stimulus will influence the pRF properties in the following manner: the size (σ_{pRF}) estimate from the pRF model depends on both neuronal and non-neuronal factors (Dumoulin & Wandell, 2008; A. T. Smith, Singh, Williams, & Greenlee, 2001) and their contribution to total size σ_{pRF} can be given by:

$$\sigma_{pRF}^2 = \sigma_{nRF}^2 + \sigma_{pv}^2 + k, \qquad (Equation\ 1)$$

Where, σ_{nRF} represent the RF size of individual neurons, σ_{pv} reflect the position scatter of neuronal RF and k stands for the non-neuronal factors. Different spatial frequency content in the stimulus can activate different neuronal populations and hence change the σ_{nRF}. Since we are comparing the pRF properties from the same fMRI voxel, σ_{pv} can be considered to be same in every measurement. Thus, the RF size of the population of neurons should be equal to the RF sizes of the individual neurons constituting the population.

Subjects performed a fixation dot task, in which the central fixation dot changed color and subjects were asked to report the change using a button press. Accuracy of the fixation dot was recorded as percentage of correct responses out of the total number of changes. All subjects had an accuracy of over 90% correct in the fixation dot task.

`

All stimuli were shown on a MR compatible and gamma corrected 32-inch BOLD screen from Cambridge systems (32 inches, 1920 x 1080 pixels, refresh rate of 120 Hz) using PsychToolbox (Brainard, 1997; Pelli, 1997) at 210 cm from the subjects' eyes. Subjects viewed the stimuli reflected through a mirror attached to the coil of the scanner.

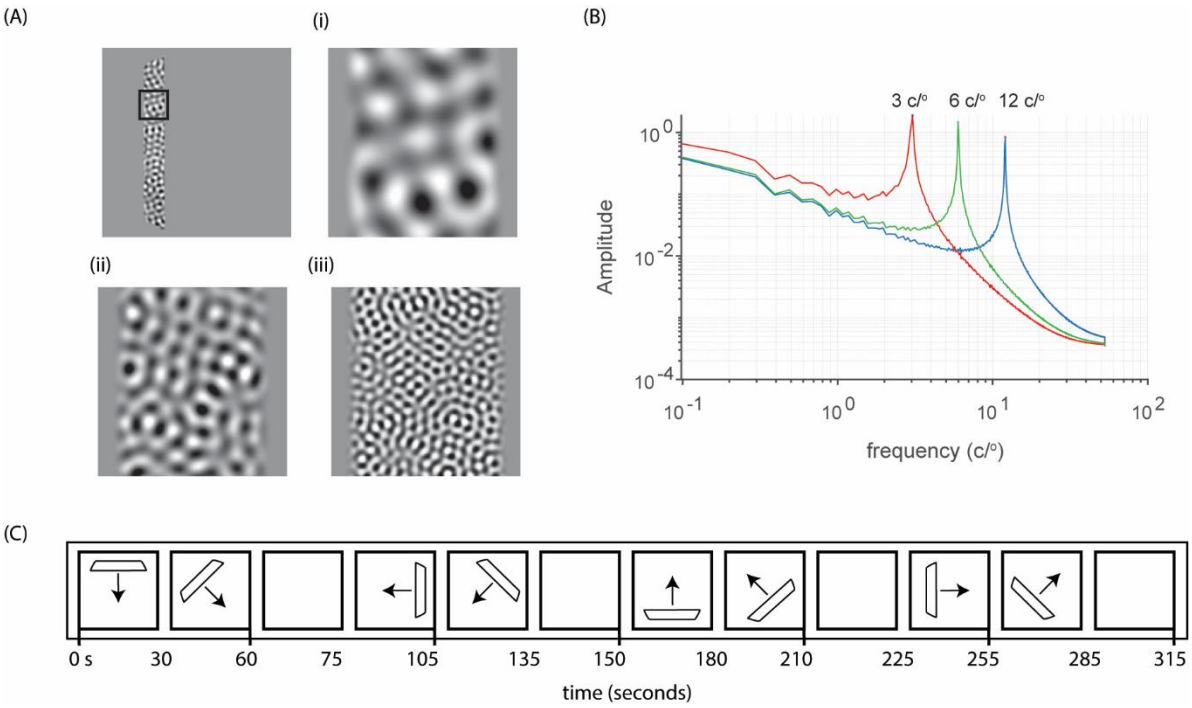

Figure 1: Stimuli. (A) Example images showing one bar position of 3 c/°. The square indicates the section enlarged with examples for the three different stimulus conditions, (i) 3 c/° (ii) 6 c/° (iii) 12 c/°. The square was not present in the actual stimulus presentation. RMS contrast for the individual spatial frequency conditions were set to 10 % (B) Power spectrum showing the frequency content of individual images used in the scan, with red showing 3, green showing 6 and blue showing 12 c/°. Power spectrum was computed for images shown in every frequency condition only for the region within the bar aperture. The power spectra reveal the dominant spatial frequency in the stimulus, but also reveal that other spatial frequencies are present as well. (C) Schematic representation of the bar positions over time (in seconds) for individual spatial frequencies. The bar aperture swept through the visual field in 30 s (20 TRs) in 8 directions with a mean luminance blank period (0% contrast) of 15 s after every oblique direction for the fMRI signal to return to the baseline.

`

MRI acquisition

Anatomical scans were acquired using a 3D T1-weighted MP2RAGE sequence (TR - 6.2 ms, TE - 3 ms, flip angle - 5 degrees, FOV - 220 x 220 x 164 mm, voxel size - 0.6x0.6x0.6 mm) (Marques et al., 2010). Functional T2* weighted 2- dimensional EPI scans (2D-EPI, TR – 1.5s, TE – 22.5 ms, Flip angle – 65 degrees, FOV –216 x 216 x 97 mm, voxel size - 1.8 mm isotropic, 57 slices) were acquired using a Philips 7T scanner. Each subject completed 10 functional runs in each session with 3 runs for 3 c/^{o} and 6 c/^{o} and 4 runs for the 12 c/^{o} conditions.

Processing of anatomical and functional data

Anatomical scans were segmented into gray and white matter using an automatic segmentation pipeline using TOADS/CRUISE algorithm in MIPAV (Bazin & Pham, 2007) and hand corrected to minimize segmentation errors (https://www.slicer.org/). Functional data was preprocessed using AFNI (Cox, 1996) and the Matlab based Vistasoft toolbox (http://white.stanford.edu/software). Raw data were motion corrected using the AFNI command 3dvolreg. Between scans motion correction was performed by aligning the first functional volume of each scan with every other scan. Within scans motion correction was done by aligning all the frames to the first frame. We corrected the scans for geometric distortions due to the magnetic field inhomogeneities. This was done by acquiring an EPI scan with a phase encoding direction opposite to the original EPI and applying a non-linear warping (Andersson et al., 2003).

We then coregistered the motion corrected and distortion corrected scans on the T1 weighted anatomy. The center of mass of the functional image was aligned with the center of mass of the anatomy, providing a good starting point to perform an affine transformation using the AFNI function, 3dAllineate. Results of the coregistration was assessed manually by visual inspection using various anatomical markers such as the boundaries for gray matter/ white matter and gray matter/ cerebrospinal fluid. Functional scans from all runs and runs from each of the conditions (spatial frequencies 3, 6 and 12 c/^{o}) separately were averaged and interpolated to the anatomical segmentation. The pRF-model was then run on the resulting functional scans using the vistasoft toolbox (Dumoulin & Wandell, 2008).

`

pRF analysis

We estimated the pRF properties (position and size) for every cortical location using the pRF model (Dumoulin & Wandell, 2008). Briefly, a population receptive field for every cortical location is modeled as a 2-dimensional gaussian with parameters for its position (x, y) and size (σ). A predicted time course for every stimulus position is made combining the stimulus, model and the hemodynamic response function (HRF). The predicted time series is then compared to the measured fMRI time series and the model parameters that give the least residual sum of squares is used as the pRF properties for that cortical location.

Specifically, for this study we computed the pRF parameters for each cortical location using the averaged functional data from all the runs (individual spatial frequency conditions, 3, 6, and 12 c/^{o}). After estimating the pRF parameters using a standard canonical HRF (Boynton et al., 1996; Friston et al., 1998), we ran an HRF fit over the cortical locations where the pRF model explained more than 10% of variance in the previous step, keeping all the pRF parameters constant (Harvey & Dumoulin, 2011). pRF parameters were then adjusted using the estimated HRF. We converted the resulting pRF parameters (x, y, sigma) to the traditional eccentricity and polar angle maps. We then delineated three visual areas (V1, V2, and V3) using these maps (Wandell, Dumoulin, & Brewer, 2007).

pRF size parameters (sigma) for the individual conditions were refined using an optimization algorithm (Fletcher & Powell, 1963) while keeping the position (x, y) and the HRF constant. We then determined a linear function that describes the relation between pRF size and eccentricity for each visual area. We compared the slope and intercept from the linear function across different conditions. We performed a one-way ANOVA to determine whether the differences were significant for individual visual field maps across different conditions.

Results

Example pRF fits

We recorded the fMRI BOLD time series from all cortical locations in visual field maps, V1, V2 and V3. An example time series from a single cortical location from V2 shows peaks corresponding to the instances when the stimulus bar passed the RF of the population of neurons in the cortical location (figure 2A). Model fits for the high spatial frequency condition (12 c/^{o}) generally had lower variance explained in the measured time series compared to other spatial frequency conditions, even though we collected more data for this condition.

`

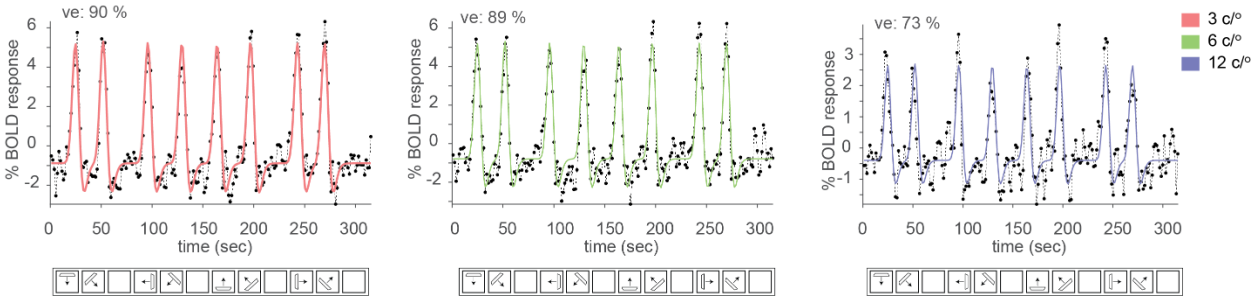

Figure 2: Example time series from a cortical location of an example subject. Black dashed lines in each panel indicate the measured time series from a cortical location in V2. Colored solid lines represent the predicted time series, with red, green, and blue showing 3, 6, and12 c/° respectively. Overall, model explained more than 70 % of variance in the estimated time series. A schematic diagram in the bottom shows the directions of bar pass.

Differences in variance explained between different spatial frequencies

Next, we compared variance explained by the pRF model for the different spatial frequencies. For spatial frequency condition 3 and 6 c/°, we found little variation in variance explained as a function of eccentricity and overall the model captured more that 40% of the variance in the data. In contrast, for the spatial frequency condition of 12 c/°, we find a decrease in variance explained by the model with eccentricity for individual subjects and average across subjects (Figure 3). We further compared the slopes of individual spatial frequencies against each other and found a significant decrease in the slope for the variance explained versus eccentricity relation for spatial frequency 12 c/° compared to 3 c/° ($t_{(16)}$ = 3.79, p = 0.0016 for V1, $t_{(16)}$ = 3.72, p = 0.0018 for V2 and $t_{(16)}$ = 2.18, p = 0.04 for V3) and 6 c/° ($t_{(16)}$ = 3.27, p = 0.004 for V1, $t_{(16)}$ = 3.29, p = 0.004 for V2). For V3, the difference was not significant between spatial frequency 12 c/° and 6 c/° ($t_{(16)}$ = 2.07, p = 0.054). Thus, we find that the variance explained as a function of eccentricity differs between the different spatial frequencies, presumably due to the decrease of neurons tuned to higher spatial frequencies at higher eccentricities (De Valois et al., 1982; Henriksson et al., 2008; Xu et al., 2007).

`

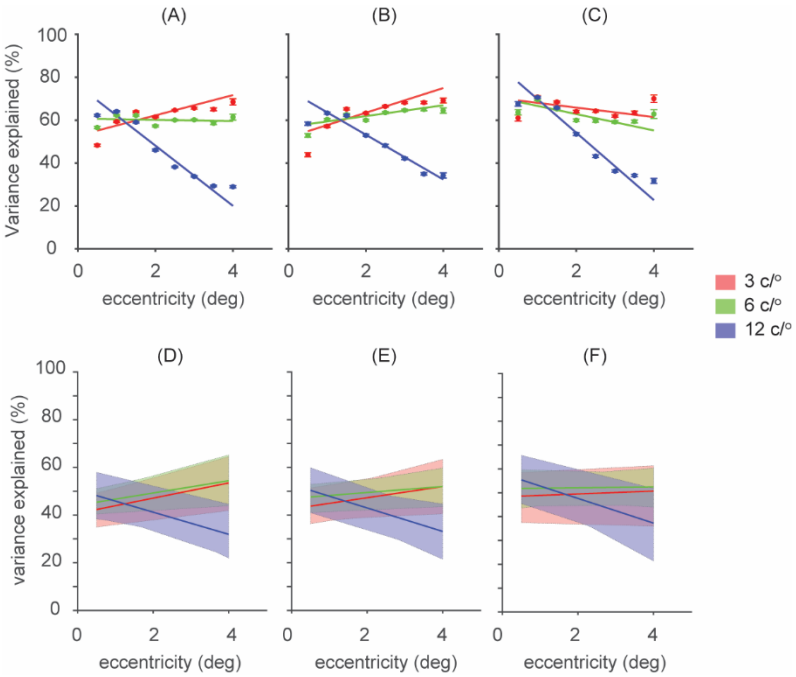

Figure 3: Relationship between variance explained with eccentricity. Variance explained plotted against eccentricity for one example subject (shown in first row) and average across 9 subjects with 95 % confidence interval of the distribution obtained by bootstrapping the slope and intercept values from individual subjects (shown in second row) for the three visual field maps, V1 (panels A and D), V2 (panels B and E) and V3 (panels C and F). Red, green and blue represent the data for 3, 6 and 12 c/° respectively. Variance explained by the model is decreasing with eccentricity for 12 c/° for all visual field maps compared to 3 and 6 c/°.

No differences in pRF size between different spatial frequencies.

We found an increase in the estimated pRF size with eccentricity for all fMRI voxels in the V1, V2 and V3 when averaged across subjects (figure 3B). For some subjects, the increase in pRF size was not observed in V1 (Supplementary figure 1). Despite the variance explained differences, we did not observe a decrease in pRF size for spatial frequencies 12 c/° compared to 3 and 6 c/° (figure 3B). Also, we did not observe a significant difference in the pRF size between different spatial frequencies for visual field maps V1, V2 and V3 across the 9 subjects (All $F_{(24,2)} < 0.88$, all $p > 0.42$).

`

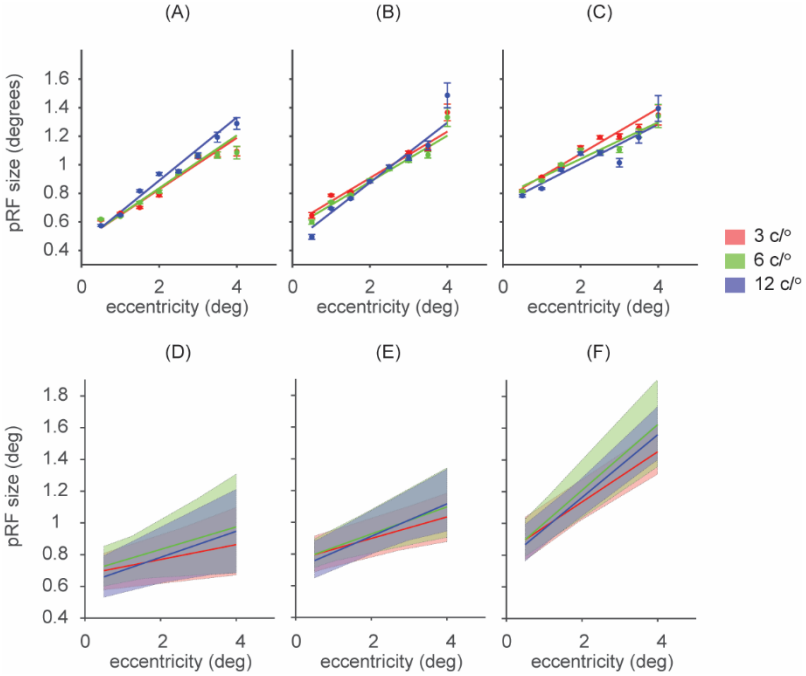

Figure 4: Relationship of pRF size with eccentricity. pRF size plotted against eccentricity for one example subject (shown in first row) and average across 9 subjects with 95 % confidence interval of the distribution obtained by bootstrapping the slope and intercept values from individual subjects (shown in second row) for the three visual field maps, V1 (panels A and D), V2 (panels B and E) and V3 (panels C and F). Red, green and blue represent the data for 3, 6 and 12 c/° respectively. pRF size is increasing with eccentricity for all spatial frequency conditions and visual field maps with no significant difference between the conditions.

Discussion

We compared pRF sizes of neurons selective to different spatial frequencies. We observed a decrease in variance explained by the model with increasing eccentricity for higher spatial frequency (12 c/°) and not for lower spatial frequencies (3 c/° and 6 c/°) suggesting a preference for higher spatial frequencies in the lower eccentricities compared to higher eccentricities. Although we find differences in variance explained by the pRF model, we did not find a significant difference in pRF size between different spatial frequencies.

Apart from the individual RF sizes, pRF sizes estimated using pRF models are also influenced by other factors. Below we discuss whether our measured pRF sizes are affected by such factors. PRF sizes measured using pRF models capture both classical RFs and extra-

`

classical RFs (Dumoulin et al., 2014). Extra-classical RFs are known to be present due to the intrinsic long-range cortical connections and are generally observed during the intercellular interactions necessary for processing complex stimuli such as natural images. Although we have limited such contextual interactions by using band-pass noise stimuli, which do not have any statistical regularities, it is still possible and likely that extra-classical interactions occur. We speculate that these may compensate for differences in classical RF sizes, particularly when RF sizes are small causing RFs to stay the same at the population level. This hypothetical counterbalance between classical and extra-classical RFs could explain the difference between known regularities in the RF sizes at the level of single neurons and our results at the level of neural populations.

Spatial frequency preferences of neurons are known to be influenced by the luminance contrast at which the stimuli are presented (Henriksson et al., 2008; Lu & Roe, 2007). A higher preferred spatial frequency optimum was observed for lower contrasts by Henriksson and colleagues. Specifically, they observed that the highest % BOLD signal change for V1 was at a spatial frequency of 1.2 c/^{o} at 1.7^{o} and 0.18 c/^{o} at 19^{o} at high contrast (82 % Michelson contrast) (Henriksson et al., 2008). The spatial frequencies (3, 6 and 12 c/^{o}) that we chose could thus fall in the high frequency optimum of these neurons. This would suggest that spatial frequencies lower than 2 c/^{o} or contrasts lower than 10 % RMS contrast would have optimally excited the neurons that respond to low spatial frequencies. However, due to technical limitations we could not use either of these stimulus settings. Lower spatial frequencies will increase the wavelength such that it covers the entire bar (1.5^{o}) width. Reducing the contrast below 10 % on the other hand would reduce the signal to noise ratio considerably. Also, we used a constant 10 % RMS contrast for all the spatial frequency conditions which in turn caused a lower perceived contrast for higher spatial frequencies compared to lower spatial frequencies. This could have counteracted the decrease in pRF size with spatial frequencies since low contrasts are typically known to cause larger pRF size in the single neuron level (Sceniak, Hawken, & Shapley, 2002). Using stimuli with a fixed perceived contrast could help to understand the effect of perceived contrast on pRF size.

Another factor that can influence the estimated pRF size is the position scatter of the individual neurons in the population. pRF measurements at a given location in the visual field is determined by the mean RF of individual neurons and also the scatter around the mean location. Previous neurophysiological data have shown that RF scatter increases with RF size and eccentricity (Dow, Snyder, Vautin, & Bauer, 1981; Hetherington & Swindale, 1999; Hubel &

`

Wiesel, 1974). Given that RF scatter increases with RF size, it is unlikely that RF scatter influenced our results. However, the RF scatter could also change depending on the number of neurons within the recording site. Even though we compared neuronal populations from the same cortical locations, different sub population of neurons excited in each of the spatial frequency conditions could result in different scatter. However, previous studies have shown that such a sparse sampling of neurons from a population can affect the amplitude of the neuronal response (Yildirim et al., 2018) but not position scatter (Clavagnier, Dumoulin, & Hess, 2015). So, we do not believe that our results are due to the position scatter of individual neurons.

Hard edges in the bar aperture will introduce a broad range of frequency components in the stimulus. To avoid these broadband frequency components from driving neuronal responses, we windowed the bar edges with soft raised cosine edges. For the raised cosine, we used a frequency smaller than our smallest frequency (1.7c/^{o}). Arguably, the responses are driven by the low frequency edges in all conditions and hence the same in all conditions. But a previous study have provided evidence that a contrast-reversing checkerboard stimulus generate response at the spatial frequency content of a moving ring stimulus and not to the edges (Engel, Glover, & Wandell, 1997). Thus, we consider it unlikely that our results are driven solely by the responses to the raised cosine edges.

Previous studies have found that attention can modulate the responses in the attended location (Kastner, De Weerd, Desimone, & Ungerleider, 1998; Murray & Wojciulik, 2004; O'Craven, Downing, & Kanwisher, 1999; Wojciulik, Kanwisher, & Driver, 1998). Attention can also have an influence in both the pRF size and position estimates (Klein et al., 2014; van Es, Theeuwes, & Knapen, 2018). However, we don't think that the pRF sizes observed in our results are influenced by an attention towards the stimuli. Firstly, attention related changes are typically observed in all the visual field maps and increase higher up the visual hierarchy (Buffalo, Fries, Landman, Liang, & Desimone, 2010; Cook & Maunsell, 2002; Klein et al., 2014; Montijn, Klink, & Van Wezel, 2012; O'Connor, Fukui, Pinsk, & Kastner, 2002; Posner & Gilbert, 1999). But in our results, we do not find any increase in the difference with visual hierarchy. Second, the subjects performed an attention task in the center of the screen and all subjects performed equally well in all conditions. Therefore, we do not believe that differences in attention are influencing our results.

Non-neural factors such as eye movements and head movements will also affect pRF sizes. However, we don't think that these effects influence our results. Previous studies

`

simulating the effects of eye movements in the pRF size estimation have found that it causes an increase in the pRF sizes for all the visual field maps, which was not observed here (Klein et al., 2014; Levin et al., 2010). Moreover, almost all the subjects showed an accuracy of over 90% in the fixation dot task, indicating proper fixation. Head movement during the scan can also cause changes in the fMRI responses and hence affect the pRF model parameters. So, head motion was minimized during the scan using foam padding, and a motion correction algorithm was used to correct for any motion artifact in the data (Cox, 1996). Head motion was found to be less than one voxel size for most subjects for most runs, for which a previous study did not observe any large effects in the estimation of the pRF parameters (van Dijk, de Haas, Moutsiana, & Schwarzkopf, 2016). The presence of motion artifacts causes noisy measured responses and a reduced model prediction accuracy. However, our results showed above 70% variance explained between the model predictions and the fMRI responses. Therefore, we do not believe that eye movements or head movements can explain our results.

Conclusion

In summary, we have provided evidence for a difference in the preference for high and low spatial frequencies at different eccentricities through a decrease in the ability of the model to predict responses to higher spatial frequency at larger eccentricities. Also, we have shown that there is no difference in the pRF size values between different spatial frequencies across eccentricities, even though there are evidences that RF size decreases with spatial frequencies at a neuronal level. Thus, our findings show that the properties at the neuronal level can differ from those estimated in the population level.

`

Supplementary figure

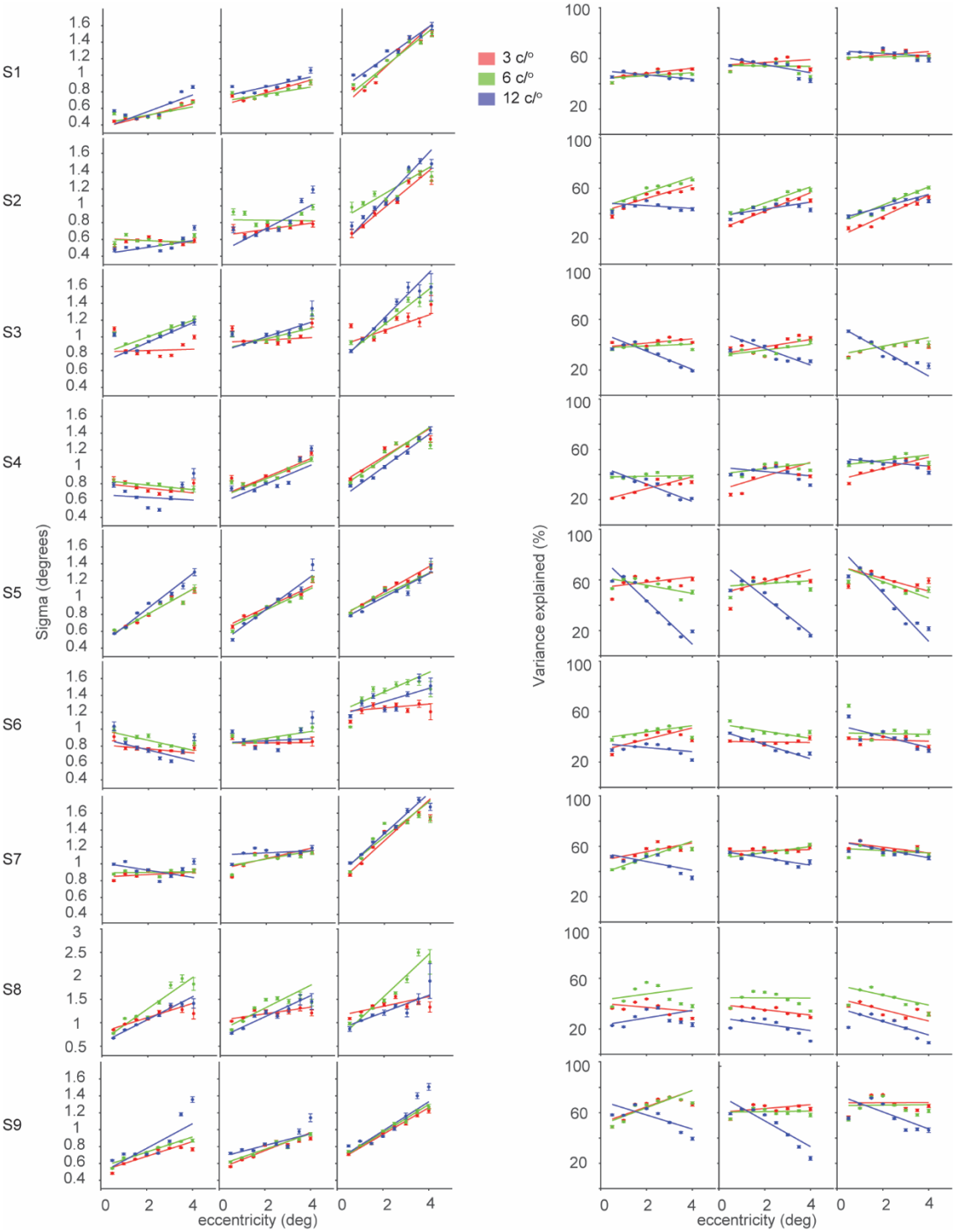

Figure S1: pRF size versus eccentricity fit and variance explained versus eccentricity fit for individual subjects for spatial frequencies 3 c/° (red), 6 c/° (green) and 12 (blue) c/° and visual field maps V1, V2 and V3 (shown in columns

`

1,2 and 3 respectively). Lines show the fits to the distribution of values and the dots with error bars depict the mean of the values in 8 bins and the standard error of the mean. pRF size shows an increase with eccentricity for all subjects in V2 and V3. For V1, some subjects do not show a positive slope. Variance explained values are decreasing with eccentricity for spatial frequency 12 c/^{o} for all subjects.

`

Chapter 4

Early extra-striate cortex supports receptive field interactions to process natural images

Akhil Edadan, Wietske Zuiderbaan, Maartje C. de Jong, Serge O Dumoulin (under review)

Author contributions

AE and SOD designed the study. AE and WZ created the stimuli and AE collected data. AE, MCDJ and WZ analyzed data. AE drafted the manuscript. SOD, MCDJ and WZ provided critical revisions. SOD, MCDJ and WZ provided general supervision and guidance throughout.

`

Abstract

Every neuron in the visual cortex processes a limited region in the visual field known as its classical receptive field (RF). Intercellular interaction beyond this classical RF, i.e. extra-classical interaction, is required to process the information rich natural scenes we experience every day. Here, we investigate where in the visual cortex, these intercellular interactions responsible for the extra-classical RF interactions in natural images occur. For this, we use 2 different stimuli: natural images and phase scrambled versions of the images. Phase scrambling removes the statistical regularities in natural images but maintains the low-level characteristics. Removing the statistical regularities reduces the contextual interactions and thereby result in a smaller RF compared to natural images. We use functional magnetic resonance Imaging (fMRI) and population RF (pRF) modelling techniques to characterize and compare the pRF properties of neurons in response to both the natural stimuli and the phase scrambled stimuli. We observed that pRF sizes determined using natural images are larger compared to the phase scrambled condition in V1, V2 and V3. We conclude that the increased intercellular interactions responsible for processing higher order statistical regularities in natural images are encoded in early extra striate visual field maps (V1, V2 and V3).

`

Introduction

Much of visual cortex is organized in retinotopic maps with every neuron responding to a certain region in the visual field, known as its receptive field (RF). The RF is often divided into the classical and extra-classical RF. Stimulation in the classical RF directly modulates neuronal responses. Classical RFs are typically characterized using simple stimuli such as dots and lines and are selective to properties such as orientation, position, spatial frequency, and direction of motion (Andrews & Pollen, 1979; Hartline, 1940; Hubel & Wiesel, 1961, 1962, 1968; Kulikowski, Marčelja, & Bishop, 1982; Spillmann, 2014; Von Baumgarten & Jung, 1952). Stimulation in the extra-classical RF indirectly modulates neural responses depending on the stimulus characteristics in both the classical and extra-classical RF and may be described as contextual interactions. Natural images, for example, are complex stimuli containing simple features such as local luminance edges or oriented curve tangents which interact with each other resulting in different statistical properties. Our visual system is shaped and refined during the process of evolution to adapt to the visual scenes that are commonly found in nature, and hence processing these contextual interactions plays a crucial role in the working of visual system.

A large group of studies have investigated the neural mechanism underlying contextual interactions (Allman et al., 1985; Fitzpatrick, 2000; Gilbert & Wiesel, 1990; Jones et al., 2002; Knierim & Van Essen, 1992; Sillito, 1995). These studies have found that contextual interactions require integration of information beyond the classical receptive fields, known as the extra-classical receptive field which enables a transition from local to global processing (Kapadia et al., 1995; C.-Y. Li, 1996; Maffei & Fiorentini, 1976; Sengpiel, Sen, & Blakemore, 1997; Vinje & Gallant, 2000; Walker, Ohzawa, & Freeman, 1999). Stimulation of these extra-classical regions by themselves do not activate the neurons but can modulate its activity leading to a variety of perceptual phenomena, such as contour integration (W. Li, Piëch, & Gilbert, 2006), figure-ground segregation (V. A. Lamme, 1995), perception of uniform surfaces, filling-in and grouping (Grossberg & Mingolla, 1985; V. A. F. Lamme, Super, & Spekreijse, 1998; Spillmann & Werner, 1996). Yet, most of these studies have used synthetic rather than natural images to investigate the process of contextual interactions.

However, it is important to validate the effects seen with the synthetic stimuli using naturalistic stimuli to see if these results can be extended to the processing of natural scenes. Though some studies appear to validate the effects seen with synthetic stimuli in naturalistic stimuli (Ringach, Hawken, & Shapley, 2002; Smyth, Willmore, Baker, Thompson, & Tolhurst, 2003; Touryan, Felsen, & Dan, 2005), others point out that naturalistic stimuli are required to

`

adequately understand brain responses to natural visual scenes (Braun, 2003; David, Vinje, & Gallant, 2004; Felsen & Dan, 2005; Hansen, Essock, Zheng, & DeFord, 2003; Kayser, Körding, & König, 2004; Simoncelli, 2003). For example, natural images have higher order statistics that elicit complex non-linear neural responses that are not typically found in synthetic stimuli (David et al., 2004; Gilbert & Wiesel, 1990). Specifically, the higher order structure that is particular to natural images is determined by the phases of the different frequency components, and it is suggested that the relative phases influence the neural responses seen with natural images (Adelson & Bergen, 1985; Felsen, Touryan, Han, & Dan, 2005; Kayser, Salazar, & Konig, 2003; Mechler, Victor, Purpura, & Shapley, 1998; Weliky, Fiser, Hunt, & Wagner, 2003). One of the studies showed that the enhanced feature sensitivity of neurons was due to the phase spectra of natural images (Felsen et al., 2005). Hence, we assert it is critical to evaluate neural properties using naturalistic images.

Here we investigate whether these extra-classical interactions occur in response to natural images in visual field maps V1 to V3. We hypothesize that the contextual interactions that will take place while viewing the natural images will not be found for the phase scrambled images. To remove the higher order statistical regularities responsible for eliciting a contextual interaction from the natural images, we scrambled the phases of the different frequency components of the images. Using functional magnetic resonance imaging (fMRI), we can measure the responses from millions of neurons to a visual stimulus in humans. Computational models can link these responses to stimuli and characterize the aggregate receptive field properties of a population of neurons. The aggregate receptive field for such a neuronal population is called its population receptive field (pRF) and the computational model that estimates the pRFs, is referred to as the pRF model (Dumoulin & Wandell, 2008; K. N. Kay et al., 2013; Zuiderbaan et al., 2012). The most basic pRF model summarizes the pRF properties by their position (x, y) and size (σ_{pRF}). Here we investigate whether pRF sizes change by viewing natural images compared to the phase scrambled natural images. We see these changes in pRF size as a measure of the presence of extra classical interactions. In a previous study, contextual interactions of contour integration were observed as pRF size changes in V2 and V3 but not in V1 and later visual field maps (Dumoulin et al., 2014). Consequently, we hypothesize that the presence of contextual integration mechanisms will cause the pRF size estimates to increase for natural images in early visual field maps V2 and V3.

`

Methods

Subjects

10 subjects (6 females, age range 26 – 46, (M = 30.4 years, SD = 6.13 years)) participated in this study. All subjects had normal or corrected-to-normal visual acuity. All studies were performed with the informed written consent of the subjects. Studies were approved by the Human Ethics Committee of the University Medical Center Utrecht in accordance with the World Medical Association's Declaration of Helsinki.

Stimuli

Stimuli consisted of a stimulus carrier (as shown in figure 1) revealed through a bar aperture that swept across the visual field in discrete steps in 8 different bar configurations for a given scan (4 different orientations (0, 45, 90, 135) with two step directions for each orientation).

The width of the bar aperture subtended 1/4th of the stimulus radius (1.5 and 5 degrees of visual angle, respectively). Each bar position lasted for a duration of 30s and the mean luminance block for 30 s. Total duration of one scan run was 6 minutes. 3 to 4 runs each of natural and phase scrambled natural condition was run per subject during one scan session. Subjects performed a fixation dot task, in which the central fixation dot changed color and subjects were asked to report the change using a button press. Accuracy of the fixation dot was recorded as percentage of correct responses out of the total number of changes. Due to the malfunctioning of the response box in the scanner, performance accuracy could not be measured for all the runs for one of the subjects and for 2 out of 5 runs for another subject. All other subjects had an accuracy of over 90% correct in the fixation dot task.

All stimuli were shown on a MR compatible 32-inch BOLD screen from Cambridge systems (32 inches, 1920 x 1080 pixels, refresh rate of 120 Hz) using PsychToolbox (Brainard, 1997; Pelli, 1997) at 210 cm from the subjects' eyes. Subjects viewed the stimuli reflected through a mirror attached to the coil of the scanner.

Stimulus carriers

We used two types of carrier stimulus images. The first type was a set of natural images including images of landscapes, buildings, animals, faces taken from the 'Berkeley Segmentation Dataset and Benchmark' (Martin, Fowlkes, Tal, & Malik, 2001). The second type was made from the same natural images, but with their phase values assigned in a random order, resulting in a noise pattern as shown in figure 1A. Different stimulus carriers can excite

`

different population of neurons and influence the pRF size estimate from the pRF model as described below.

The size (σ_{pRF}) estimate from the pRF model depends on both neuronal and non-neuronal factors (Dumoulin & Wandell, 2008; A. T. Smith et al., 2001) and their contribution to total size σ_{pRF} can be given by:

$$\sigma_{pRF}^2 = \sigma_{nRF}^2 + \sigma_{pv}^2 + k, \qquad (Equation\ 1)$$

Where, neuronal factors are represented by both σ_{nRF} (mean neuronal RF size) and σ_{pv} (position variance of neuronal RF) and the non-neuronal factors by k. At the spatial resolution of fMRI, pRF models can capture both the classical and extra classical RF for a population of neurons (Dumoulin et al., 2014). Thus, σ_{nRF} can be divided into a classical (σ_{cRF}) and an extra-classical RF (σ_{ecRF}):

$$\sigma_{nRF}^2 = \sigma_{cRF}^2 + \sigma_{ecRF}^2 \qquad (Equation\ 2)$$

The difference in the population receptive field (σ_{pRF}) between natural (n) and phase scrambled natural (s) images for an individual population of neurons is given by:

$$\sigma_{pRF(n-s)}^2 = \sigma_{pRF(n)}^2 - \sigma_{pRF\ (s)}^2 \qquad (Equation\ 3)$$

Given that the experimental conditions and stimulus aperture are constant between the conditions and the same recording sites are compared, we assume that the position variance and non-neuronal factors (σ_{pv} and k, in formula 1) are the same for both conditions and cancel out. Thus, combining equations 1, 2 and 3,

$$\sigma_{pRF(n-s)}^2 = \sigma_{nRF(n-s)}^2$$

$$= \sigma_{cRF(n-s)}^2 + \sigma_{ecRF\ (n-s)}^2 \qquad (Equation\ 4)$$

`

We expect that any difference in the pRF size is due to the difference of intercellular long-range interactions occurring when viewing natural images, but not when viewing the phase scrambled images, since phase scrambling removes the contextual information from the images. Thus, the expected increase in pRF size for natural images will be driven by extra classical RF interactions:

$$\sigma^2_{pRF(n-s)} = \sigma^2_{ecRF\ (n-s)} \qquad (Equation\ 5)$$

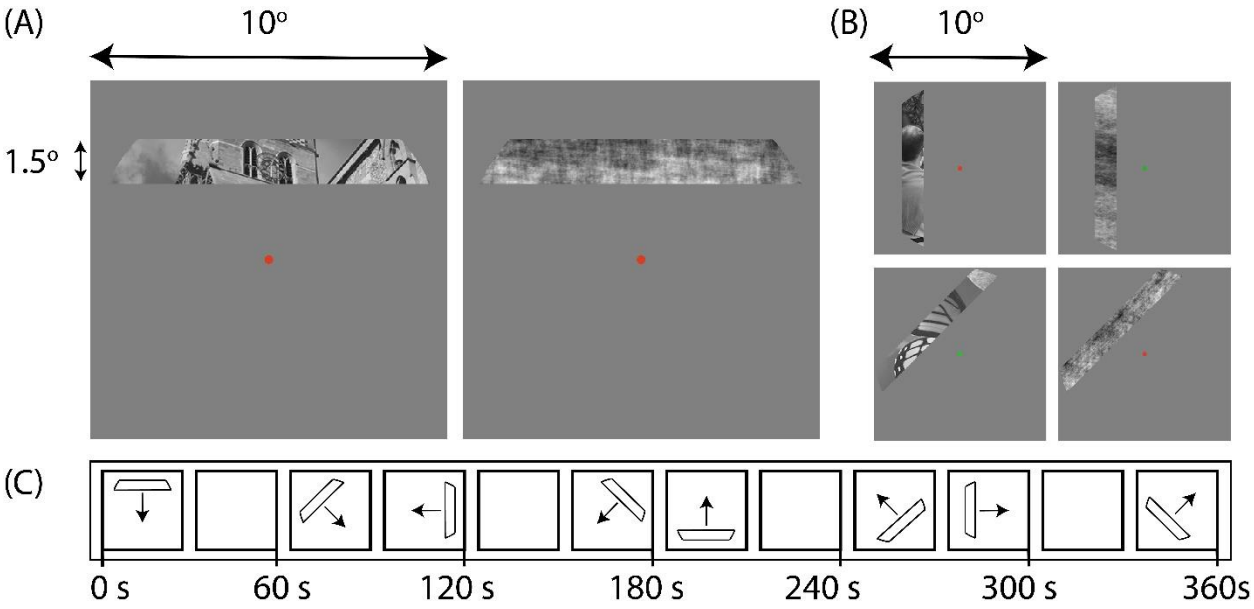

Figure 1. Example stimuli. (A) pRF mapping stimuli consisted of bar apertures revealing the carriers, which consisted of either a natural image (left) or a phase scrambled natural image (right). A fixation dot was presented in the center which changed color between red and green. The stimulus was presented within a circular window, with a radius of 5 degrees of visual angle. (B) Two pairs of stimulus carrier examples for both conditions. The carrier image changed twice within a volume acquisition (TR) (C) Schematic representation of the bar positions over time (in seconds). The bar aperture swept through the visual field in 30 s (20 TRs) in 8 directions with a mean luminance blank period (0% contrast) of 30 s after every cardinal direction for the fMRI signal to return to the baseline.

MRI acquisition

Anatomical scans were acquired using a 3D T1-weighted MP2RAGE sequence (TR - 6.2 ms, TE - 3 ms, flip angle - 5 degrees, FOV - 220 x 220 x 164 mm, voxel size - 0.6x0.6x0.6 mm). Functional T2* weighted 2- dimensional EPI scans (2D-EPI, TR – 1.5s, TE -25 ms, Flip angle -

`

70 degrees, FOV – 180 x 180 x 50 mm, voxel size 1.8 mm isotropic, 28 slices) were acquired using a Philips 7T scanner. Each subject completed 6-8 functional runs in each session with equal number of runs for the natural and phase scrambled natural condition.

Processing of anatomical and functional data

Anatomical scans were segmented into gray and white matter using an automatic segmentation pipeline using TOADS/CRUISE algorithm in MIPAV (Bazin & Pham, 2007) and hand corrected to minimize segmentation errors (https://www.slicer.org/).

Functional data was preprocessed using AFNI (Cox, 1996) and the Matlab based vistasoft toolbox (http://white.stanford.edu/software). Raw data were motion corrected using the AFNI command 3dvolreg. Between scans motion correction was performed by aligning the first functional volume of each scan with every other scan. Within scans motion correction was done by aligning all the frames to the first frame. We applied the same motion correction for all the runs from both the natural and phase scrambled natural conditions and averaged all the runs from both conditions together and each condition separately, resulting in 3 averaged functional data sets. Averaged functional scans were then coregistered on the T1 weighted anatomy. The center of mass of the functional image was aligned with the center of mass of the occipital lobe of the anatomy (obtained by clipping in the anterior posterior direction), providing a good starting point to perform an affine transformation using the AFNI function, 3dAllineate, using a two-pass approach. This step performs a set of coarse alignments, allowing for large rotations and shifts and uses the best alignments for a fine transformation stage. Next, another stage of affine transformation was performed with a one pass option without blurring, allowing only small rotations and shifts. Results of the coregistration was assessed manually by visual inspection using various anatomical markers such as the boundaries for gray matter/ white matter and gray matter/ cerebrospinal fluid. Functional scans from all runs and runs from each of the conditions (natural image and phase scrambled natural image) separately were averaged and interpolated to the anatomical segmentation. The pRF-model (Dumoulin & Wandell, 2008) was then run on the resulting functional scans using the vistasoft toolbox.

pRF analysis

We estimated the pRF properties (position and size) for every cortical location using the PRF model (Dumoulin & Wandell, 2008). Briefly, a population receptive field for every cortical location is modeled as a 2-dimensional gaussian with parameters for its position (x, y) and size (sigma). A predicted time course for every stimulus position is made combining the stimulus,

`

model and the hemodynamic response function (HRF). The predicted time series is then compared to the measured fMRI time series and the model parameters that give the least residual sum of squares is used as the pRF properties for that cortical location. We used the pRF-model with a fitted HRF (hemodynamic response function) to determine the pRFs.

Specifically, for this study we computed the pRF parameters for each cortical location using the averaged functional data from all the runs (including both natural and phase scrambled natural conditions). After estimating the pRF parameters using a standard canonical HRF (Boynton et al., 1996; Friston et al., 1998), we ran an HRF fit over the cortical locations where the pRF model explained more than 10% of variance in the previous step, keeping all the pRF parameters constant (Harvey & Dumoulin, 2011). pRF parameters were then adjusted using the estimated HRF. We converted the resulting pRF parameters (x, y, sigma) to the traditional eccentricity and polar angle maps. We then delineated four visual areas (V1, V2, V3, LO1+LO2) using these maps (Wandell et al., 2007).

pRF size parameters (sigma) for the individual conditions were refined using an optimization algorithm (Fletcher & Powell, 1963) while keeping the position (x, y) and the HRF constant. We then computed the pRF size difference between the two conditions. For this, we determined a linear function that described the relation between pRF size and eccentricity for each visual area. We then computed the relative difference in pRF size at a central eccentricity (2.5 degrees of visual angle) between the two conditions as shown in equation 6.

$$y = \frac{x1 - x2}{\frac{(x1 + x2)}{2}} \qquad (Equation\ 6)$$

Where, y is the relative difference in pRF size, $x1$ is the central pRF size for the natural condition, $x2$ is the central pRF size for the phase scrambled condition. The relative difference is calculated to account for the increase in pRF size over the visual hierarchy. Resulting values were then averaged across 10 subjects per visual region. We performed a one-way repeated measures ANOVA to determine whether the differences were significant for individual visual field maps and across visual field maps.

`

Results

Population receptive field size increases with eccentricity in all visual areas:

Figure 2a shows two example BOLD fMRI responses for a single recording site from V3 elicited by viewing a moving bar aperture carrying natural images and phase scrambled natural images respectively. Predicted responses to the corresponding stimuli shows that the model explains up to 90% of the variance in the measured data in both conditions. We observe a systematic increase in the pRF size value with eccentricity for V1, V2 and V3 and an increase in pRF size value with visual hierarchy as expected from previous studies (Amano, Wandell, & Dumoulin, 2009; Burkhalter & Van Essen, 1986; Dumoulin & Wandell, 2008; Felleman & Van Essen, 1987; Gattass, Gross, & Sandell, 1981; Harvey & Dumoulin, 2011; Newsome, Maunsell, & van Essen, 1986; Rosa, Sousa, & Gattass, 1988; Winawer, Horiguchi, Sayres, Amano, & Wandell, 2010).

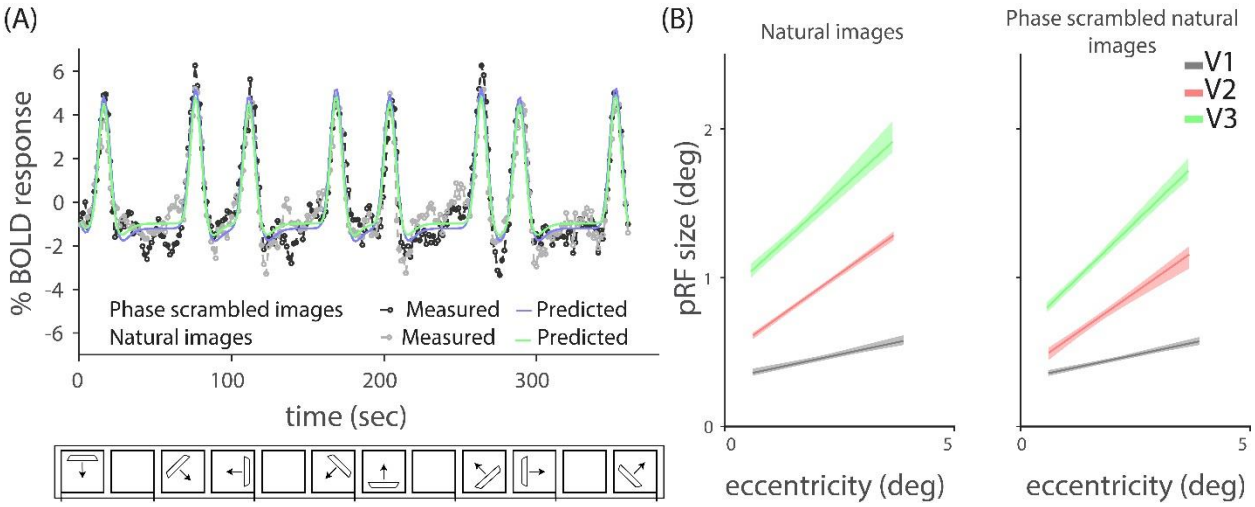

Figure 2: Example fMRI data and pRF fits from 1 subject. (A) Black and gray lines with dots indicate % BOLD fMRI responses elicited by viewing natural and phase scrambled stimuli respectively. Green and blue lines indicate their corresponding predicted responses. The fMRI time series are from one recording site from V3 and show 8 peaks corresponding to the 8 times that the bar aperture swept through the location of the pRF in the visual field, in different directions. Predicted pRF responses capture more than 90 % of variance (r^2) in the measured responses. (B) Relationship between pRF size and eccentricity in V1, V2 and V3. Left and right panel shows the natural and phase scrambled natural conditions respectively. Within each map, pRF size increases with eccentricity. The shaded error regions indicate the 95% confidence interval.

`

Larger population receptive field sizes in V1, V2 and V3 when viewing natural images

We summarized the pRF size values by taking the pRF size value at a central eccentricity from the linear fit of pRF size versus eccentricity (figure 2B). pRF sizes were generally larger for natural than for phase scrambled images (condition: $F_{(1,9)}$= 18.12, p=0.002) and this difference between conditions increased from V1 to V2 to V3 (condition x ROI: $F_{(2,18)}$= 17.64, p<0.01, condition (natural vs. phase scrambled) x ROI (V1, V2, V3) repeated measures ANOVA for 10 subjects). When tested per visual field map, the difference was significant in V1, V2 and V3 (V3: $t_{(9)}$= 4.74, p=0.001 ; V2: $t_{(9)}$= 3.65, p= 0.005; V1: $t_{(9)}$= 2.38, p= 0.0407). Illustrating that the difference increased in magnitude from V1 to V2 to V3, we found that the difference was larger in V3 than in V1 ($F_{(1,9)}$=19.78, p=0.0016) and V2 ($F_{(1,9)}$=25.92, p<0.01), and larger in V2 than in V1 ($F_{(1,9)}$=8.42, p=0.017)

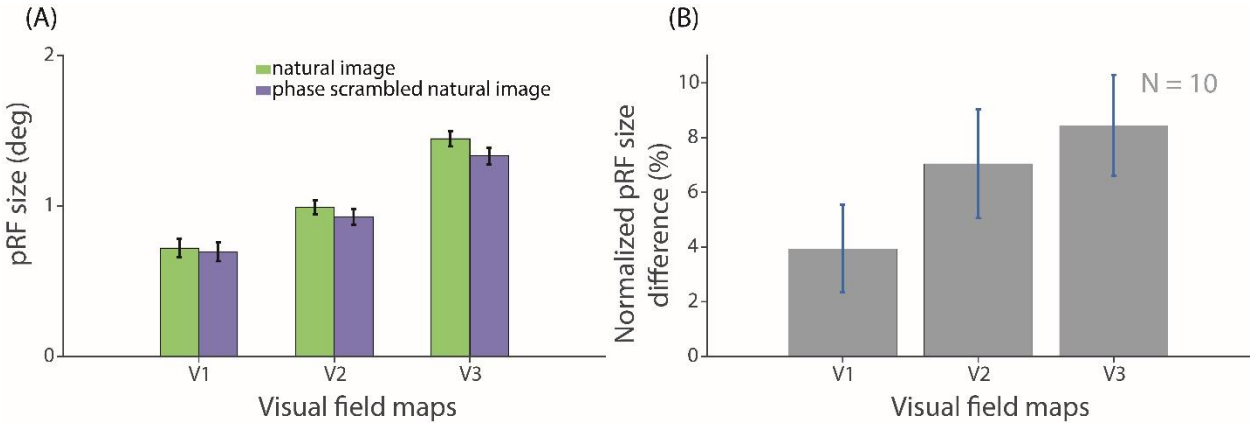

Figure 3: pRF size differences (A) Average pRF sizes for early visual field maps V1, V2 and V3 with the natural image condition in green and the phase scrambled natural image condition in blue. pRF sizes increase across the visual hierarchy. (B) Normalized pRF size difference between natural and phase scrambled conditions show that the pRF size is larger when viewing natural as compared to phase-scrambled images in all 3 visual areas. Error bars represent the standard error of the mean in both (A) and (B).

Discussion

We investigated the neural mechanisms underlying the processing of complex contextual stimuli, namely natural images. We hypothesized that the aggregate receptive field size of a population of neurons will increase when they are processing natural images compared to phase scrambled natural images due to the presence of an extra-classical intercellular

`

interactions (Field, Hayes, & Hess, 1993; Kapadia, Ito, Gilbert, & Westheimer, 1995; C.-Y. Li, 1996; Maffei & Fiorentini, 1976; Sengpiel, Sen, & Blakemore, 1997; Vinje & Gallant, 2000; Walker, Ohzawa, & Freeman, 1999). In line with our hypothesis, we found an increase in pRF sizes for visual areas V1, V2 and V3 when viewing natural images. We attribute this pRF size difference to the interaction of neurons beyond the classical receptive field required to process the complex contextual information present in natural images.

Our results are in line with the previous study by Dumoulin et al, where they found an increase in pRF size for V2 and V3 during contour integration using synthetic images (Dumoulin et al., 2014). Moreover, the percentage increase in pRF size normalized for visual areas are very similar (around 10% increase in pRF size for V3). The increase in pRF size found in our results is also in agreement with other observations from human and macaque showing an increased activation of V2 neurons in response to the statistical regularities in natural images (Freeman, Ziemba, Heeger, Simoncelli, & Movshon, 2013; Walker et al., 1999). Also, our results are consistent with previous literature showing that V2 and later areas respond to angles and curvatures, which are an integral part of naturalistic images (Anzai, Peng, & Van Essen, 2007; Hegdé & Van Essen, 2000; Ito & Komatsu, 2004; Pasupathy & Connor, 1999). Last, we show that these previous results derived from viewing synthetic images extend to more naturalistic images.

Higher visual areas such as LO1 and LO2 are typically implicated in the processing of objects (Grill-Spector, Kourtzi, & Kanwisher, 2001; Larsson & Heeger, 2006; Mazer & Gallant, 2000). Since our presented natural images contain objects, we also checked for extra-classical interactions occurring in LO1 and LO2. There are no previous reports of pRF size increase in response to a contextual stimulus. However, we did not find a significant pRF size change in these areas (supplementary figure 3). This could be due to the larger pRF sizes in these regions in combination with the limited size of the stimulus window and, consequently, an inability of the model to capture these differences. Alternatively, it's possible that integration of the higher order structures in natural images are happening at early visual areas and these are then communicated with these later areas. This could result in a signal amplitude change and not necessarily a change in pRF size (Dumoulin et al., 2014).

Apart from the average RF (classical and extra classical) size of the underlying neuronal population that was excited by the stimuli, measured pRF size changes could also be the result of other nuisance neural components which are unrelated to the response to the stimuli, such as position scatter. Position scatter of the individual neurons within the recording site are known to contribute to the overall pRF size (Dumoulin & Wandell, 2008; Hubel & Wiesel, 1974). However,

since we are comparing the same cortical locations for both natural image and control stimuli, we can be sure that the changes because of the position scatter will be cancelled out.

Alternatively, hemodynamic response properties may influence the measured pRF sizes (Dumoulin & Wandell, 2008; Klein et al., 2014). Linking neural activity to fMRI measurements should also take into account that the neural activity is indirectly measured as the hemodynamic changes. So, there can be differences in the pRF estimation depending on the hemodynamic response function (HRF) of the neuronal population. Again, since we compared the pRF sizes from the identical neuronal population for both conditions, we assume that the HRF between the two conditions do not vary.

Non-neural factors such as eye movements and head movements will also affect pRF sizes. However, we don't think that these effects influence our results. Previous studies simulating the effects of eye movements in the pRF size estimation have found that it causes an increase in the pRF sizes for all the visual field maps, which was not observed here (Klein et al., 2014; Levin et al., 2010). Moreover, almost all the subjects showed an accuracy of over 90% in the fixation dot task, indicating proper fixation. Head movement during the scan can also cause changes in the fMRI responses and hence affect the pRF model parameters. So, head motion was minimized during the scan using foam padding, and a motion correction algorithm was used to correct for any motion artifact in the data (Cox, 1996). Head motion was found to be less than one voxel size for most subjects for most runs, for which a previous study did not observe any large effects in the estimation of the pRF parameters (van Dijk et al., 2016). The presence of motion artifacts causes noisy measured responses and a reduced model prediction accuracy. However, our results showed above 90% variance explained between the model predictions and the fMRI responses. Therefore, we do not believe that eye movements or head movements can explain our results.

Natural images are rich in information content compared to the phase scrambled condition, which could cause increased attention towards the natural images. Previous studies have found that attention can modulate the responses in the attended location (Kastner et al., 1998; Murray & Wojciulik, 2004; O'Craven et al., 1999; Wojciulik et al., 1998). Attention can also have an influence in both the pRF size and position estimates (Klein et al., 2014; van Es et al., 2018). However, we don't think that the pRF size changes observed in our results are caused by an increased attention for the natural images. Firstly, attention related changes are typically observed in all the visual field maps and increase higher up the visual hierarchy (Buffalo et al., 2010; Cook & Maunsell, 2002; Klein et al., 2014; Montijn et al., 2012; O'Connor et al., 2002; Posner & Gilbert, 1999). However, we see that the pRF changes are high in V2 and V3 but not

`

in higher areas like LO1 and LO2. Second, the subjects performed an attention task in the center of the screen and all subjects performed equally good in both the conditions. Therefore, we do not believe that differences in attention are underlying our results.

Conclusion

In summary, we show the presence of an increased intercellular interaction in response to natural images in early extra-striate areas, V1, V2 and V3. We have shown that the intercellular interactions observed in synthetic stimuli translate to natural stimuli.

`

Supplementary figures

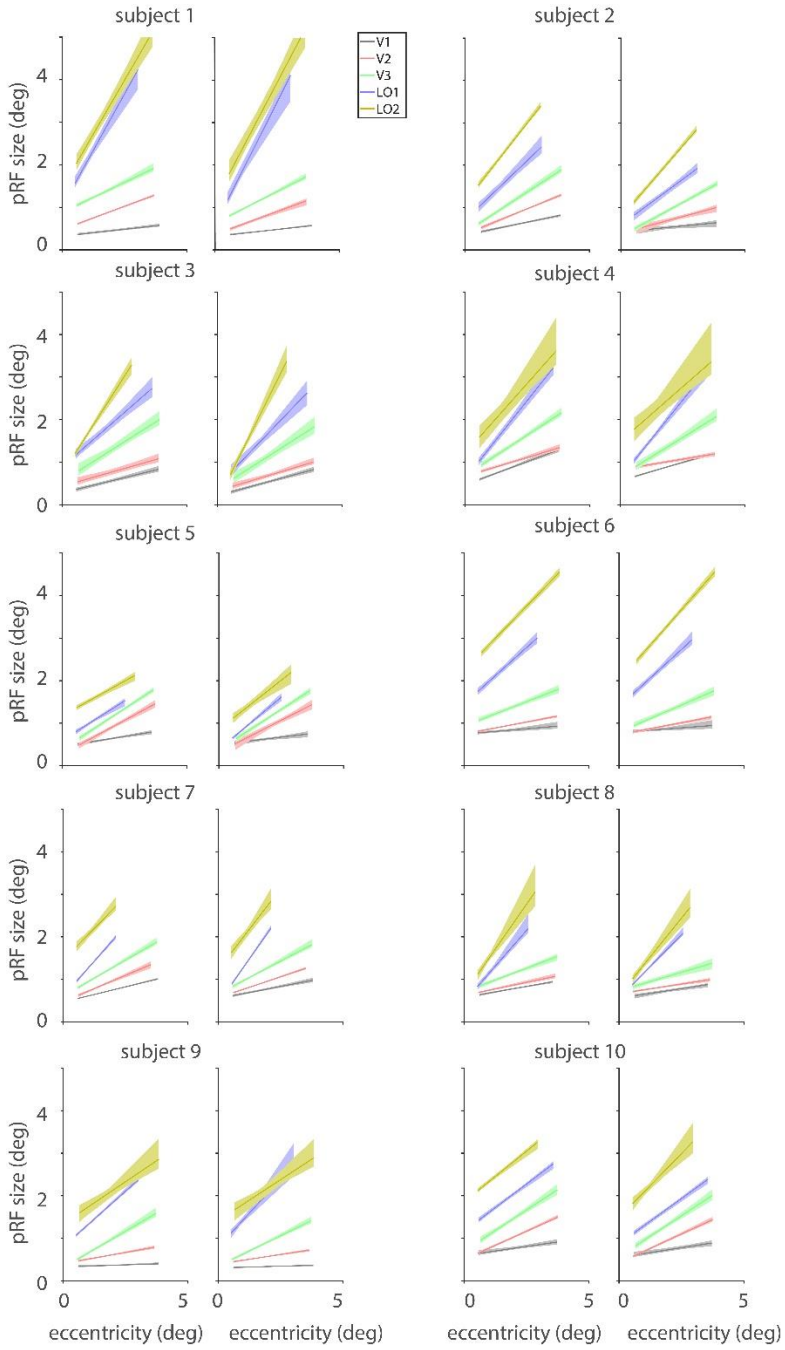

S1: pRF size vs eccentricity for 10 subjects (visual field maps V1, V2, V3, LO1, LO2). For each subject, the left panel represents the natural image condition and the right panel represents the phase scrambled natural image condition. pRF size increases with eccentricity for all visual field maps, as expected. Shaded error regions indicate the 95 % confidence interval.

`

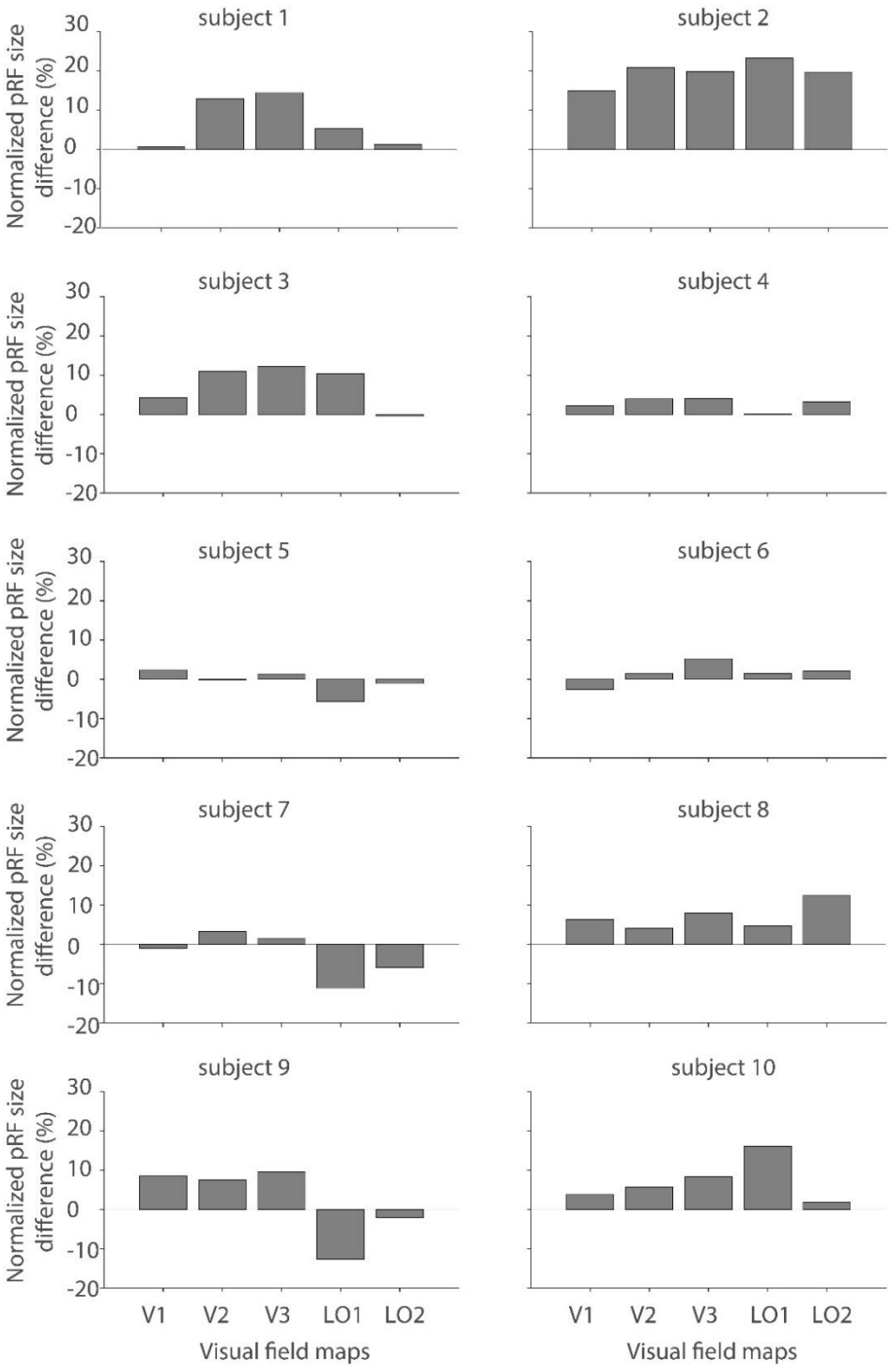

S2: Normalized pRF size difference between natural and phase scrambled conditions: All subjects show an increase in pRF size for V2 and V3 and all except subject 6 and 7 for V1. For LO1 and LO2, this difference is not consistent. Error bars represent the standard error of the mean.

`

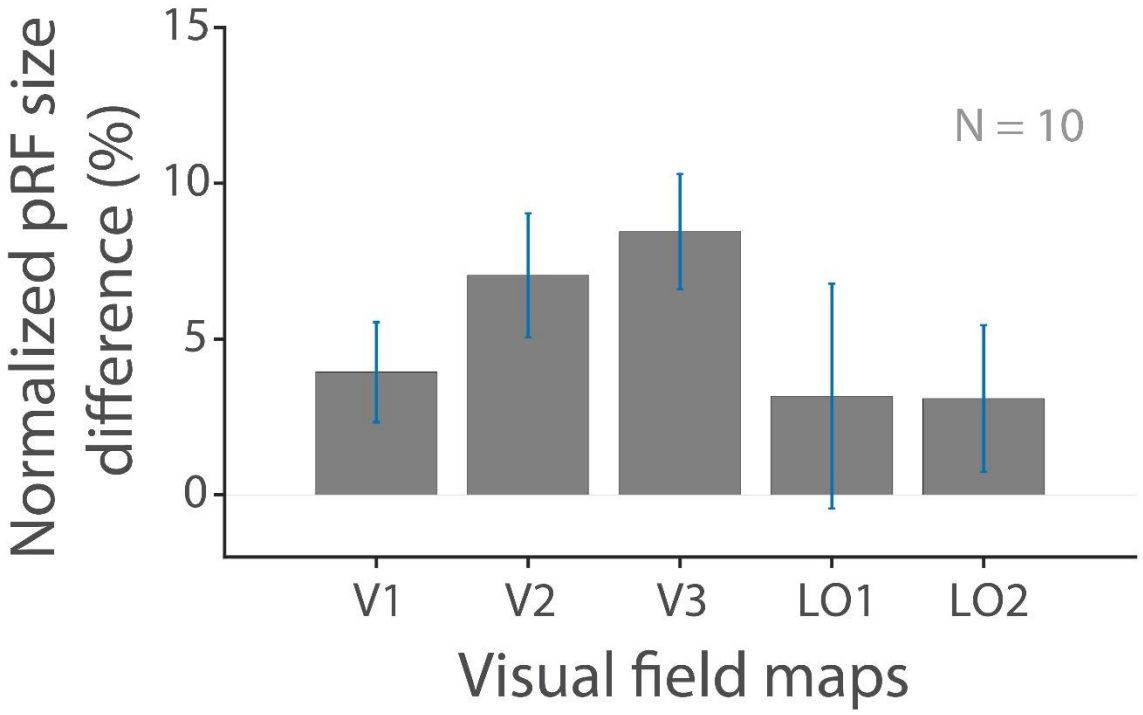

S3: Average central value difference for all visual field maps. Mean pRF size across 10 subjects with error bar showing the standard error of the mean for all visual field maps including LO1 and LO2.

`

`

Chapter 5

The functional architecture of the visual cortex in psychotic patients with visual hallucinations

Akhil Edadan, Marouska Van Ommen, Maartje C de Jong, Serge O Dumoulin, Richard Bruggeman, Teus van Laar, Frans W. Cornelissen (under preparation)

MO, TvL, RB and FWC conceived the experiments. MO, TvL, RB selected/recruited patients. MO acquired the data. AE, MO analyzed the data. AE, MO wrote the manuscript. TvL, RB, FWC, MdJ, SD provided supervision. FWC, SD acquired funding. MdJ, SD and FWC provided critical comments on the manuscript.

`

Abstract

Visual hallucinations are the second most common type of hallucinations in patients with schizophrenia after auditory hallucinations. In addition to visual hallucinations, patients with schizophrenia demonstrate abnormal visual perception in various tasks. Both abnormal visual perception and visual hallucinations are often proposed to be caused by an imbalance between the cortical excitation and inhibition. Here, we compared the functional architecture in visual cortex between patients with and without visual hallucinations and healthy control participants by analyzing population receptive field (pRF) properties. Specifically, we hypothesized that suppressive surround mechanisms are associated with visual hallucinations in patients with schizophrenia. We estimated the pRF properties using conventional moving bar stimuli, pRF modeling and functional MRI and compared pRF properties in visual field maps V1 to hV4. Our results show a reduced surround size in hV4 for patients with schizophrenia having visual hallucinations compared to patients without visual hallucinations. We speculate that this decrease in suppressive surround leading to an imbalance in excitatory and inhibitory mechanism could contribute to visual hallucinations in patients with schizophrenia.

`

Introduction

Schizophrenia is a neuropsychiatric disorder involving chronic or recurrent psychosis (American Pyschiatric Association, 2000). One of the core symptoms of schizophrenia is hallucinations. Hallucinations in the auditory domain are studied extensively in schizophrenia, but visual hallucinations are usually considered rare (Bowman & Raymond, 1931; Goodwin & Jamison, 2007; Small, Small, & Andersen, 1966; Waters et al., 2014). Thus, visual hallucination have been neglected in psychiatric and psychotic disorders though they are studied extensively in eye diseases and neurologic disorders (S. W. Anderson & Rizzo, 1994; Carter, 2015; Collerton, Perry, & McKeith, 2005; Holroyd & Wooten, 2006; Imamura et al., 1999; Matsui et al., 2006). However, recent studies have challenged the idea that visual hallucinations are atypical or uncommon in psychosis, with a lifetime prevalence rate of 37 % (van Ommen, van Laar, Cornelissen, & Bruggeman, 2019; Waters et al., 2014). Following a phenomenological study which looked at the epidemiology and clinical characteristics of visual hallucinations in psychosis (van Ommen et al., 2019), this study aims to understand its neural mechanisms. We do this by investigating whether an altered neural architecture is associated with visual hallucinations in patients with schizophrenia.

Interestingly, in addition to visual hallucinations, patients with schizophrenia show atypical performance in a range of visual perception tasks. Some of these include unusual appearance of familiar objects or scenes (Phillipson & Harris, 1985), decreased contrast sensitivity (Slaghuis, 1998), poor motion processing (Chen, Levy, Sheremata, & Holzman, 2004; Kim, Wylie, Pasternak, Butler, & Javitt, 2006), reduced orientation discriminability (Tibber et al., 2015), impaired spatial frequency processing (Slaghuis, 1998), inability to detect contours embedded in noise (Robol et al., 2013), and altered effects of prior knowledge on interpretation of visual input (Silverstein, 2016). Patients with schizophrenia are also known to show decreased susceptibility to visual illusions such as the “contrast-contrast” illusion (Dakin et al., 2005), “hollow face” illusion (Schmeider, Leweke, Sternemann, Emrich, & Weber, 1996), and binocular depth inversion illusion (Koethe et al., 2009). In short, patients with schizophrenia demonstrate a range of atypical visual perception indicative of atypical mechanisms in visual cortex.

Atypical visual perception in patients with schizophrenia are often attributed to impaired gain control mechanism, a process by which neurons control information transfer (Butler, Silverstein, & Dakin, 2008). In particular, surround suppression, a form of gain control

`

mechanism in visual processing, has been proposed to be affected in patients with schizophrenia along with deficit in a global integration (Silverstein & Keane, 2011). For example, surround suppression causes the perceived contrast to be reduced when surrounded by a high contrast in healthy individuals, but not in patients with schizophrenia (Dakin et al., 2005; Yoon et al., 2010). In line with this proposal, a recent fMRI study found reduced population receptive field (pRF) sizes in V1 and hV4 and a reduction in size and depth of the inhibitory surround in V1, V2 and hV4 in patients with schizophrenia, providing evidence for a decreased integration and surround suppression (E. J. Anderson et al., 2017). Reduced surround suppression is also found to be correlated with reduced GABA (gamma-aminobutyric acid) concentration, which is an inhibitory neurotransmitter in the brain (Yoon et al., 2010). Some computational models explain hallucinations and delusions observed in psychotic disorders to be the result of impaired excitatory-inhibitory mechanisms (Adams, Stephan, Brown, Frith, & Friston, 2013; Jardri, Thomas, Delmaire, Delion, & Pins, 2012). However, no study has investigated whether such altered functional architectures differ in patients with schizophrenia having visual hallucinations and those not having visual hallucinations.

Here we investigate the neural mechanism underlying visual hallucinations in schizophrenia by comparing the functional architecture in patients with schizophrenia with and without visual hallucinations and healthy controls. For this, we use fMRI and pRF models to quantify the properties of population of neurons in the visual cortex (Dumoulin & Knapen, 2018; Dumoulin & Wandell, 2008). We hypothesize that if visual hallucinations are associated with a disturbed integration and gain control mechanisms, pRF size and suppressive surround size will be altered in patients with schizophrenia having visual hallucinations compared to patients with schizophrenia not having visual hallucinations.

Methods

Participants

The study took place at the Neuroimaging Center at the University Medical Center Groningen from 2015 to 2018 as part of a larger study (van Ommen et al., 2019). The study was approved by the Ethical Review Board of University Medical Center, Groningen (UMCG) and is registered in the Nederland Trial Register (Dutch Trial Register), with NTR number NTR6855 (http://www.trialregister.nl/trialreg/admin/rctview.asp?TC=6855). Participants gave their written informed consent prior to the start of the study.

`

Fifteen (15) participants with schizophrenia with visual hallucinations (SZ VH group) (8 males), 16 with schizophrenia without visual hallucinations (SZ nVH) (13 males) and 17 healthy controls (HC) (12 males) participated in this study. Patients who had at least 1 visual hallucination in the previous month of the study were assigned to the SZ VH group, whereas those who never had visual hallucinations to SZ nVH group. Data from 11 participants from SZ VH, 14 from SZ nVH and 10 from HC were included in the analysis and the results shown here are from these participants (please see below for exclusion criteria). All participants were aged between 20-57 (The mean (standard deviation) age for SZ VH, SZ nVH and HC were 36.2 (7.1), 36.9 (11.1), and 31.4 (11.8) years respectively), and gave written informed consent. In addition, all patients met DSM-IV-TR criteria for schizophrenia, schizophreniform disorder, schizoaffective disorder or psychotic disorder not otherwise specified (or the DSM 5- equivalent) (American Pyschiatric Association, 2000). In case of psychiatric comorbidity, psychotic disorders had to be predominating and the visual hallucinations had to be related to the primary psychotic disorder. These were evaluated by a psychiatrist.

Patients were excluded based on the following criteria: 1) presence of psychiatric disorders other than schizophrenia spectrum disorders, neurological disorders or cognitive impairment as assessed using Mini-Mental State Examination (MMSE) < 26 (Folstein, 1975), 2) visual acuity less than 50 percent (assessed by a chart with sentences at a reading distance), 3) tested positive for visual field defects using Donders technique, 4) unable to go in the MRI scanner for clinical reasons or due to the presence of implantable devices. Furthermore, HC were excluded if they ever had a psychotic episode, experienced visual hallucinations or had a first-degree family member who have a psychotic disorder or ever had a psychotic episode.

Out of the participants who were included in the study, we further excluded participants with poor or abnormal data. Two (2) participants from SZ VH, 2 from SZ nVH and 4 from HC group were excluded due to excessive motion during the scanning session. One (1) participant from HC group was excluded due to an abnormality on the anatomical scan. Two (2) participants from SZ VH group was excluded because of visual hallucinations during the scan sessions. One from HC group was excluded because of amblyopia, known to show altered pRF properties (Clavagnier et al., 2015). Two (2) participants from HC group were excluded based on noisy pRF model fit, showing a negative slope for pRF size versus eccentricity relation or larger pRF size for V1 compared to V3 (which has never been reported in healthy adults or animal studies and therefore likely reflects poor data quality (Amano et al., 2009; Burkhalter & Van Essen, 1986; Dumoulin & Wandell, 2008; Felleman & Van Essen, 1987; Gattass et al.,

`

1981; Harvey & Dumoulin, 2011; Newsome et al., 1986; Rosa et al., 1988; Winawer et al., 2010).

Participant demographics are shown in the supplementary table 1. Participants were interviewed about their psychotic symptoms using the Dutch version of the Questionnaire for Psychotic Experiences (QPE; http://qpeinterview.com/home/) and the Positive and Negative Syndrome Scale (PANSS; (S. R. Kay, Fiszbein, & Opler, 1987)) by trained researchers. Scores on the PANSS and QPE were compared between groups using MANOVA (Wilks' lambda). We found no significant differences between the groups regarding age or gender. Non-parametric tests were used to explore differences between the groups when univariate testing was significant, using the Bonferroni correction. Most patients were diagnosed with schizophrenia (60.0%), 24.0% were diagnosed with schizoaffective disorder and 16.0% with psychotic disorder not otherwise specified. The total patient group had a significantly higher score than HC on all items on psychotic symptoms (PANSS, QPE). The biggest differences were between SZ VH and HC. SZ VH showed more psychotic symptoms on all listed PANSS and QPE items than HC (except for QPE delusions). SZ nVH did not significantly differ from HC regarding the severity of hallucinations or delusions specifically (QPE), but had more psychotic symptoms (all PANSS items) overall. Comparing the two patient groups directly, SZ VH had a significantly higher score than SZ nVH on the severity of visual hallucinations in particular and the severity of all hallucinations in general. The groups did not differ when comparing the total hallucination score minus visual hallucinations (data not shown). There were no significant differences between the patient groups regarding the severity of auditory hallucinations, severity of delusions (QPE), or total scores on negative, positive and general symptoms. All participants had a MMSE (Mini-Mental State Examination) score >25, with patients showing a worse score than HC. We compared the use of antipsychotics between the patient groups using Pearson Chi-Square test. Most patients used antipsychotics (SZ VH 72.7%, SZ nVH 92.9%). Of them, most patients used 1 atypical antipsychotic (SZ VH 50.0%, SZ nVH 69.2%). Two (2) SZ VH, 6 SZ nVH and 1 HC used antidepressants, 2 SZ VH used mood stabilizers, 3 SZ VH and 2 SZ nVH used benzodiazepines/anxiolytics. Moreover, 1 SZ nVH used Methylphenidate and 2 SZ VH used Biperiden. The quality of vision was checked during a visual evaluation session at the Ophthalmology Department at the University Medical Center Groningen (UMCG). Visual acuity (Snellen chart) and contrast sensitivity (GECKO chart) were assessed (results in supplementary table 1). There were no significant differences in visual acuity and contrast sensitivity between the groups.

`

Stimuli

All participants underwent 8 functional MRI scan runs. In the first 6 runs, they viewed bar apertures, revealing a checkerboard pattern, sweeping the visual field in discrete steps in 8 different configurations (figure 1A, 1B). Bars made a complete sweep across the visual field in 4 cardinal directions and half the visual field in 4 oblique directions. A mean luminance screen was presented at the beginning of every run and after every oblique bar pass for the hemodynamic response function (HRF) to go back to baseline. Each scan lasted for a duration of 192 seconds with each bar pass in cardinal direction for 24 seconds, oblique direction for 12 seconds and mean luminance block for 12 seconds. The fMRI data for the 12 seconds in the beginning of every run was removed from the analysis. In the last 2 functional runs, participants viewed rotating wedges with 45 degrees duty cycle. Data from these runs were not included in the analysis.

Stimuli were presented using Psychtoolbox (Brainard, 1997; Pelli, 1997) in MATLAB 7.10.0 (R2010a), on a MacBook Pro. Participants viewed the display through an angled mirror. Participants were asked to fixate on a dot in the center of the screen, and to press a button when the dot changes color. After the scan, participants were interviewed about possible hallucinations in all the sensory domains.

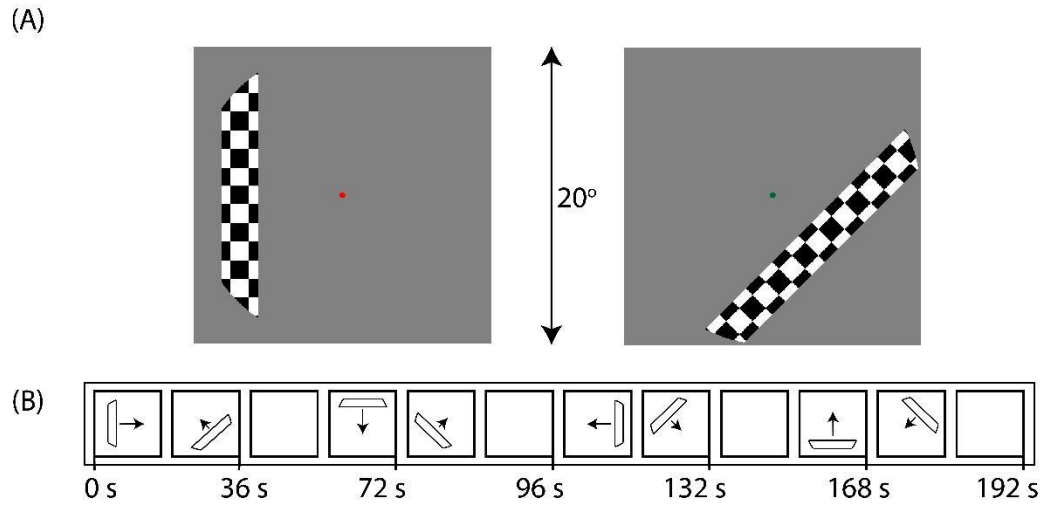

Figure 1: Illustration of the stimuli. (A) pRF mapping stimuli consisted of bar apertures revealing a high contrast moving checkerboard carrier. A fixation dot was presented in the center which changed color between red and green. Stimulus was presented within a circular window, with a radius of 10 degrees of visual angle. (B) Schematic

`

representation of bar position with the time in seconds of stimulus presentations. The bar aperture swept the visual field in 8 directions with a mean luminance blank period of 12 s after every oblique direction. Bars in the oblique directions swept only half the visual field as represented by the shorter arrows.

MRI acquisition

MRI data were collected using a 3T Philips MRI with a SENSE head coil (Intera, Philips Medical Systems, Best, The Netherlands). Participants wore noise-reducing earplugs. Foam padding was used to minimize head motion. For the functional scans, echo-planar images (EPI) were acquired, with a repetition time (TR) of 1.5 seconds, an echo time (TE) of 30 milliseconds, a voxel size of 2.5 x 2.55 x 3 mm (reconstructed voxel size = 2.5 mm isotropic) and a flip angle of 80 (FOV= 224 x 193.45 x 72 mm). Each scan consists of a maximum of 24 slices, which were aligned parallel to the calcarine sulcus. In between the functional scans, inplane T1 anatomical scans were acquired (24 slices, voxel size 2.55 x 2.5 x 3 mm, FOV 196 x 226.95 x 72 mm). Furthermore, a high-resolution T1 anatomy was acquired (160 slices, voxel size 1 x 1 x 1 mm, FOV 256 x 224 x 160 mm).

Preprocessing of the data

Raw images were converted to nifti using MRIcroGL (University of South Carolina, USA). Anatomical scans were aligned to ACPC and re-sliced into isotropic (1 mm) voxels. Then, an automatic segmentation was performed using Freesurfer (stable v5, https://surfer.nmr.mgh.harvard.edu/). Functional data was preprocessed using Freesurfer (Fischl, 2012) and Matlab based vistasoft toolbox (http://white.stanford.edu/software). All functional data from 6 pRF mapping runs were motion corrected and averaged. Averaged functional data was then coregistered onto the anatomical data and resampled to the anatomical resolution. ROIs were defined as the Visual field maps, V1, V2, V3 and hV4 delineated using a probabilistic atlas of visual areas (Benson & Winawer, 2018; Wang et al., 2014).

Population receptive field model analysis

We estimated the pRF model parameters using Matlab-based vistasoft toolbox (http://white.stanford.edu/software). We used the standard 2D gaussian model to estimate pRF

`

parameters, namely the position (x, y), spatial spread (σ) and response amplitude (β) of the pRF for every cortical location (Dumoulin & Wandell, 2008). In order to characterize the center surround property of the population of neurons, we used the difference of Gaussians (DoG) model (Zuiderbaan et al., 2012). DoG model is implemented as the combination of a central positive 2D gaussian (with position (x, y) and standard deviation (σ_1)) and a larger negative 2 D gaussian (with position (x, y) and standard deviation (σ_2)) along with their respective response amplitudes (β_1, β_2). For the further analysis, we used the width of the gaussian at half of the maximum amplitude (FWHM) for both 2 D gaussian model and DoG model. For the DoG model, we also derived the surround size (SS) as the distance between the points where the pRF reaches its minimum amplitude and suppression index (SI) as the ratio between the volumes of larger and smaller gaussians (equation 1) (Sceniak, Hawken, & Shapley, 2001; Zuiderbaan et al., 2012).

We estimated the pRF model parameters for the participants from all three groups (SZ VH, SZ nVH and HC) for the visual field maps, V1 to hV4. For the comparison between groups and visual field maps, we used six metrices – pRF size from 2 D Gaussian model, pRF size from DoG model, pRF surround, pRF surround suppression and the two components of the DoG model, positive (σ_1) and negative (σ_2) Gaussian size.

Suppression index, $SI = \frac{\beta_2 * (\sigma_2)^2}{\beta_1 * (\sigma_1)^2}$ (Equation 1)

We selected the pRF parameters from the cortical locations where the model predicted more than 30 percent of the variance in the measured response. For all those pRF parameters, we subdivided the cortical locations into 20 eccentricity bins such that there are an equal number of data points in each bin. Eccentricity bins were defined between 0.5 degrees to 9.5 degrees to avoid the pRFs close to fovea and in the far eccentricity which are at the boundaries of our stimulus display. Also, to avoid the effects of pial draining veins (Olman, Ugurbil, Schrater, & Kersten, 2004; Winawer et al., 2010), voxels with low mean fMRI signal were excluded.

For every eccentricity, we then calculated a group mean of pRF size parameters from all voxels belonging to that bin. We then fitted a linear function to the eccentricity versus mean pRF size parameter distribution. Then, we summarized the pRF size parameter as the pRF size

`

value at a central eccentricity (5 degrees) from the linear fit of pRF size parameter versus eccentricity (central value).

To test if the difference in the parameter values between the three groups were significant, we performed a one-way ANOVA on the central values from each of the six pRF parameters separately with schizophrenia and visual hallucination as the between group factors (SZ VH, SZ nVH, HC) for every visual field map individually (V1- hV4). We then compared the parameters between the SZ VH, SZ nVH and HC groups with in every visual field map if the result from the ANOVA were significant. For this we performed three separate independent t test between two groups at a time (SZ VH and SZ nVH; SZVH and HC; SZnVH and HC).

Results

Measured and predicted time series from both the patient groups and healthy controls show peaks corresponding to the instances when the bars swept the visual field (figure 2). Visual field maps for the patients and healthy controls showed the polar angle and eccentricity maps as expected, (see supplementary figure 2 for example eccentricity and polar angle maps from 1 subject in each group) (Dumoulin & Wandell, 2008; Wandell et al., 2007).

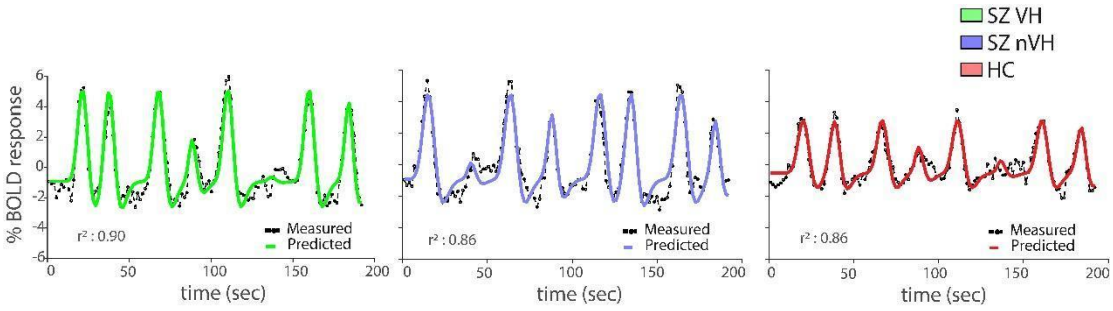

Figure 2: Example fMRI data and pRF model fit. Measured and predicted time series from one cortical location from one example subject in each of the groups. Black dotted lines in each condition represent the measured time series and the colored lines represent the predicted responses, where green is SZ VH, blue is SZ nVH and red is HC. Peaks corresponds to the instances when the stimulus bar aperture crossed the preferred region in the visual field for that cortical location.

`

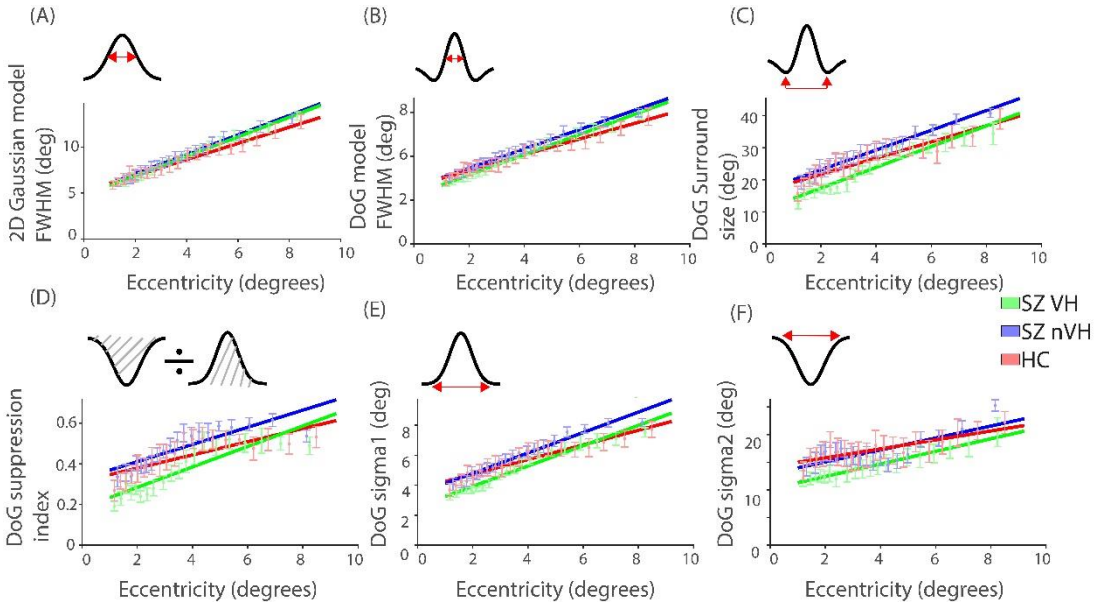

Figure 3: pRF parameters plotted against eccentricity for hV4. Lines show the linear fit for the average of the pRF parameters (pRF size (A and B), pRF surround (C), pRF surround suppression (D) and the two components of the DoG model, positive (σ_1) and negative (σ_2) Gaussian size (E and F respectively) across subjects for different groups plotted against eccentricity. Individual points are the mean pRF parameter value from each bin across all subjects from the corresponding condition and the error bars depict the standard error of mean.

Significant decrease in surround size for SZ VH compared to SZ nVH

We summarized pRF size parameters using the value at a central eccentricity from a linear fit of pRF size parameter versus eccentricity (figure 4). See figure 3 for linear fit for hv4 and supplementary figure 3,4 and 5 for V1, V2, and V3 respectively. We observed an increase in the pRF size values with visual hierarchy for pRF size from 2 D Gaussian model, pRF size from DoG model, surround size, σ_1 and σ_2. For the suppression index, we see a decrease with visual hierarchy, which is consistent with previous studies (Zuiderbaan et al., 2012).

We found an overall significant difference in hV4 between the three groups for surround size ($F_{(32,2)}$=3.97, p = 0.028), suppression index ($F_{(32,2)}$=4.79, p = 0.015) and σ_1 ($F_{(32,2)}$= 3.63, p = 0.037). We did not observe any significant difference in the pRF properties for any other visual areas (All $F_{(32,2)} < 2.21$, all $p > 0.12$). Using a post-hoc test, we found a significant decrease in

`

the surround size ($t_{(23)}$ = 3.19, p =0.004), suppression index ($t_{(23)}$ = 3.52, p =0.0018) and σ_1 ($t_{(23)}$ = 3.33, p =0.0029) for SZ VH group compared to SZ nVH group for hV4. We did not find significant differences between the patient groups and HC however (both t(23) < 1.5, both p > 0.13). We also did not find a significant difference when the two patient groups were combined and compared against the HC (all $F_{(33,1)}$ < 2.6, all p > 0.11).

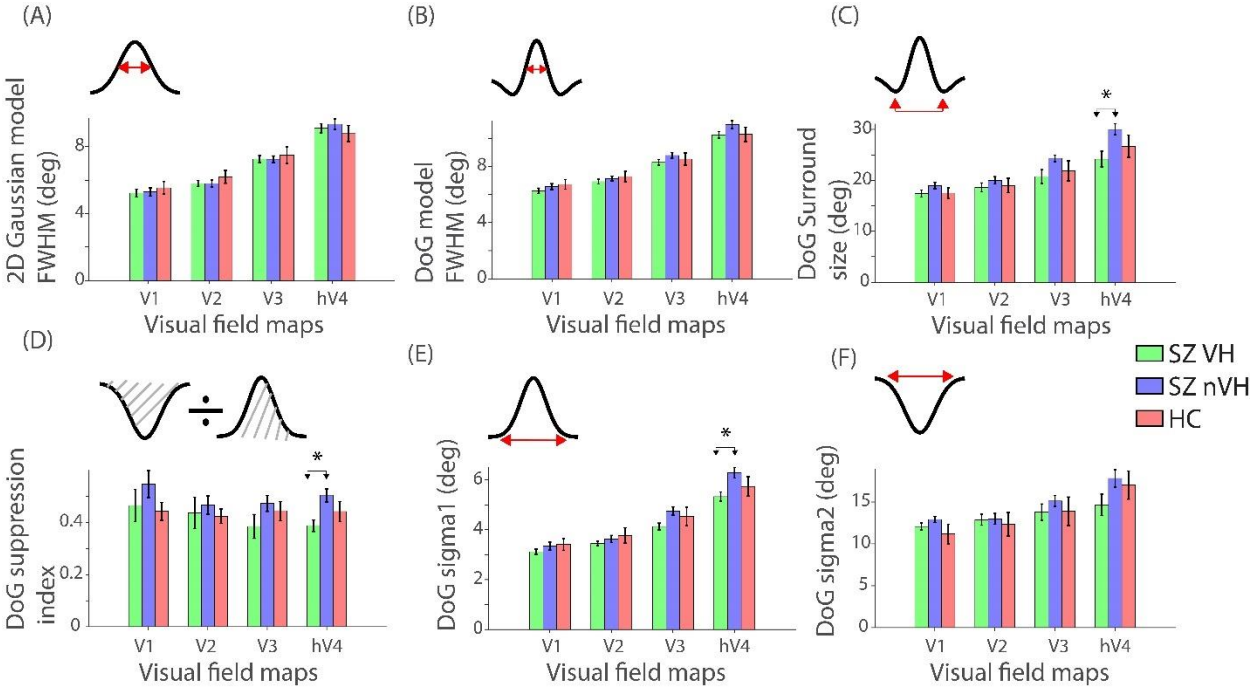

Figure 4: pRF parameter values for V1 to hV4, for pRF sizes (A and B), pRF surround size (C), pRF surround suppression (D) and the two components of the DoG model, positive (σ_1) and negative (σ_2) Gaussian size (E and F respectively). An illustration of the pRF parameter is shown in the inset. Green, blue and red bars represent SZ VH, SZ nVH and HC respectively. Significant differences between patients with and without visual hallucinations in surround size, suppression index and σ_1 values are observed in hV4. * indicates p < 0.05.

Discussion

We employed pRF models to study the changes in fine-grained functional architecture associated with visual hallucinations in patients with schizophrenia. Our results indicate a

`

decrease in the inhibitory surround size for patients with schizophrenia having visual hallucinations compared to patients with schizophrenia having no visual hallucinations in hV4.

Previous studies have proposed computational models to explain hallucinations in psychotic disorders. We explain our results using the circular inference model, which works in a Bayesian framework and relates the psychotic symptoms such as hallucinations and delusions as an imbalance between excitatory and inhibitory mechanism (Jardri & Deneve, 2013). According to the model, perception involves a combination of bottom up and top down information transfer. These information exchanges are maintained by a set of excitatory and inhibitory cortical networks, which are known to be affected in patients with schizophrenia (O'Donnell, 2011). The imbalance resulting from this disturbed information flow causes a circular propagation of beliefs, where in the sensory evidence is sent back down as if they were prior information and gets combined with themselves. A reduced suppressive surround could contribute to the weakened inhibition of the sensory information. We speculate that a reduced surround suppression leading to an imbalance between the excitatory and inhibitory mechanism could contribute to the visual hallucinations observed in people with schizophrenia.

Our results indicate that an impaired visual processing in the early visual areas predispose patients with psychotic disorder to experience visual hallucinations. Thus, our results also is in line with the 'Perception and Attention Deficit' model which describes that both impairments in visual perception and attention are a prerequisite for the occurrence of visual hallucination (Collerton et al., 2005). This model describes that in our unawareness, there are 'potentially observed objects', also called 'proto-objects'. They compete for further visual processing. Visual stimuli from the external world stimulate or activate these proto-objects. After further processing, this leads to awareness of the object. This model describes that adequate visual perception and attentional binding is necessary to choose the correct proto-object. Impairments in both perception and attention would lead to choosing the wrong proto-object, thus experiencing visual hallucination.

The severity of schizophrenia has been linked to the presence or absence of visual hallucinations (Mueser, Bellack, & Brady, 1990; Waters et al., 2014) and visual illusions (Keane, Silverstein, Wang, & Papathomas, 2013; Norton, Ongur, Stromeyer III, & Chen, 2008; Silverstein et al., 2013; Tadin et al., 2006; Yang et al., 2013), while others have found weak or no relation (Koethe et al., 2006; Tibber et al., 2015; Yang et al., 2013). We do not believe the difference in surround size that we observe is related to increased severity of the disease,

`

because the severity of disease did not differ between the two patient groups (assessed using PANSS and QPE metrics).

Inconsistent with a previous finding, our results do not support a decrease in pRF size in the early visual cortex (V1 and hV4) in patients with schizophrenia compared to the HC (E. J. Anderson et al., 2017). We separated the schizophrenia into SZ VH and SZ nVH, but it is unclear whether the patients used by Anderson and colleagues suffered from visual hallucinations. Also, 7 out of 13 subjects in their study used different medications (e.g. Clozapine, a drug widely used for treatment resistant schizophrenia) which may also affect pRF properties. Therefore, the discrepancy in findings could be related to a difference in the characteristics of the patient groups.

Anderson and colleagues found that three patients with schizophrenia were unable to maintain fixation (E. J. Anderson et al., 2017). Eye movements influence the pRF parameters and specifically can alter pRF size and position (Hummer et al., 2016; Klein et al., 2014; Levin et al., 2010) by adding a constant factor to pRF size and position for all visual field maps (Klein et al., 2014; Levin et al., 2010). However, no study specifically investigated the effect of eye-movements on the pRF surround component. Although we did not record eye-movements, we consider it unlikely that the observed difference in surround size is caused by eye movements, because we did not observe such an increase in the pRF sizes for all the visual field maps and for all the parameters.

Similarly, attention affects pRF properties, such as pRF position and size (Klein et al., 2014; van Es et al., 2018). PRF position changes due to attention increases up the visual hierarchy. Similar to the eye movements, no study has specifically looked at the changes in surround size with attention. Could differences in attention underlie our results? Previous studies have found disturbed attentional networks in patients with schizophrenia (McKay, Headlam, & Copolov, 2000; Nuechterlein et al., 2004). A recent study found a decreased performance in attention related tasks in patients with schizophrenia compared to healthy controls (Van Ommen et al., 2016). So, attention related changes may be expected between patients and healthy subjects, but we found no indication of that as attention affects the amplitude, pRF size and position across visual field maps and not just surround size in hV4.

Our study has some limitations. The first one is the small sample number of HC because of poor or abnormal data quality. This probably has led to a loss of power. Moreover, our HC group

`

shows a relatively large variability. However, our significant comparisons are between SZ VH and SZ nVH, which are not directly affected by the HC group. Second, we also used the DoG approach, however, this method is less reliable from visual field maps V3 and up (Zuiderbaan et al., 2012). We could use other models such as the Bayesian pRF model which could also give us information about the uncertainty of the model fits (Zeidman, Silson, Schwarzkopf, Baker, & Penny, 2018). Third, 3 of our participants had visual field defects, which could have influenced their perception. Nevertheless, we feel that our study contributed to the knowledge about normal visual processing in relationship with visual hallucinations in patients with a psychotic disorder. For future studies, we recommend researchers do take the presence/absence of visual hallucinations into account while investigating the visual system.

Conclusion

In summary, we provided evidence for decreased pRF surround size in patients with schizophrenia with visual hallucinations, possibly indicating a decreased inhibition of sensory information. We speculate that this may be a contributing factor to visual hallucinations in schizophrenia. Thus, hallucinations in general could be due to disruption in the balance between the excitatory and inhibitory information. This imbalance could result in a perceptual incoherence and attempts to cope with this imperfect sensory information could alter the subjective experiences in atypical ways (de Vries et al., 2013; Postmes et al., 2014).

`

Supplementary data

	Patients* (n=25)		HC (n=10)		SZ VH (n=11)		SZ nVH (n=14)		Test score pt vs HC	p-value	Test score 3 groups	p-value
	Range	M (sd)	Range	M (sd)	Range	M (sd)	Range	M (sd)	(df)		(df)	
Age (y)	21-57	36.6 (9.4)	20-49	31.4 (11.8)	27-49	36.2 (7.1)	21-57	36.9 (11.1)	85.5	.51	2.09 (2)	.35
Gender (n, (%))									0.01 (1)	1.00	1.67	.44
Males	17 (68.0)		7 (70.0)		6 (54.5)		11 (78.6)					
Females	8 (32.0)		3 (30.0)		5 (45.5)		3 (21.4)					
Education	3-8	6.6 (1.4)	7-8	7.6 (0.5)	3-8	6.2 (1.7)	4-8	6.9 (1.2)	177	.06	5.33 (2)	.07
MMSE	26-30	28.8 (1.1)	29-30	29.7 (0.5)	27-30	28.6 (1.1)	26-30	28.9 (1.1)	186	.03	6.15 (2)	.046
Visual acuity ODS	0.8-1.5	1.2 (0.2)	1-1.5	1.3 (0.2)	0.8-1.5	1.1 (0.2)	1-1.5	1.2 (0.1)	158	.24	3.31 (2)	.19
Contrast ODS	12-16	15.0 (1.2)	14-16	15.5 (0.7)	12-16	15.0 (1.4)	13-16	15.1 (1.0)	136.5	.41	0.93 (2)	.63
Diagnosis (n, (%))											1.85	.53
Schizophrenia	15 (60.0)				6 (54.5)		9 (64.3)					
Schizoaffective disorder	6 (24.0)				2 (18.2)		4 (28.6)					
Schizophreniform disorder	3 (12.0)											
Psychosis NOS	1 (4.0)				3 (27.3)		1 (7.1)					
Disease duration (y)	0-44	13.6 (11.4)			2-32	11.9 (9.2)	0-44	14.9 (13.1)			84	.73
PANSS									10.5 (3,31)	.00	6.0 (6,60)	.00
tot pos	7-28	16.4 (5.9)	7-8	7.4 (0.5)	11-28	19.3 (5.4)	7-24	14.1 (5.4)	22.6	.00	17.7	.00[BC]
tot neg	8-25	14.7 (4.3)	7-10	7.8 (1.0)	8-25	15.8 (5.2)	8-19	13.8 (3.5)	24.3	.00	13.4	.00[BC]
tot gen	20-54	34.6 (9.4)	16-20	17.8 (1.2)	23-54	39.0 (9.5)	20-47	31.2 (8.1)	31.0	.00	21.5	.00[BC]
tot	35-100	65.7 (17.8)	30-36	33.0 (1.8)	45-100	74.1 (17.8)	35-86	59.1 (15.2)	33.1	.00	23.2	.00[BC]
QPE									2.9 (4.30)	.04	13.1 (8,58)	.00
severity AH	0-28	9.2 (10.0)	0-0	0.0 (0.0)	0-23	12.6 (9.3)	0-28	6.6 (10.0)	8.4	.01	6.2	.01[B]
severity VH	0-20	5.2 (6.8)	0-0	0.0 (0.0)	3-20	11.8 (4.9)	0-0	0.0 (0.0)	5.9	.02	71.5	.00[AB]
severity all H	0-41	15.5 (14.6)	0-0	0.0 (0.0)	6-41	26.0 (11.8)	0-31	7.2 (10.9)	11.1	.00	21.2	.00[AB]
severity delusions	0-18	5.0 (5.9)	0-0	0.0 (0.0)	0-18	5.6 (6.4)	0-14	4.5 (5.6)	7.1	.01	3.6	.04
Use antipsychotics (n, (%))											1.86	.29
Yes	21 (84.0)				8 (72.7)		13 (92.9)					
No	4 (16.0)				3 (27.3)		1 (7.1)					
Type antipsychotics (n, (%))											1.94	.47
1 typical	1 (4.8)				0 (0)		1 (7.7)					
1 atypical	13 (61.9)				4 (50.0)		9 (69.2)					
Multiple	7 (33.0)				4 (50.0)		13 (23.1)					
Other medication* (n, (%))									0.64	.80	1.64	.88
Yes, 1	9 (36.0)		3 (30.0)		4 (36.4)		5 (35.7)					
No	9 (36.0)		5 (50.0)		3 (27.3)		6 (42.9)					
Multiple	7 (28.0)		2 (20.0)		4 (36.4)		3 (21.4)					

* SZ VH + SZ nVH
[A]= difference between SZ VH and SZ nVH (p<.05, corrected)
[B]= difference between SZ VH and HC (p<.05, corrected)
[c]= difference between SZ nVH and HC (p<.05, corrected)

Table S1: Demographics and illness. Demographics of the participants used for the analysis. Various scores used for assessing the patient illness are also shown.

`

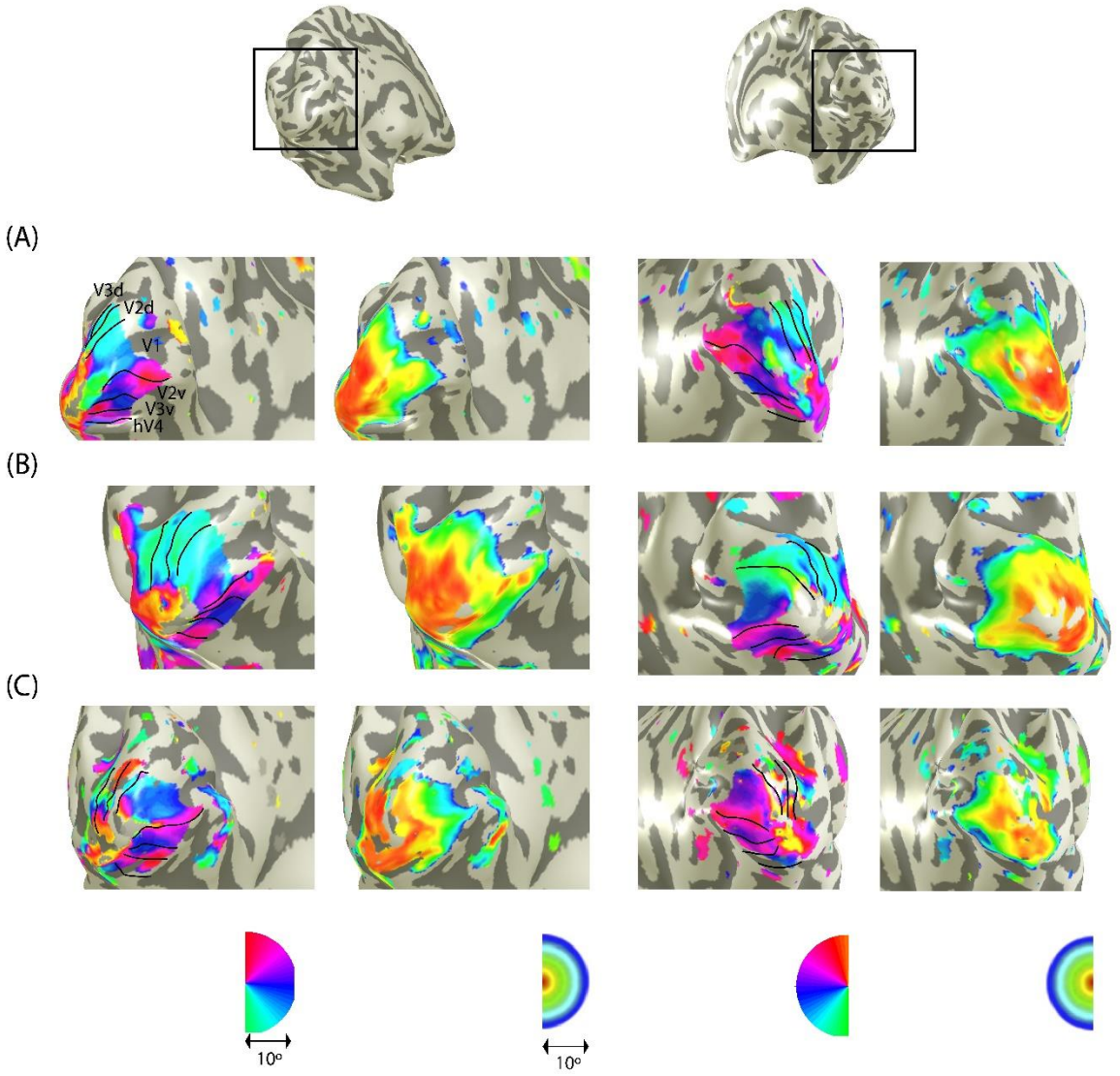

Figure S2: Visual field maps for example subjects from each group. Eccentricity and polar angle maps for subjects from (A) SZ VH (B) SZ nVH and (C) healthy group for left (columns 1 and 2) and right (columns 3 and 4) hemispheres.

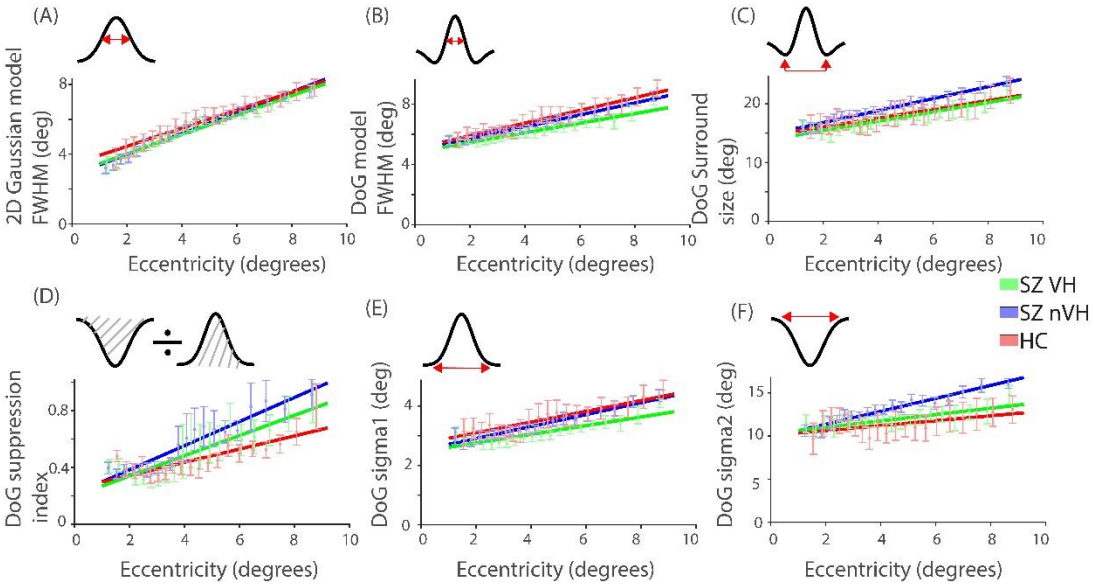

Figure S3: pRF parameters plotted against eccentricity for V1. Lines show the linear fit for the average of the pRF parameters (pRF size (A and B), pRF surround (C), pRF surround suppression (D) and the two components of the DoG model, positive (σ_1) and negative (σ_2) Gaussian size (E and F respectively) across subjects for different groups plotted against eccentricity. Individual points are the mean pRF parameter value from each bin across all subjects from the corresponding condition and the error bars depict the standard error of mean.

`

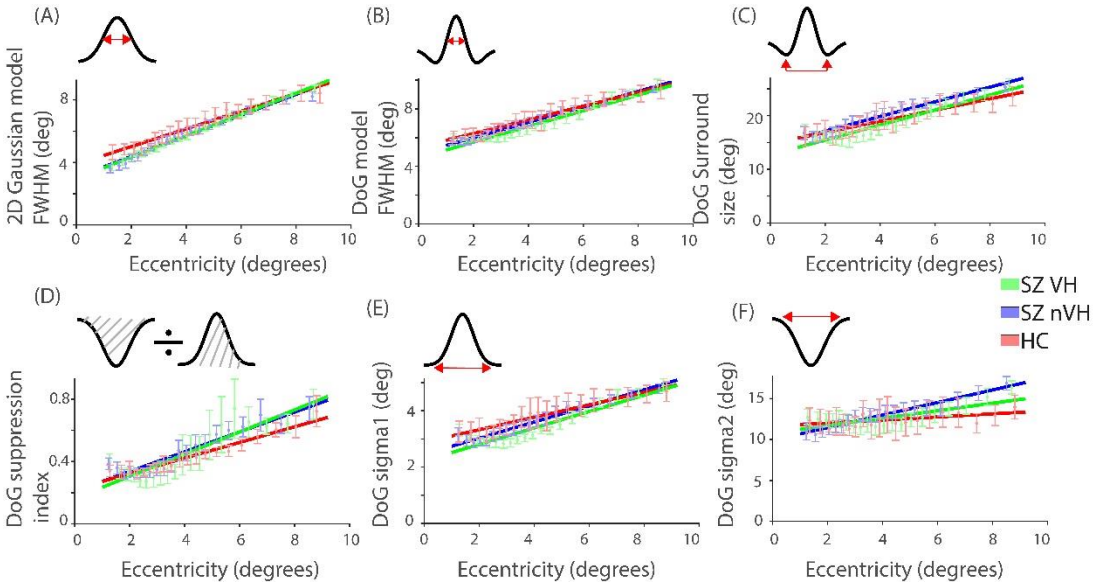

Figure S4: pRF parameters plotted against eccentricity for V2. Lines show the linear fit for the average of the pRF parameters (pRF size (A and B), pRF surround (C), pRF surround suppression (D) and the two components of the DoG model, positive (σ_1) and negative (σ_2) Gaussian size (E and F respectively) across subjects for different groups plotted against eccentricity. Individual points are the mean pRF parameter value from each bin across all subjects from the corresponding condition and the error bars depict the standard error of mean.

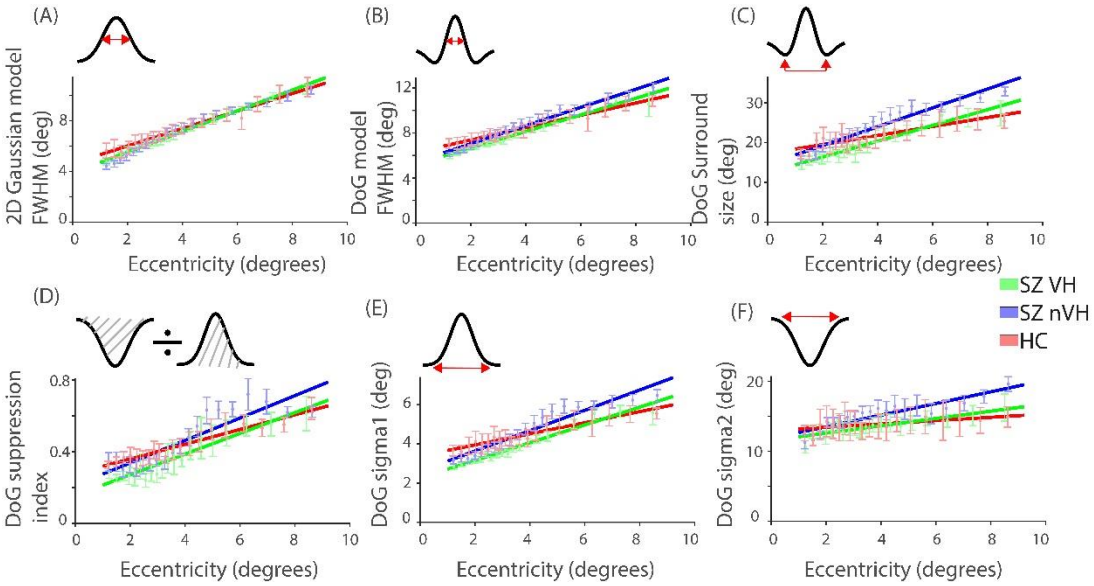

Figure S5: pRF parameters plotted against eccentricity for V3. Lines show the linear fit for the average of the pRF parameters (pRF size (A and B), pRF surround (C), pRF surround suppression (D) and the two components of the DoG model, positive (σ_1) and negative (σ_2) Gaussian size (E and F respectively) across subjects for different groups plotted against eccentricity. Individual points are the mean pRF parameter value from each bin across all subjects from the corresponding condition and the error bars depict the standard error of mean.

`

Chapter 6

General Discussion

`

The main aim of this thesis was to explore how neurons in the visual cortex process the information received from outside the classical RFs with intercellular interactions. For this, we employed the pRF modeling approach for quantifying RF properties of a population of neurons in humans measured using fMRI (Dumoulin & Wandell, 2008). pRF models are used in vision science to predict the responses of a population of neurons to visual stimulation and thereby clarify the underlying brain computations (Dumoulin & Knapen, 2018; Wandell & Winawer, 2015). In this thesis we first validated the pRF model as a true description of neural activity by using the model to predict the MEG responses to visual stimulation (chapter 2). We then investigated how extra-classical interactions operate in healthy participants. For this we used pRF models to first investigate how neurons process simple synthetic stimuli and considered the involvement of intercellular interactions in such stimulus paradigms (chapter 3). We then probed the inter-cellular interactions in depth using a more naturalistic contextual stimulus (chapter 4). Finally, we applied the pRF models to study the abnormal visual perception which are thought to be due to disturbed intercellular interactions in patients with schizophrenia (chapter 5).

This chapter discusses the importance of combining different brain measurement modalities for understanding the neural computations, and summarizes the main findings from the studies on pRF properties in healthy and patient populations. In the end we discuss new possibilities for studying spatial properties of vision at high temporal resolution.

Spatial properties of visual processing in healthy population

fMRI and MEG measures different aspects of brain activity but can be connected to a common underlying neural activity

Before we can use pRF models describing the fMRI responses to visual stimulation, for investigating abnormalities in visual processing in patients, we need to show that pRF models reflect the properties of underlying neural computations in healthy subjects (chapters 2, 3 and 4). To do this, in chapter 2, we developed a forward model that can extrapolate the predicted responses from pRF models on the cortex to MEG responses elicited by visual stimulation. MEG measures the magnetic fields resulting from the electric current instigated by neural activity (Hämäläinen et al., 1993), whereas fMRI indirectly measures the local changes in the blood oxygenation (Logothetis & Wandell, 2004). pRF models describe the computations

`

performed by the underlying neurons as measured by the fMRI. We found that the model, built to capture the properties of fMRI responses, was able to predict the MEG responses to the same stimulus. This gives confidence in a common underlying neural computation in both measurements and confirms that pRF models used in fMRI reflect neural computations. Furthermore, the ability to predict the MEG responses from pRF models opens new possibilities for studying the visual system which are discussed in the end of this chapter.

Differences in the RF properties at the neuronal and population level

Much of what we know about the RFs and the underlying computations are from the single neuron studies in non-human primates through electrophysiological measurements. Though the estimates of pRFs from the individual fMRI voxels provide a great deal of information about visual processing, these are the properties of billions of neurons and not a single neuron. Hence, it is important to make sure how much of the computations in the single neuron level are reflected in the population level. In chapter 3 we studied this by investigating whether the regularities of spatial frequency preference of individual neurons are also displayed by the neurons at the population level. We compared the pRF sizes estimated using stimuli containing sine wave gratings of different spatial frequencies. Previous single neuron animal studies have shown that the pRF sizes decrease with spatial frequency content of the stimuli (De Valois et al., 1982; Schiller et al., 1976). However, we found that the differences disappeared at the population level indicating an effect of neuronal interactions at the population level. We attributed the difference between single-neuron RF and pRF to the activation of extra-classical interactions resulting from the intercellular connections present between the neurons. We hypothesized that the inter-cellular connections are activated to counteract the decrease in the RF size for smaller spatial frequencies. Our results indicate that regularities in the properties of individual neurons may play a small role in the behavior of these neurons at the population level

Extra-classical interactions at the population level are amplified using contextual stimuli

Changes in the pRF size in the presence of extra-classical interactions was shown in previous studies using carefully controlled contextual stimuli (Dumoulin et al., 2014; Harvey & Dumoulin, 2016). In chapter 4, we used naturalistic stimuli which contained statistical regularities that are known to elicit such extra classical interactions. We estimated the pRF size for the stimuli with

`

natural images and compared it with the phase scrambled versions of the images. The phase scrambled version was chosen since they do not have the statistical regularities that can cause extra-classical interactions but contain the same amount of stimulus energy (Adelson & Bergen, 1985; Dumoulin, Dakin, & Hess, 2008; Felsen & Dan, 2005; Kayser et al., 2003; Mechler et al., 1998). We found an increase in the pRF size for stimuli with natural images compared to the phase scrambled condition in visual field maps V1, V2 and V3. We reason that this increase in the pRF size was due to the activation of extra-classical RFs in response to the contextual stimulus properties in the natural images. Our results show that pRF models are sensitive enough to pick up the subtle modulations in receptive fields due to the presence of extra-classical interactions at the population level. Our results also validate that the neural computations observed in response to carefully controlled synthetic stimuli can be extended to less controlled natural images. Natural images activate non-linear responses in a manner which is different than the synthetic grating stimuli (David et al., 2004; Dumoulin et al., 2008; Gilbert & Wiesel, 1990). Most of the studies in vision are conducted using more synthetic stimuli because it is easy to control them (Braun, 2003; Felsen & Dan, 2005; Hansen et al., 2003; Kayser et al., 2004; Ringach et al., 2002; Simoncelli, 2003; Smyth et al., 2003; Touryan et al., 2005). However, in the end such studies should be applicable to more naturalistic stimuli to get a complete understanding of visual processing in healthy and patient population.

Abnormal visual perception in patients with Schizophrenia

Reduced suppressive surround in patients with Schizophrenia with visual hallucinations

In chapter 4, we showed that the contextual interactions are processed in the early visual cortex resulting in a change in the RF size. We believe that such interactions help in the processing of local information to form a more global percept in natural images. Such an ability to process the information from the contextual stimuli are known to be disturbed in patients with schizophrenia. Various studies have attributed the abnormal performance in various cognitive and visual perception tasks in patients with schizophrenia to the inability to use context to interpret stimuli (Dakin et al., 2005; Hemsley, 2005; Silverstein & Schenkel, 1997). Specifically, the studies explained this based on a weaker suppressive surround mechanism which can both be a classical RF property and extra-classical RF property. In chapter 5, we investigated whether such reduced suppression could explain the visual hallucinations observed in these patients. We used the pRF model developed by Zuiderbaan and colleagues to investigate the pRF

`

surround size (Zuiderbaan et al., 2012). We showed evidence for a decrease in the RF surround size in patients with schizophrenia with the visual hallucinations compared to those without visual hallucinations. We believe that the decreased surround size causing an imbalance in the inhibitory mechanism could be resulting visual hallucinations in patients with schizophrenia.

Future directions for studying the temporal properties of pRFs

In this thesis we explored how different spatial properties are processed by the neurons in the visual cortex. In chapter 2 we showed that pRF method can reliably explain both fMRI and MEG recordings. In chapters 3 and 4 we showed that known regularities in receptive fields at the level of single neurons can be different from regularities at the population level, presumably due to intercellular interactions. In chapter 5, we found indications that atypical perception, in this case in patients with schizophrenia, may be related to an inability to use contextual information. However, to get a complete understanding of visual processing, we need to study the temporal properties along with the spatial properties. The forward model that we developed in the chapter 2 forms a powerful tool for studying the changes in pRF properties over time, thereby allowing us to study neural computations at a high spatial and temporal resolution. To end this chapter and this thesis, I briefly consider some of the possible future applications.

First, the contextual interactions leading to the activation of extra-classical RFs can happen at a time-scale of milliseconds which cannot be measured by fMRI. However, neural activity in the millisecond resolution can be recorded using MEG. Our forward model (chapter 2) provides the possibility to investigate the changes in the pRF size over millisecond time scale and clarify the activation of extra-classical RFs. Second, apart from the abnormal perception in the spatial domain (Phillipson & Harris, 1985; Robol et al., 2013; Slaghuis, 1998), patients with schizophrenia also show aberrant temporal processing (Chen et al., 2004; Kim et al., 2006). Our forward model (chapter 2) provides the opportunity to explore such abnormal temporal processing deficits in patients with schizophrenia by studying changes in pRF size and surround size over time. Also, our model can be used for investigating the effect of motion on the pRF parameters at the temporal resolution of MEG by extending a previous study in fMRI (Harvey & Dumoulin, 2016). Apart from the pRF properties, the forward model approach can be used for extending other models such as the attention model and numerosity model to MEG (Harvey, Klein, et al., 2013; Klein et al., 2014).

`

To summarize, in this thesis our main goal was to study how neurons in the visual cortex process information through various intercellular interactions. We explored this thoroughly in the spatial domain for healthy participants and a patient population and opened new possibilities for studying the information received in the temporal domain.

`

Appendix

References

`

Adams, R. A., Stephan, K. E., Brown, H. R., Frith, C. D., & Friston, K. J. (2013). The computational anatomy of psychosis. *Frontiers in Psychiatry*, *4*, 47.

Adelson, E. H., & Bergen, J. R. (1985). Spatiotemporal energy models for the perception of motion. *Josa A*, *2*(2), 284–299.

Allman, J., Miezin, F., & McGuinness, E. (1985). Stimulus Specific Responses from Beyond the Classical Receptive Field: Neurophysiological Mechanisms for Local-Global Comparisons in Visual Neurons. *Annual Review of Neuroscience*, *8*(1), 407–430. https://doi.org/10.1146/annurev.ne.08.030185.002203

Alvarez, I., De Haas, B. A., Clark, C. A., Rees, G., & Schwarzkopf, D. S. (2015). Comparing different stimulus configurations for population receptive field mapping in human fMRI. *Frontiers in Human Neuroscience*, *9*, 96.

Amano, K., Wandell, B. A., & Dumoulin, S. O. (2009). Visual field maps, population receptive field sizes, and visual field coverage in the human MT+ complex. *Journal of Neurophysiology*, *102*(5), 2704–2718.

American Pyschiatric, & Association. (2000). *Diagnostic criteria from dsM-iV-tr*. American Psychiatric Pub.

Anderson, E. J., Tibber, M. S., Schwarzkopf, D. S., Shergill, S. S., Fernandez-Egea, E., Rees, G., & Dakin, S. C. (2017). Visual population receptive fields in people with schizophrenia have reduced inhibitory surrounds. *Journal of Neuroscience*, *37*(6), 1546–1556.

Anderson, S. W., & Rizzo, M. (1994). Hallucinations following occipital lobe damage: the pathological activation of visual representations. *Journal of Clinical and Experimental Neuropsychology*, *16*(5), 651–663.

Andersson, J. L. R., Skare, S., & Ashburner, J. (2003). How to correct susceptibility distortions in spin-echo echo-planar images: application to diffusion tensor imaging. *Neuroimage*, *20*(2), 870–888.

Andrade, A., Kherif, F., Mangin, J., Worsley, K. J., Paradis, A., Simon, O., … Poline, J. (2001). Detection of fMRI activation using cortical surface mapping. *Human Brain Mapping*, *12*(2), 79–93.

Andrews, B. W., & Pollen, D. A. (1979). Relationship between spatial frequency selectivity and receptive field profile of simple cells. *The Journal of Physiology*, *287*(1), 163–176.

`

Angelucci, A., Levitt, J. B., & Lund, J. S. (2002). Anatomical origins of the classical receptive field and modulatory surround field of single neurons in macaque visual cortical area V1. In *Progress in brain research* (Vol. 136, pp. 373–388). Elsevier.

Anzai, A., Peng, X., & Van Essen, D. C. (2007). Neurons in monkey visual area V2 encode combinations of orientations. *Nature Neuroscience*, *10*(10), 1313.

Baillet, S., Mosher, J. C., & Leahy, R. M. (2001). Electromagnetic brain mapping. *IEEE Signal Processing Magazine*, *18*(6), 14–30.

Bazin, P.-L., & Pham, D. L. (2007). Topology-preserving tissue classification of magnetic resonance brain images. *IEEE Transactions on Medical Imaging*, *26*(4), 487–496.

Benson, N. C., & Winawer, J. (2018). Bayesian analysis of retinotopic maps. *Elife*, *7*, e40224.

Bowman, K. M., & Raymond, A. F. (1931). A statistical study of delusions in the manic-depressive psychoses. *American Journal of Psychiatry*, *88*(1), 111–121.

Boynton, G. M., Engel, S. A., Glover, G. H., & Heeger, D. J. (1996). Linear systems analysis of functional magnetic resonance imaging in human V1. *Journal of Neuroscience*, *16*(13), 4207–4221.

Brainard, D. H. (1997). The psychophysics toolbox. *Spatial Vision*, *10*, 433–436.

Braun, J. (2003). Natural scenes upset the visual applecart. *Trends in Cognitive Sciences*, *7*(1), 7–9.

Brewer, A. A., & Barton, B. (2012). Visual field map organization in human visual cortex. *Visual Cortex-Current Status and Perspectives*, 29–60.

Brookes, M. J., Zumer, J. M., Stevenson, C. M., Hale, J. R., Barnes, G. R., Vrba, J., & Morris, P. G. (2010). Investigating spatial specificity and data averaging in MEG. *Neuroimage*, *49*(1), 525–538.

Buffalo, E. A., Fries, P., Landman, R., Liang, H., & Desimone, R. (2010). A backward progression of attentional effects in the ventral stream. *Proceedings of the National Academy of Sciences*, *107*(1), 361–365.

Burkhalter, A., & Van Essen, D. C. (1986). Processing of color, form and disparity information in visual areas VP and V2 of ventral extrastriate cortex in the macaque monkey. *Journal of Neuroscience*, *6*(8), 2327–2351.

`

Butler, P. D., Silverstein, S. M., & Dakin, S. C. (2008). Visual perception and its impairment in schizophrenia. *Biological Psychiatry*, *64*(1), 40–47.

Campbell, F. W., & Robson, J. G. (1968). Application of Fourier analysis to the visibility of gratings. *The Journal of Physiology*, *197*(3), 551.

Carter, R. (2015). On visual hallucinations and cortical networks: a trans-diagnostic review. *Journal of Neurology*, *262*(7), 1780–1790.

Cavanaugh, J. R., Bair, W., & Movshon, J. A. (2002). Nature and interaction of signals from the receptive field center and surround in macaque V1 neurons. *Journal of Neurophysiology*, *88*(5), 2530–2546.

Chen, Y., Levy, D. L., Sheremata, S., & Holzman, P. S. (2004). Compromised late-stage motion processing in schizophrenia. *Biological Psychiatry*, *55*(8), 834–841.

Clavagnier, S., Dumoulin, S. O., & Hess, R. F. (2015). Is the cortical deficit in amblyopia due to reduced cortical magnification, loss of neural resolution, or neural disorganization? *Journal of Neuroscience*, *35*(44), 14740–14755.

Collerton, D., Perry, E., & McKeith, I. (2005). Why people see things that are not there: a novel perception and attention deficit model for recurrent complex visual hallucinations. *Behavioral and Brain Sciences*, *28*(6), 737–757.

Cook, E. P., & Maunsell, J. H. R. (2002). Attentional modulation of behavioral performance and neuronal responses in middle temporal and ventral intraparietal areas of macaque monkey. *Journal of Neuroscience*, *22*(5), 1994–2004.

Cox, R. W. (1996). AFNI: software for analysis and visualization of functional magnetic resonance neuroimages. *Computers and Biomedical Research*, *29*(3), 162–173.

da Silva, F. L. (2013). EEG and MEG: relevance to neuroscience. *Neuron*, *80*(5), 1112–1128.

Dakin, S., Carlin, P., & Hemsley, D. (2005). Weak suppression of visual context in chronic schizophrenia. *Current Biology*, *15*(20), R822–R824.

Dale, A. M., Fischl, B., & Sereno, M. I. (1999). Cortical surface-based analysis: I. Segmentation and surface reconstruction. *Neuroimage*, *9*(2), 179–194.

David, S. V, Vinje, W. E., & Gallant, J. L. (2004). Natural stimulus statistics alter the receptive field structure of v1 neurons. *Journal of Neuroscience*, *24*(31), 6991–7006.

`

De Valois, R. L., Albrecht, D. G., & Thorell, L. G. (1982). Spatial frequency selectivity of cells in macaque visual cortex. *Vision Research*, *22*(5), 545–559.

de Vries, R., Heering, H. D., Postmes, L., Goedhart, S., Sno, H. N., & de Haan, L. (2013). Self-disturbance in schizophrenia: a phenomenological approach to better understand our patients. *The Primary Care Companion for CNS Disorders*, *15*(1).

Dow, B. M., Snyder, A. Z., Vautin, R. G., & Bauer, R. (1981). Magnification factor and receptive field size in foveal striate cortex of the monkey. *Experimental Brain Research*, *44*(2), 213–228.

Dumoulin, S. O., Dakin, S. C., & Hess, R. F. (2008). Sparsely distributed contours dominate extra-striate responses to complex scenes. *Neuroimage*, *42*(2), 890–901.

Dumoulin, S. O., Hess, R. F., May, K. A., Harvey, B. M., Rokers, B., & Barendregt, M. (2014). Contour extracting networks in early extrastriate cortex. *Journal of Vision*, *14*(5), 18.

Dumoulin, S. O., & Knapen, T. (2018). How visual cortical organization is altered by ophthalmologic and neurologic disorders. *Annual Review of Vision Science*, *4*, 357–379.

Dumoulin, S. O., & Wandell, B. A. (2008). Population receptive field estimates in human visual cortex. *Neuroimage*, *39*(2), 647–660.

Engel, S. A., Glover, G. H., & Wandell, B. A. (1997). Retinotopic organization in human visual cortex and the spatial precision of functional MRI. *Cerebral Cortex (New York, NY: 1991)*, *7*(2), 181–192.

Enroth-Cugell, C., & Robson, J. G. (1966). The contrast sensitivity of retinal ganglion cells of the cat. *The Journal of Physiology*, *187*(3), 517–552.

Felleman, D. J., & Van Essen, D. C. (1987). Receptive field properties of neurons in area V3 of macaque monkey extrastriate cortex. *Journal of Neurophysiology*, *57*(4), 889–920.

Felsen, G., & Dan, Y. (2005). A natural approach to studying vision. *Nature Neuroscience*, *8*(12), 1643.

Felsen, G., Touryan, J., Han, F., & Dan, Y. (2005). Cortical sensitivity to visual features in natural scenes. *PLoS Biology*, *3*(10), e342.

Field, D. J., Hayes, A., & Hess, R. F. (1993). Contour integration by the human visual system: evidence for a local “association field.” *Vision Research*, *33*(2), 173–193.

`

Fischl, B. (2012). FreeSurfer. *Neuroimage*, *62*(2), 774–781.

Fischl, B., & Dale, A. M. (2000). Measuring the thickness of the human cerebral cortex from magnetic resonance images. *Proceedings of the National Academy of Sciences*, *97*(20), 11050–11055.

Fischl, B., Liu, A., & Dale, A. M. (2001). Automated manifold surgery: constructing geometrically accurate and topologically correct models of the human cerebral cortex. *IEEE Transactions on Medical Imaging*, *20*(1), 70–80.

Fischl, B., Sereno, M. I., & Dale, A. M. (1999). Cortical surface-based analysis: II: inflation, flattening, and a surface-based coordinate system. *Neuroimage*, *9*(2), 195–207.

Fitzpatrick, D. (2000). Seeing beyond the receptive field in primary visual cortex. *Current Opinion in Neurobiology*, *10*(4), 438–443.

Fletcher, R., & Powell, M. J. D. (1963). A rapidly convergent descent method for minimization. *The Computer Journal*, *6*(2), 163–168.

Folstein, M. E. (1975). A practical method for grading the cognitive state of patients for the children. *J Psychiatr Res*, *12*, 189–198.

Freeman, J., Ziemba, C. M., Heeger, D. J., Simoncelli, E. P., & Movshon, J. A. (2013). A functional and perceptual signature of the second visual area in primates. *Nature Neuroscience*, *16*(7), 974.

Friston, K. J., Fletcher, P., Josephs, O., Holmes, A., Rugg, M. D., & Turner, R. (1998). Event-related fMRI: characterizing differential responses. *Neuroimage*, *7*(1), 30–40.

Gattass, R., Gross, C. G., & Sandell, J. H. (1981). Visual topography of V2 in the macaque. *Journal of Comparative Neurology*, *201*(4), 519–539.

Gilbert, C. D., & Wiesel, T. N. (1990). The influence of contextual stimuli on the orientation selectivity of cells in primary visual cortex of the cat. *Vision Research*, *30*(11), 1689–1701.

Goodwin, F. K., & Jamison, K. R. (2007). *Manic-depressive illness: bipolar disorders and recurrent depression* (Vol. 1). Oxford University Press.

Gorgolewski, K. J., Auer, T., Calhoun, V. D., Craddock, R. C., Das, S., Duff, E. P., … Halchenko, Y. O. (2016). The brain imaging data structure, a format for organizing and describing outputs of neuroimaging experiments. *Scientific Data*, *3*, 160044.

`

Grill-Spector, K., Kourtzi, Z., & Kanwisher, N. (2001). The lateral occipital complex and its role in object recognition. *Vision Research*, *41*(10–11), 1409–1422.

Grossberg, S., & Mingolla, E. (1985). Neural dynamics of form perception: boundary completion, illusory figures, and neon color spreading. *Psychological Review*, *92*(2), 173.

Haak, K. V, Winawer, J., Harvey, B. M., Renken, R., Dumoulin, S. O., Wandell, B. A., & Cornelissen, F. W. (2013). Connective field modeling. *Neuroimage*, *66*, 376–384.

Hadamard, J. (1952). *Lectures on Cauchy's problem in partial differential equations*. Dover.

Hämäläinen, M., Hari, R., Ilmoniemi, R. J., Knuutila, J., & Lounasmaa, O. V. (1993). Magnetoencephalography—theory, instrumentation, and applications to noninvasive studies of the working human brain. *Reviews of Modern Physics*, *65*(2), 413.

Hansen, B. C., Essock, E. A., Zheng, Y., & DeFord, J. K. (2003). Perceptual anisotropies in visual processing and their relation to natural image statistics. *Network: Computation in Neural Systems*, *14*(3), 501–526.

Hartline, H. K. (1940). The receptive fields of optic nerve fibers. *American Journal of Physiology-Legacy Content*, *130*(4), 690–699.

Harvey, B. M., & Dumoulin, S. O. (2011). The relationship between cortical magnification factor and population receptive field size in human visual cortex: constancies in cortical architecture. *Journal of Neuroscience*, *31*(38), 13604–13612.

Harvey, B. M., & Dumoulin, S. O. (2016). Visual motion transforms visual space representations similarly throughout the human visual hierarchy. *Neuroimage*, *127*, 173–185.

Harvey, B. M., Klein, B. P., Petridou, N., & Dumoulin, S. O. (2013). Topographic representation of numerosity in the human parietal cortex. *Science*, *341*(6150), 1123–1126.

Harvey, B. M., Vansteensel, M. J., Ferrier, C. H., Petridou, N., Zuiderbaan, W., Aarnoutse, E. J., … Leijten, F. S. S. (2013). Frequency specific spatial interactions in human electrocorticography: V1 alpha oscillations reflect surround suppression. *Neuroimage*, *65*, 424–432.

Heeger, D. J., & Ress, D. (2002). What does fMRI tell us about neuronal activity? *Nature Reviews Neuroscience*, *3*(2), 142–151.

Hegdé, J., & Van Essen, D. C. (2000). Selectivity for complex shapes in primate visual area V2.

Journal of Neuroscience, *20*(5), RC61–RC61.

Hemsley, D. R. (2005). The schizophrenic experience: taken out of context? *Schizophrenia Bulletin*, *31*(1), 43–53.

Henriksson, L., Nurminen, L., Hyvärinen, A., & Vanni, S. (2008). Spatial frequency tuning in human retinotopic visual areas. *Journal of Vision*, *8*(10), 5.

Hermes, D., Petridou, N., Kay, K., & Winawer, J. (2019). An image-computable model for the stimulus selectivity of gamma oscillations. *BioRxiv*, 583567.

Hetherington, P. A., & Swindale, N. V. (1999). Receptive field and orientation scatter studied by tetrode recordings in cat area 17. *Visual Neuroscience*, *16*(4), 637–652.

Hicks, T. P., Lee, B. B., & Vidyasagar, T. R. (1983). The responses of cells in macaque lateral geniculate nucleus to sinusoidal gratings. *The Journal of Physiology*, *337*(1), 183–200.

Hoffmann, M. B., Kaule, F. R., Levin, N., Masuda, Y., Kumar, A., Gottlob, I., … Wolynski, B. (2012). Plasticity and stability of the visual system in human achiasma. *Neuron*, *75*(3), 393–401.

Holroyd, S., & Wooten, G. F. (2006). Preliminary FMRI evidence of visual system dysfunction in Parkinson's disease patients with visual hallucinations. *The Journal of Neuropsychiatry and Clinical Neurosciences*, *18*(3), 402–404.

Huang, M. X., Mosher, J. C., & Leahy, R. M. (1999). A sensor-weighted overlapping-sphere head model and exhaustive head model comparison for MEG. *Physics in Medicine & Biology*, *44*(2), 423.

Hubel, D. H., & Wiesel, T. N. (1961). Integrative action in the cat's lateral geniculate body. *The Journal of Physiology*, *155*(2), 385–398.

Hubel, D. H., & Wiesel, T. N. (1962). Receptive fields, binocular interaction and functional architecture in the cat's visual cortex. *The Journal of Physiology*, *160*(1), 106–154.

Hubel, D. H., & Wiesel, T. N. (1968). Receptive fields and functional architecture of monkey striate cortex. *The Journal of Physiology*, *195*(1), 215–243.

Hubel, D. H., & Wiesel, T. N. (1974). Uniformity of monkey striate cortex: a parallel relationship between field size, scatter, and magnification factor. *Journal of Comparative Neurology*, *158*(3), 295–305.

`

Hummer, A., Ritter, M., Tik, M., Ledolter, A. A., Woletz, M., Holder, G. E., … Windischberger, C. (2016). Eyetracker-based gaze correction for robust mapping of population receptive fields. *Neuroimage*, *142*, 211–224.

Hupé, J. M., James, A. C., Payne, B. R., Lomber, S. G., Girard, P., & Bullier, J. (1998). Cortical feedback improves discrimination between figure and background by V1, V2 and V3 neurons. *Nature*, *394*(6695), 784.

Ichida, J. M., Schwabe, L., Bressloff, P. C., & Angelucci, A. (2007). Response facilitation from the “suppressive” receptive field surround of macaque V1 neurons. *Journal of Neurophysiology*, *98*(4), 2168–2181.

Imamura, T., Ishii, K., Hirono, N., Hashimoto, M., Tanimukai, S., Kazuai, H., … Mori, E. (1999). Visual hallucinations and regional cerebral metabolism in dementia with Lewy bodies (DLB). *Neuroreport*, *10*(9), 1903–1907.

Ito, M., & Komatsu, H. (2004). Representation of angles embedded within contour stimuli in area V2 of macaque monkeys. *Journal of Neuroscience*, *24*(13), 3313–3324.

Jardri, R., & Deneve, S. (2013). Circular inferences in schizophrenia. *Brain*, *136*(11), 3227–3241.

Jardri, R., Thomas, P., Delmaire, C., Delion, P., & Pins, D. (2012). The neurodynamic organization of modality-dependent hallucinations. *Cerebral Cortex*, *23*(5), 1108–1117.

Jones, H. E., Wang, W., & Sillito, A. M. (2002). Spatial organization and magnitude of orientation contrast interactions in primate V1. *Journal of Neurophysiology*, *88*(5), 2796–2808.

Kapadia, M. K., Ito, M., Gilbert, C. D., & Westheimer, G. (1995). Improvement in visual sensitivity by changes in local context: parallel studies in human observers and in V1 of alert monkeys. *Neuron*, *15*(4), 843–856.

Kaplan, E., & Shapley, R. M. (1982). X and Y cells in the lateral geniculate nucleus of macaque monkeys. *The Journal of Physiology*, *330*(1), 125–143.

Kastner, S., De Weerd, P., Desimone, R., & Ungerleider, L. G. (1998). Mechanisms of directed attention in the human extrastriate cortex as revealed by functional MRI. *Science*, *282*(5386), 108–111.

`

Kastner, S., Nothdurft, H.-C., & Pigarev, I. N. (1999). Neuronal responses to orientation and motion contrast in cat striate cortex. *Visual Neuroscience*, *16*(3), 587–600.

Kay, K. N., Naselaris, T., Prenger, R. J., & Gallant, J. L. (2008). Identifying natural images from human brain activity. *Nature*, *452*(7185), 352.

Kay, K. N., Winawer, J., Mezer, A., & Wandell, B. A. (2013). Compressive spatial summation in human visual cortex. *Journal of Neurophysiology*, *110*(2), 481–494.

Kay, S. R., Fiszbein, A., & Opler, L. A. (1987). The positive and negative syndrome scale (PANSS) for schizophrenia. *Schizophrenia Bulletin*, *13*(2), 261–276.

Kayser, C., Körding, K. P., & König, P. (2004). Processing of complex stimuli and natural scenes in the visual cortex. *Current Opinion in Neurobiology*, *14*(4), 468–473.

Kayser, C., Salazar, R. F., & Konig, P. (2003). Responses to natural scenes in cat V1. *Journal of Neurophysiology*, *90*(3), 1910–1920.

Keane, B. P., Silverstein, S. M., Wang, Y., & Papathomas, T. V. (2013). Reduced depth inversion illusions in schizophrenia are state-specific and occur for multiple object types and viewing conditions. *Journal of Abnormal Psychology*, *122*(2), 506.

Kim, D., Wylie, G., Pasternak, R., Butler, P. D., & Javitt, D. C. (2006). Magnocellular contributions to impaired motion processing in schizophrenia. *Schizophrenia Research*, *82*(1), 1–8.

Klein, B. P., Harvey, B. M., & Dumoulin, S. O. (2014). Attraction of position preference by spatial attention throughout human visual cortex. *Neuron*, *84*(1), 227–237.

Knierim, J. J., & Van Essen, D. C. (1992). Neuronal responses to static texture patterns in area V1 of the alert macaque monkey. *Journal of Neurophysiology*, *67*(4), 961–980.

Koethe, D., Gerth, C. W., Neatby, M. A., Haensel, A., Thies, M., Schneider, U., … Leweke, F. M. (2006). Disturbances of visual information processing in early states of psychosis and experimental delta-9-tetrahydrocannabinol altered states of consciousness. *Schizophrenia Research*, *88*(1–3), 142–150.

Koethe, D., Kranaster, L., Hoyer, C., Gross, S., Neatby, M. A., Schultze-Lutter, F., … Leweke, F. M. (2009). Binocular depth inversion as a paradigm of reduced visual information processing in prodromal state, antipsychotic-naive and treated schizophrenia. *European*

`

Archives of Psychiatry and Clinical Neuroscience, *259*(4), 195.

Kovacs, I., & Julesz, B. (1993). A closed curve is much more than an incomplete one: Effect of closure in figure-ground segmentation. *Proceedings of the National Academy of Sciences*, *90*(16), 7495–7497.

Kuffler, S. W. (1953). Discharge patterns and functional organization of mammalian retina. *Journal of Neurophysiology*, *16*(1), 37–68.

Kulikowski, J. J., Marčelja, S., & Bishop, P. O. (1982). Theory of spatial position and spatial frequency relations in the receptive fields of simple cells in the visual cortex. *Biological Cybernetics*, *43*(3), 187–198.

Kupers, E. R., Wang, H. X., Amano, K., Kay, K. N., Heeger, D. J., & Winawer, J. (2018). A non-invasive, quantitative study of broadband spectral responses in human visual cortex. *PloS One*, *13*(3), e0193107.

Lamme, V. A. (1995). The neurophysiology of figure-ground segregation in primary visual cortex. *Journal of Neuroscience*, *15*(2), 1605–1615.

Lamme, V. A. F., Super, H., & Spekreijse, H. (1998). Feedforward, horizontal, and feedback processing in the visual cortex. *Current Opinion in Neurobiology*, *8*(4), 529–535.

Larsson, J., & Heeger, D. J. (2006). Two retinotopic visual areas in human lateral occipital cortex. *Journal of Neuroscience*, *26*(51), 13128–13142.

Lerma-Usabiaga, G., Benson, N., Winawer, J., & Wandell, B. A. (2020). A validation framework for neuroimaging software: the case of population receptive fields. *BioRxiv*, 2020.01.07.897991. https://doi.org/10.1101/2020.01.07.897991

Leuba, G., & Garey, L. J. (1989). Comparison of neuronal and glial numerical density in primary and secondary visual cortex of man. *Experimental Brain Research*, *77*(1), 31–38.

Levin, N., Dumoulin, S. O., Winawer, J., Dougherty, R. F., & Wandell, B. A. (2010). Cortical maps and white matter tracts following long period of visual deprivation and retinal image restoration. *Neuron*, *65*(1), 21–31.

Levitt, J. B., & Lund, J. S. (1997). Contrast dependence of contextual effects in primate visual cortex. *Nature*, *387*(6628), 73.

Levitt, J. B., & Lund, J. S. (2002). The spatial extent over which neurons in macaque striate

cortex pool visual signals. *Visual Neuroscience*, *19*(4), 439–452.

Li, C.-Y. (1996). Integration fields beyond the classical receptive field: organization and functional properties. *Physiology*, *11*(4), 181–186.

Li, W., Piëch, V., & Gilbert, C. D. (2006). Contour saliency in primary visual cortex. *Neuron*, *50*(6), 951–962.

Logothetis, N. K., & Wandell, B. A. (2004). Interpreting the BOLD signal. *Annu. Rev. Physiol.*, *66*, 735–769.

Lu, H. D., & Roe, A. W. (2007). Optical imaging of contrast response in macaque monkey V1 and V2. *Cerebral Cortex*, *17*(11), 2675–2695.

Maffei, L., & Fiorentini, A. (1973). The visual cortex as a spatial frequency analyser. *Vision Research*, *13*(7), 1255–1267.

Maffei, L., & Fiorentini, A. (1976). The unresponsive regions of visual cortical receptive fields. *Vision Research*, *16*(10), 1131-IN5.

Mante, V., Bonin, V., & Carandini, M. (2008). Functional mechanisms shaping lateral geniculate responses to artificial and natural stimuli. *Neuron*, *58*(4), 625–638.

Marques, J. P., Kober, T., Krueger, G., van der Zwaag, W., Van de Moortele, P.-F., & Gruetter, R. (2010). MP2RAGE, a self bias-field corrected sequence for improved segmentation and T1-mapping at high field. *Neuroimage*, *49*(2), 1271–1281.

Martin, D., Fowlkes, C., Tal, D., & Malik, J. (2001). *A database of human segmented natural images and its application to evaluating segmentation algorithms and measuring ecological statistics*. Iccv Vancouver:

Matsui, H., Udaka, F., Tamura, A., Oda, M., Kubori, T., Nishinaka, K., & Kameyama, M. (2006). Impaired visual acuity as a risk factor for visual hallucinations in Parkinson's disease. *Journal of Geriatric Psychiatry and Neurology*, *19*(1), 36–40.

Mattay, V. S., & Weinberger, D. R. (1999). Organization of the human motor system as studied by functional magnetic resonance imaging. *European Journal of Radiology*, *30*(2), 105–114.

Mazer, J. A., & Gallant, J. L. (2000). Object recognition: seeing us seeing shapes. *Current Biology*, *10*(18), R668–R670.

`

McIlwain, J. T. (1964). Receptive fields of optic tract axons and lateral geniculate cells: peripheral extent and barbiturate sensitivity. *Journal of Neurophysiology*, *27*(6), 1154–1173.

McKay, C. M., Headlam, D. M., & Copolov, D. L. (2000). Central auditory processing in patients with auditory hallucinations. *American Journal of Psychiatry*, *157*(5), 759–766.

Mechler, F., Victor, J. D., Purpura, K. P., & Shapley, R. (1998). Robust temporal coding of contrast by V1 neurons for transient but not for steady-state stimuli. *Journal of Neuroscience*, *18*(16), 6583–6598.

Montijn, J. S., Klink, P. C., & Van Wezel, R. J. A. (2012). Divisive normalization and neuronal oscillations in a single hierarchical framework of selective visual attention. *Frontiers in Neural Circuits*, *6*, 22.

Moradi, F., Liu, L. C., Cheng, K., Waggoner, R. A., Tanaka, K., & Ioannides, A. A. (2003). Consistent and precise localization of brain activity in human primary visual cortex by MEG and fMRI. *Neuroimage*, *18*(3), 595–609.

Mueser, K. T., Bellack, A. S., & Brady, E. U. (1990). Hallucinations in schizophrenia. *Acta Psychiatrica Scandinavica*, *82*(1), 26–29.

Murray, S. O., & Wojciulik, E. (2004). Attention increases neural selectivity in the human lateral occipital complex. *Nature Neuroscience*, *7*(1), 70.

Nasiotis, K., Clavagnier, S., Baillet, S., & Pack, C. C. (2017). High-resolution retinotopic maps estimated with magnetoencephalography. *Neuroimage*, *145*, 107–117.

Newsome, W. T., Maunsell, J. H. R., & van Essen, D. C. (1986). Ventral posterior visual area of the macaque: visual topography and areal boundaries. *Journal of Comparative Neurology*, *252*(2), 139–153.

Norton, D., Ongur, D., Stromeyer III, C., & Chen, Y. (2008). Altered ‘three-flash’illusion in response to two light pulses in schizophrenia. *Schizophrenia Research*, *103*(1–3), 275–282.

Nuechterlein, K. H., Barch, D. M., Gold, J. M., Goldberg, T. E., Green, M. F., & Heaton, R. K. (2004). Identification of separable cognitive factors in schizophrenia. *Schizophrenia Research*, *72*(1), 29–39.

`

O'Connor, D. H., Fukui, M. M., Pinsk, M. A., & Kastner, S. (2002). Attention modulates responses in the human lateral geniculate nucleus. *Nature Neuroscience*, *5*(11), 1203.

O'Craven, K. M., Downing, P. E., & Kanwisher, N. (1999). fMRI evidence for objects as the units of attentional selection. *Nature*, *401*(6753), 584.

O'Donnell, P. (2011). Adolescent onset of cortical disinhibition in schizophrenia: insights from animal models. *Schizophrenia Bulletin*, *37*(3), 484–492.

Olman, C. A., Ugurbil, K., Schrater, P., & Kersten, D. (2004). BOLD fMRI and psychophysical measurements of contrast response to broadband images. *Vision Research*, *44*(7), 669–683.

Oostenveld, R., Fries, P., Maris, E., & Schoffelen, J.-M. (2011). FieldTrip: open source software for advanced analysis of MEG, EEG, and invasive electrophysiological data. *Computational Intelligence and Neuroscience*, *2011*, 1.

Pasupathy, A., & Connor, C. E. (1999). Responses to contour features in macaque area V4. *Journal of Neurophysiology*, *82*(5), 2490–2502.

Pelli, D. G. (1997). The VideoToolbox software for visual psychophysics: Transforming numbers into movies. *Spatial Vision*, *10*, 437–442.

Phillipson, O. T., & Harris, J. P. (1985). Perceptual changes in schizophrenia: a questionnaire survey. *Psychological Medicine*, *15*(4), 859–866.

Poghosyan, V., & Ioannides, A. A. (2007). Precise mapping of early visual responses in space and time. *Neuroimage*, *35*(2), 759–770.

Posner, M. I., & Gilbert, C. D. (1999). Attention and primary visual cortex. *Proceedings of the National Academy of Sciences*, *96*(6), 2585–2587.

Postmes, L., Sno, H. N., Goedhart, S., Van Der Stel, J., Heering, H. D., & De Haan, L. (2014). Schizophrenia as a self-disorder due to perceptual incoherence. *Schizophrenia Research*, *152*(1), 41–50.

Ringach, D. L., Hawken, M. J., & Shapley, R. (2002). Receptive field structure of neurons in monkey primary visual cortex revealed by stimulation with natural image sequences. *Journal of Vision*, *2*(1), 2.

Robol, V., Tibber, M. S., Anderson, E. J., Bobin, T., Carlin, P., Shergill, S. S., & Dakin, S. C.

`

(2013). Reduced crowding and poor contour detection in schizophrenia are consistent with weak surround inhibition. *PloS One*, *8*(4), e60951.

Rockel, A. J., Hiorns, R. W., & Powell, T. P. (1980). The basic uniformity in structure of the neocortex. *Brain: A Journal of Neurology*, *103*(2), 221–244.

Rosa, M. G. P., Sousa, A. P. B., & Gattass, R. (1988). Representation of the visual field in the second visual area in the Cebus monkey. *Journal of Comparative Neurology*, *275*(3), 326–345.

Saenz, M., & Langers, D. R. M. (2014). Tonotopic mapping of human auditory cortex. *Hearing Research*, *307*, 42–52.

Sasaki, Y., Hadjikhani, N., Fischl, B., Liu, A. K., Marret, S., Dale, A. M., & Tootell, R. B. H. (2001). Local and global attention are mapped retinotopically in human occipital cortex. *Proceedings of the National Academy of Sciences*, *98*(4), 2077–2082.

Sceniak, M. P., Hawken, M. J., & Shapley, R. (2001). Visual spatial characterization of macaque V1 neurons. *Journal of Neurophysiology*, *85*(5), 1873–1887.

Sceniak, M. P., Hawken, M. J., & Shapley, R. (2002). Contrast-dependent changes in spatial frequency tuning of macaque V1 neurons: effects of a changing receptive field size. *Journal of Neurophysiology*, *88*(3), 1363–1373.

Schiller, P. H., Finlay, B. L., & Volman, S. F. (1976). Quantitative studies of single-cell properties in monkey striate cortex. III. Spatial frequency. *Journal of Neurophysiology*, *39*(6), 1334–1351.

Schmeider, U., Leweke, F. M., Sternemann, U., Emrich, H. M., & Weber, M. M. (1996). Visual 3D illusion: a systems-theoretical approach to psychosis. *European Archives of Psychiatry and Clinical Neuroscience*, *246*(5), 256–260.

Schwarzkopf, D. S., Anderson, E. J., de Haas, B., White, S. J., & Rees, G. (2014). Larger extrastriate population receptive fields in autism spectrum disorders. *Journal of Neuroscience*, *34*(7), 2713–2724.

Sengpiel, F., Sen, A., & Blakemore, C. (1997). Characteristics of surround inhibition in cat area 17. *Experimental Brain Research*, *116*(2), 216–228.

Sharon, D., Hämäläinen, M. S., Tootell, R. B. H., Halgren, E., & Belliveau, J. W. (2007). The

advantage of combining MEG and EEG: comparison to fMRI in focally stimulated visual cortex. *Neuroimage*, *36*(4), 1225–1235.

Sherrington, C. S. (1906). Observations on the scratch-reflex in the spinal dog. *The Journal of Physiology*, *34*(1–2), 1–50.

Sillito, A. M. (1995). Grieve KL, Jones HE, Cudeiro J, and Davis J. *Visual Cortical Mechanisms Detecting Focal Orientation Discontinuities. Nature*, *378*, 492–496.

Silverstein, S. M. (2016). Visual perception disturbances in schizophrenia: a unified model. In *The neuropsychopathology of schizophrenia* (pp. 77–132). Springer.

Silverstein, S. M., & Keane, B. P. (2011). Perceptual organization impairment in schizophrenia and associated brain mechanisms: review of research from 2005 to 2010. *Schizophrenia Bulletin*, *37*(4), 690–699.

Silverstein, S. M., Keane, B. P., Wang, Y., Mikkilineni, D., Paterno, D., Papathomas, T. V, & Feigenson, K. (2013). Effects of short-term inpatient treatment on sensitivity to a size contrast illusion in first-episode psychosis and multiple-episode schizophrenia. *Frontiers in Psychology*, *4*, 466.

Silverstein, S. M., & Schenkel, L. S. (1997). Schizophrenia as a model of context-deficient cortical computation. *Behavioral and Brain Sciences*, *20*(4), 696–697.

Simoncelli, E. P. (2003). Vision and the statistics of the visual environment. *Current Opinion in Neurobiology*, *13*(2), 144–149.

Slaghuis, W. A. (1998). Contrast sensitivity for stationary and drifting spatial frequency gratings in positive-and negative-symptom schizophrenia. *Journal of Abnormal Psychology*, *107*(1), 49.

Small, I. F., Small, J. G., & Andersen, J. M. (1966). Clinical characteristics of hallucinations of schizophrenia. *Diseases of the Nervous System*, *27*(5), 349.

Smith, A. T., Singh, K. D., Williams, A. L., & Greenlee, M. W. (2001). Estimating receptive field size from fMRI data in human striate and extrastriate visual cortex. *Cerebral Cortex*, *11*(12), 1182–1190.

Smith, S. M., Jenkinson, M., Woolrich, M. W., Beckmann, C. F., Behrens, T. E. J., Johansen-Berg, H., … Flitney, D. E. (2004). Advances in functional and structural MR image analysis

and implementation as FSL. *Neuroimage*, *23*, S208–S219.

Smyth, D., Willmore, B., Baker, G. E., Thompson, I. D., & Tolhurst, D. J. (2003). The receptive-field organization of simple cells in primary visual cortex of ferrets under natural scene stimulation. *Journal of Neuroscience*, *23*(11), 4746–4759.

Spillmann, L. (2014). Receptive fields of visual neurons: the early years. *Perception*, *43*(11), 1145–1176.

Spillmann, L., & Werner, J. S. (1996). Long-range interactions in visual perception. *Trends in Neurosciences*, *19*(10), 428–434.

Stigliani, A., Jeska, B., & Grill-Spector, K. (2017). Encoding model of temporal processing in human visual cortex. *Proceedings of the National Academy of Sciences*, *114*(51), E11047–E11056.

Tadel, F., Baillet, S., Mosher, J. C., Pantazis, D., & Leahy, R. M. (2011). Brainstorm: a user-friendly application for MEG/EEG analysis. *Computational Intelligence and Neuroscience*, *2011*, 8.

Tadin, D., Kim, J., Doop, M. L., Gibson, C., Lappin, J. S., Blake, R., & Park, S. (2006). Weakened center-surround interactions in visual motion processing in schizophrenia. *Journal of Neuroscience*, *26*(44), 11403–11412.

Tibber, M. S., Anderson, E. J., Bobin, T., Carlin, P., Shergill, S. S., & Dakin, S. C. (2015). Local and global limits on visual processing in schizophrenia. *PLoS One*, *10*(2), e0117951.

Tootell, R. B., Silverman, M. S., Hamilton, S. L., Switkes, E., & De Valois, R. L. (1988). Functional anatomy of macaque striate cortex. V. Spatial frequency. *Journal of Neuroscience*, *8*(5), 1610–1624.

Touryan, J., Felsen, G., & Dan, Y. (2005). Spatial structure of complex cell receptive fields measured with natural images. *Neuron*, *45*(5), 781–791.

van Dijk, J. A., de Haas, B., Moutsiana, C., & Schwarzkopf, D. S. (2016). Intersession reliability of population receptive field estimates. *NeuroImage*, *143*, 293–303.

van Es, D. M., Theeuwes, J., & Knapen, T. (2018). Spatial sampling in human visual cortex is modulated by both spatial and feature-based attention. *ELife*, *7*, e36928.

Van Essen, D. C. (2003). Organization of visual areas in macaque and human cerebral cortex.

`

The Visual Neurosciences, *1*, 507–521.

Van Essen, D. C., & DeYoe, E. A. (1995). Concurrent processing in the primate visual cortex. *The Cognitive Neurosciences*, 383–400.

Van Ommen, M. M., Van Beilen, M., Cornelissen, F. W., Smid, H., Knegtering, H., Aleman, A., … Investigators, G. (2016). The prevalence of visual hallucinations in non-affective psychosis, and the role of perception and attention. *Psychological Medicine*, *46*(8), 1735–1747.

van Ommen, M. M., van Laar, T., Cornelissen, F. W., & Bruggeman, R. (2019). Visual hallucinations in psychosis. *Psychiatry Research*, *280*, 112517.

Vinje, W. E., & Gallant, J. L. (2000). Sparse coding and decorrelation in primary visual cortex during natural vision. *Science*, *287*(5456), 1273–1276.

Von Baumgarten, R., & Jung, R. (1952). Microelectrode studies on the visual cortex. *Revue Neurologique*, *87*(2), 151.

Vorwerk, J., Cho, J.-H., Rampp, S., Hamer, H., Knösche, T. R., & Wolters, C. H. (2014). A guideline for head volume conductor modeling in EEG and MEG. *NeuroImage*, *100*, 590–607.

Walker, G. A., Ohzawa, I., & Freeman, R. D. (1999). Asymmetric suppression outside the classical receptive field of the visual cortex. *Journal of Neuroscience*, *19*(23), 10536–10553.

Wandell, B. A. (1999). Computational neuroimaging of human visual cortex. *Annual Review of Neuroscience*, *22*(1), 145–173.

Wandell, B. A., Dumoulin, S. O., & Brewer, A. A. (2007). Visual field maps in human cortex. *Neuron*, *56*(2), 366–383.

Wandell, B. A., & Winawer, J. (2015). Computational neuroimaging and population receptive fields. *Trends in Cognitive Sciences*, *19*(6), 349–357.

Wandell, B. A., Winawer, J., & Kay, K. N. (2015). Computational modeling of responses in human visual cortex. *Brain Mapping: An Encyclopedic Reference*, *1*, 651–659.

Wang, L., Mruczek, R. E. B., Arcaro, M. J., & Kastner, S. (2014). Probabilistic maps of visual topography in human cortex. *Cerebral Cortex*, *25*(10), 3911–3931.

`

Waters, F., Collerton, D., Ffytche, D. H., Jardri, R., Pins, D., Dudley, R., … Ford, S. (2014). Visual hallucinations in the psychosis spectrum and comparative information from neurodegenerative disorders and eye disease. *Schizophrenia Bulletin*, *40*(Suppl_4), S233–S245.

Weliky, M., Fiser, J., Hunt, R. H., & Wagner, D. N. (2003). Coding of natural scenes in primary visual cortex. *Neuron*, *37*(4), 703–718.

Winawer, J., Horiguchi, H., Sayres, R. A., Amano, K., & Wandell, B. A. (2010). Mapping hV4 and ventral occipital cortex: the venous eclipse. *Journal of Vision*, *10*(5), 1.

Winawer, J., Kay, K. N., Foster, B. L., Rauschecker, A. M., Parvizi, J., & Wandell, B. A. (2013). Asynchronous broadband signals are the principal source of the BOLD response in human visual cortex. *Current Biology*, *23*(13), 1145–1153.

Wipf, D., & Nagarajan, S. (2009). A unified Bayesian framework for MEG/EEG source imaging. *NeuroImage*, *44*(3), 947–966.

Wojciulik, E., Kanwisher, N., & Driver, J. (1998). Covert visual attention modulates face-specific activity in the human fusiform gyrus: fMRI study. *Journal of Neurophysiology*, *79*(3), 1574–1578.

Xu, X., Anderson, T. J., & Casagrande, V. A. (2007). How do functional maps in primary visual cortex vary with eccentricity? *Journal of Comparative Neurology*, *501*(5), 741–755.

Yang, E., Tadin, D., Glasser, D., Hong, S. W., Blake, R., & Park, S. (2013). Visual context processing in bipolar disorder: a comparison with schizophrenia. *Frontiers in Psychology*, *4*, 569.

Yildirim, F., Carvalho, J., & Cornelissen, F. W. (2018). A second-order orientation-contrast stimulus for population-receptive-field-based retinotopic mapping. *NeuroImage*, *164*, 183–193.

Yoon, J. H., Maddock, R. J., Rokem, A., Silver, M. A., Minzenberg, M. J., Ragland, J. D., & Carter, C. S. (2010). GABA concentration is reduced in visual cortex in schizophrenia and correlates with orientation-specific surround suppression. *Journal of Neuroscience*, *30*(10), 3777–3781.

Zeidman, P., Silson, E. H., Schwarzkopf, D. S., Baker, C. I., & Penny, W. (2018). Bayesian population receptive field modelling. *NeuroImage*, *180*, 173–187.

`

Zhou, J., Benson, N. C., Kay, K. N., & Winawer, J. (2018). Compressive temporal summation in human visual cortex. *Journal of Neuroscience*, *38*(3), 691–709.

Zuiderbaan, W., Harvey, B. M., & Dumoulin, S. O. (2012). Modeling center–surround configurations in population receptive fields using fMRI. *Journal of Vision*, *12*(3), 10.

`

Appendix

Nederlandse samenvatting

`

Mensen zijn visueel ingesteld**.** Het gezichtsvermogen is een belangrijk zintuig en essentieel om te communiceren en te navigeren in de wereld om ons heen**.** Kennis over de werking van het visuele systeem is daarom van fundamenteel belang. Visuele waarneming omvat verschillende biologische systemen, van de ogen tot aan de neuronen in het brein. In dit proefschrift onderzoeken we de verwerking van visuele informatie door populaties van miljoenen neuronen.

Visuele informatie wordt verwerkt door neuronen in de visuele cortex van ons brein, waarbij elk individuele neuron reageert op een specifiek gebied in het gezichtsveld; *het receptieve veld* (RV) van het neuron. Het RV is ook selectief voor verschillende kenmerken van de visuele informatie, zoals de vorm, oriëntatie, positie en spatiale frequentie van hetgeen waarnaar gekeken wordt. Neuronen waarvan de RVs dicht bij elkaar liggen, bevinden zich ook dicht bij elkaar in de visuele cortex en vormen hier zogenaamde visuele gebieden in het brein.

Het *klassieke RV* van een neuron is het deel van het visuele veld waarbinnen aanwezigheid van een stimulus een response van het neuron opwekt. Soms kunnen stimuli die buiten het klassieke RV van een neuron vallen de respons van een neuron toch beïnvloeden via intercellulaire verbindingen. Visuele neuronen kunnen namelijk met elkaar communiceren via deze intercellulaire verbindingen. Men spreekt dan van een *extra-klassiek RV*. Een stimulus buiten het klassieke RV van een neuron kan op zichzelf geen respons van het neuron opwekken, maar als deze stimulus wel binnen het extra-klassieke RV van het neuron valt kan de aanwezigheid van deze stimulus de respons van het neuron op stimuli binnen het klassieke RV wijzigen. In Figuur 1 worden verschillende vormen van extra-klassieke RVs weergegeven. Interacties tussen klassieke en extra-klassieke RVs, kortweg extra-klassieke interacties, spelen een cruciale rol bij de overgang van lokale naar globale verwerking van visuele informatie. Ze spelen een belangrijke rol bij bijvoorbeeld de herkenning van objecten en het opdelen van een complexe afbeelding in verschillende onderdelen (*scene segmentation).* Vergeleken met afbeeldingen van simpele vormen, zoals strepen of cirkels, vinden er daarom veel extra-klassieke interacties plaats als we kijken naar afbeeldingen van een natuurlijke omgeving.

RV eigenschappen van individuele neuronen bij mensen kunnen over het algemeen niet worden onderzocht, omdat het gebruik van invasieve elektrofysiologie voor niet-klinische doeleinden

`

niet toegestaan is . Om RV-eigenschappen toch bij mensen te onderzoeken, kan beeldvorming middels non-invasieve functionele magnetische resonantie (fMRI) worden gebruikt. Echter, de spatiële resolutie van fMRI is beperkt tot ongeveer 1 mm. Op deze schaal geven de metingen de activiteit van miljoenen neuronen weer. RVs onderzocht met fMRI worden om deze reden aangeduid als populatie RVs (pRV). Bovendien meet fMRI een indirecte maat van neurale activiteit, namelijk bloedoxygenatie. Deze metingen worden daarom bloedoxygenatieniveau afhankelijke signalen genoemd (blood oxygenation level dependent, afgekort als BOLD).

Naast fMRI zijner ook andere methoden om hersenactiviteit te meten, zoals magneto-encefalografie (MEG), elektro-encefalografie (EEG) en elektrocorticografie (ECoG). Deze meten echter eveneens indirecte gevolgen van de activiteit van populaties neuronen. Daarom is de precisie waarmee deze metingen de onderliggende neurale activiteit representeren enigszins onzeker. Wanneer modellen gebaseerd op een specifieke techniek metingen met een andere techniek kunnen verklaren kan een directe relatie tussen neurale activiteit en de verschillende meetmethoden kan aannemelijk worden gemaakt. Om dit te bereiken, hebben we in hoofdstuk 2 van dit proefschrift een nieuw model geïntroduceerd. Dit model kan MEG metingen tijdens visuele stimulatie voorspellen op basis van een pRV analyse van fMRI metingen tijdens visuele stimulatie.

pRV eigenschappen worden berekend door met behulp van fMRI metingen de reactie van populaties neuronen op visuele stimuli te modelleren. Deze modellen worden pRV modellen genoemd. PRV modellen vormen een fundament in de visuele neurowetenschappen voor het bestuderen van spatiële eigenschappen van het visuele systeem**.** PRV modellen geven gedetailleerde informatie over pRV eigenschappen, zoals de positie en de grootte van het RV, waaronder de grootte van het excitatoire centrum van het RV (*excitatory center*) en de grootte van de daaromheen liggende suppressieve schil (*suppressive surround*). Ook andere complexe eigenschappen, zoals spatiële summatie en connectiviteit tussen neuronen, kunnen worden onderzocht**.** Met behulp van zorgvuldig ontworpen experimentele stimuli en taken kunnen we pRV modellen gebruiken om verschillende eigenschappen van het visuele systeem te onderzoeken bij zowel gezonde proefpersonen als mensen met een klinische aandoening.

`

In hoofdstuk 3 van dit proefschrift hebben we onderzocht in hoeverre pRV eigenschappen de eigenschappen van RVs van individuele neuronen weergeven. Hiervoor hebben we visuele stimuli gebruikt met verschillende spatiële frequenties, om zo subpopulaties neuronen te stimuleren die verschillen in hun gevoeligheid voor spatiële frequenties. In hoofdstuk 4 hebben we het effect van de extra-klassieke interacties op de pRV eigenschappen onderzocht. Ten slotte hebben we in hoofdstuk 5 pRV modellen gebruikt om afwijkingen in he visuele systeem die leiden tot visuele hallucinaties bij patiënten met schizofrenie te onderzoeken.

Het huidige proefschrift heeft de kennis van het menselijke visuele systeem in zowel gezonde proefpersonen als mensen met schizofrenie uitgebreid met behulp van pRV modellen. We ontdekten dat pRV modellen, gebouwd om fMRI metingen te voorspellen, ook MEG metingen kunnen voorspellen. Dit geeft vertrouwen in een gemeenschappelijke onderliggende maat van neurale activiteit in beide metingen en maakt aannemelijk dat pRV modellen die in fMRI onderzoek worden gebruikt inderdaad onderliggende neurale activiteit representeren. Bovendien biedt ons nieuwe model mogelijkheden om het visuele systeem met zowel een hoge spatiële als een hoge temporele resolutie te onderzoeken. De bevindingen in dit proefschrift tonen tevens aan dat eigenschappen van individuele neuronen verdwijnen op populatieniveau, waarschijnlijk als gevolg van intercellulaire interacties. Het gebruik van afbeeldingen van een natuurlijke omgeving stelde ons in staat om deze extra-klassieke interacties op populatieniveau in beeld te brengen. Daarnaast hebben we onze kennis van het visuele systeem en pRV eigenschappen uitgebreid naar een klinische populatie door visuele hallucinaties te bestuderen bij patiënten met schizofrenie. Er was een afname te zien in de grootte van de suppressieve schil van het RV bij patiënten met visuele hallucinaties in vergelijking met patiënten zonder visuele hallucinaties. Wij vermoeden dat deze afname in grootte komt door een onbalans in inhibitoire interacties tussen neuronen.

Het voornaamste doel van dit proefschrift was het bestuderen van de invloed van intercellulaire en extra-klassieke interacties op pRV eigenschappen, zodat we meer te weten komen over de eigenschappen van ons visuele systeem op het niveau van grote populaties neuronen. Wij hebben dit voornamelijk onderzocht wat betreft spatiële modulaties van pRVs en ontdekt dat pRV eigenschappen kunnen afwijken van de eigenschappen van RVs van individuele neuronen. Daarnaast hebben we deze methode toegepast op een klinische populatie en nieuwe

`

mogelijkheden ontdekt om onderzoek te doen naar temporele modulaties in pRV eigenschappen.

`

`

Appendix

Curriculum Vitae

`

Akhil Edadan was born on 29th of March, 1993 in Payyanur, India. In 2010, he completed his secondary education at Kendriya Vidyalaya in Payyanur, India. After this, he received his B. Tech degree in Biomedical engineering from VIT University, Vellore, India in 2014. He then graduated from University college Dublin, Ireland with a master's degree in Bioengineering. In 2016, he started as a PhD student at the department of experimental psychology of Utrecht University, under the supervision of Prof. dr. S.O. Dumoulin. He is now working as risk model engineer at Rabobank in Utrecht.